DISSERTATION

ROTATIONAL MOTION AND ORGANIZATION STUDIES OF CELL MEMBRANE PROTEINS

Submitted by

Dongmei Zhang

Department of Chemistry

In partial fulfillment of the requirements

For the Degree of Doctor of Philosophy

Colorado State University

Fort Collins, Colorado

Spring 2016

Doctoral Committee:

Advisor: B. George Barisas

Alan Van Orden
Chuck Henry
Deborah A. Roess
Debbie Crans

ABSTRACT

ROTATIONAL MOTION AND ORGANIZATION STUDIES OF CELL MEMBRANE PROTEINS

Cell membranes are dynamic structures with complex organization. The complexity of the cell membrane arises from intrinsic membrane structure, membrane microdomains within the plasma membrane and the membrane cytoskeleton. Plasma membrane receptors are integral membrane proteins with diverse structures and functions which bind specific ligands to trigger cellular responses. Due to compartmentalization of the plasma membrane and the formation of membrane microdomains, receptors are distributed non-homogeneously in the cell membrane bilayer. Both lateral and rotational diffusion of membrane receptors reflects different kinds of intermolecular interactions within the plasma membrane environment. Understanding protein diffusion within the membrane is very important to further understanding biomolecular interactions in vivo during complex biological processes including receptor-mediated signaling.

Rotational diffusion depends linearly on the in-membrane volume of the rotating proteins. Relative to lateral diffusion, rotational diffusion is a more sensitive probe of an individual molecule's size and local environment. We have used asymmetric quantum dots (QD) to conduct imaging measurements of individual 2H3 cell Type I Fcε receptor rotation on timescales down to 10 msec per frame. We have also used time-tagged single photon counting measurements of individual QD to examine μsec timescales, although rapid timescales are limited by QD emission rates. In both approaches, decays of time-autocorrelation functions (TACF) for fluorescence polarization fluctuations extend into the millisecond timescale, as

implied by time-resolved phosphorescence anisotropy results. Depending on instrumental parameters used in data analysis, polarization fluctuation TACFs can contain a contribution from the intensity fluctuation TACF arising from QD blinking. Such QD blinking feed-through is extremely sensitive to these analysis parameters which effectively change slightly from one measurement to another. We discuss approaches based on the necessary statistical independence of polarization and intensity fluctuations to guarantee removal of a blinking-based component from rotation measurements. Imaging results demonstrate a range of rotational behavior among individual molecules. Such slow motions, not observable previously, may occur with large signaling complexes, which are important targets of study in cell biology. These slow motions appear to be a property of the membrane itself, not of the receptor state. Our results may indicate that individual mesoscale membrane regions rotate or librate with respect to the overall cell surface.

The luteinizing hormone receptor (LHR) is a seven transmembrane domain receptor and a member of the GPCR family. It is located on luteal cells, granulosa and theca cells in females. Understanding how these protein receptors function on the plasma membrane will lead to better understanding of mammalian reproduction. LHR becomes aggregated upon binding hCG when receptors are expressed at physiological numbers. Binding of hormone to LHR leads to activation of adenylate cyclase (AC) and an increase in intracellular cyclic AMP (cAMP). ICUE3 is an Epac-based cAMP sensor with two fluorophores, cyan fluorescent protein (CFP) and the YFP variant, cpVenus, and a membrane-targeting motif which can be palmitoylated. Upon binding cAMP, ICUE3 undergoes a conformational change that separates CFP and YFP, significantly reducing FRET and thus increasing the ratio of CFP to YFP fluorescence upon excitation with an arc lamp or 405nm laser source. Hence we have investigated hLHR signal

transduction using the cyclic AMP reporter probe, ICUE3. A dual wavelength emission ratio (CFP/YFP) imaging method was used to detect a conformational change in ICUE3 upon binding cAMP. This technique is useful in understanding the sequence of intercellular events following hormone binding to receptor and in particular, the time course involved in signal transduction in a single cell. Our data suggested that CHO cells expressing ICUE3 and directly treated with different concentrations of cAMP with saponin can provide a dose-dependent relationship for changes in intracellular cAMP levels. Forskolin (50μM) causes maximal activation of the intracellular cAMP and an increase in the CFP/YFP emission ratio. In CHO cells expressing both ICUE3 and hLHR-mCherry, the CFP/YFP ratio increased in cells treated with forskolin and in hCG- treated cells. In flow cytometry studies, similar results were obtained when CHO cells expressed < 60k LHR-mCherry per cell. Our results indicate that ICUE3 can provide real time information on intracellular cAMP levels, and the ICUE3 is a reliable cAMP reporter can be used to examine various aspects of LH receptor-mediated signaling.

ACKNOWLEDGEMENTS

I would first like to extend my sincere thanks to my advisor Dr. B. George Barisas for guiding my research and scientific development at Colorado State University. I sincerely appreciate his contributions of time and ideas to my projects and his willingness and patience with me in all aspects of my research. I also would like to acknowledge Dr. Deborah A. Roess' invaluable help throughout my Ph.D. studies. The research in this dissertation would have not been successful without their help. I realize how fortunate I have been a student in their lab.

I would like to thank my present and former committee members for their efforts and contribution to this dissertation: Dr. Alan Van Orden, Dr. Chuck Henry, Dr. Debbie Crans and Dr. Dawn Rickey. Their advice, time and continued support made this work possible.

I would like to thank my present and former laboratory members for their advice, support and friendship. Special thanks to Dr. Shaorui Xu and Dr. Peter W. Winter for their help in microscopy techniques and suggestions for experimental methods.

In addition, I would like to thank my friends at CSU for their kind help over the past years. Dr. Yupaporn Sameenoi and Dr. Brendan Tompkins have supported me throughout my time in graduate school. Dr. Rajesh Kumar Nayakand, Dr. Kevin Whitcomb and Dr. Claire Filloux have given me friendship and support. Each of you made a significant impact on my life and I will always value the friendships that we have formed.

Finally, I would like to give my special thanks to my husband, Haitao Yu, who has encouraged and supported my study and research, and my two lovely kids, Andy Yu and Sara Yu.

I could not have reached my career goals without their support. I would also like to thank all of my family, relatives and friends who never wavered in their belief in me throughout this journey.

DEDICATION

This dissertation is dedicated to my grandma, my parents and parents-in law for their guidance and support. I will remember the kindness and love of my grandma, my father and my father-in-law forever.

TABLE OF CONTENTS

CHAPTER II: Use of The ICUE3 cAMP Reporter to Evaluate Luteinizing Hormone (LH) Receptor Function

LIST OF TABLES

LIST OF FIGURES

CHAPTER I

ROTATION OF SINGLE CELL SURFACE I RECEPTORS EXAMINED BY QUANTUM DOT PROBES

I. BACKGROUND

I.A. Structure of the cell membrane

Cell membranes are dynamic structures with complex organization [1]. In 1925, the presence of a lipid bilayer in cell membranes was proposed by Gorter and Grendel [2]. Based on the lipid bilayer model of Gorter and Grendel, Davidson and Danielli proposed a tri-layer, protein–lipid–protein model of membrane structure in which proteins were coated on either side of the lipid bilayer [3]. Roberson proposed the unit membrane model in 1959 which refined the Davidson–Danielli tri-layer model. In 1972, Singer and Nicolson proposed the "Fluid Mosaic Model" for membranes. Their model membrane consisted of integral and peripheral membrane proteins embedded in a fluid phospholipid bilayer [4] (Figure 1.1).

In the Fluid Mosaic Model, the membrane is made up of three components: lipids, proteins and oligosaccharides. Membrane lipids are represented by phospholipids, glycolipids, and cholesterol. The organization of the lipid bilayer is based on the combined effects of hydrophobic and hydrophilic interactions. Electrostatic interactions and hydrogen bonding play secondary role in the phospholipid bilayer organization. The ionic and polar head groups of the phospholipids are in contact with the aqueous extracellular region. The nonpolar fatty acid chains of the phospholipids stay together and resist contact with the aqueous environment. The amphipathic properties of lipids can lead to segregation of internal constituents from the external environment. Integral proteins are bound to membranes by mainly hydrophobic forces and peripheral proteins are bound to membranes by electrostatic or other non-hydrophobic

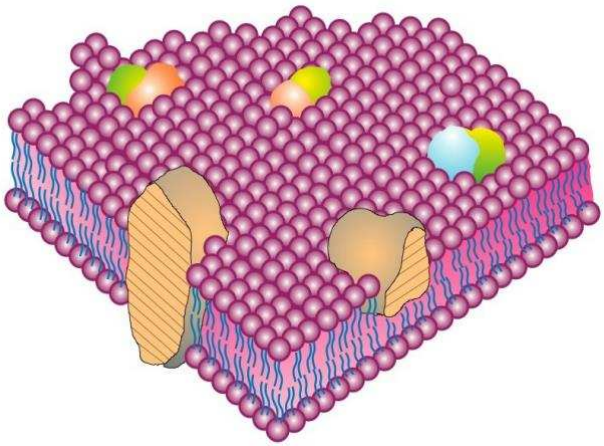

Figure 1.1: Fluid-mosaic membrane model of cell membrane structure proposed by Singer and Nicolson in 1972. The plasma membrane is a two-dimensional phospholipid bilayer with integral and peripheral proteins. The integral proteins are randomly distributed in the plane of the cell membrane, and the peripheral membrane proteins are temporarily attached either to the lipid bilayer or to integral proteins. From Singer and Nicolson, 1972 [4].

interactions [4]. An important property of the fluid mosaic model is the predicted ability of membrane components to move within the cell membrane via simple Brownian motion. Generally the two main modes of motion for both lipids and proteins are lateral diffusion and rotational diffusion (Figure 1.2). Flip-flop diffusion of lipids between leaflets of the bilayer does not occur frequently because of the energy barrier presented by the hydrophobic effect of the polar groups of lipids and proteins in cell membrane bilayer [5].

Data published since 1972 indicates that the plasma membrane is more complex than suggested by Singer's Fluid Mosaic Model. Lipids and proteins have more constrained diffusion than predicted by Singer and Nicolson because of protein-protein, protein-lipid, cytoskeletal interactions, *etc.* [6]. In 2003, Kusumi and co-workers included the cytoskeleton meshwork formed by actin and actin-binding proteins to the Fluid Mosaic Model [7] (Figure 1.3). The cytoskeleton provides mechanical stability to the plasma membrane and also can modulate the diffusion of plasma membrane proteins via interactions with membrane compartments. Protein lateral diffusion within a compartment is much faster than diffusion over longer distances. Although proteins tend to remain within compartments, hop diffusion occurs when proteins or lipids jump from between two compartments. Figure 1.4 shows a fluid-mosaic cell membrane model with contemporary information on the membrane skeleton, extracellular and membrane domain.

An additional level of membrane complexity arises from the formation of specialized microdomains within the plasma membrane [7]. Kusumi and his coworkers proposed three types of mesoscale (2–300 nm) domains to help understand the architecture and working mechanisms of the plasma cell membrane [8]. In mesoscale domains, molecular interactions play important roles in both thermal fluctuations and weak cooperativity which are critical for various functions

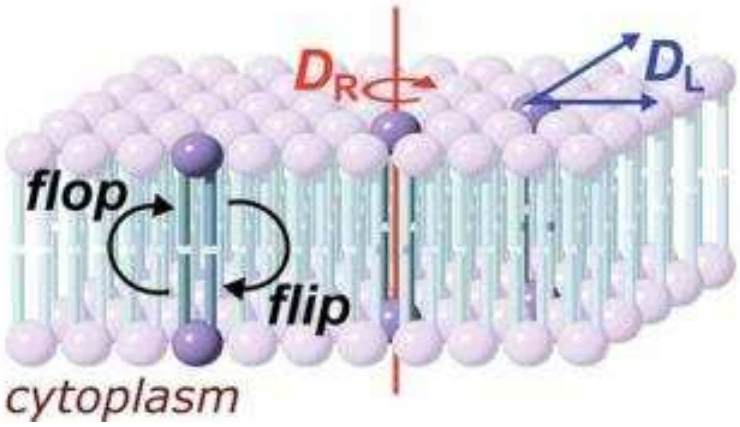

Figure 1.2: Diffusion processes of membrane molecules: Translocation (flip-flop), lateral diffusion (D_L) and rotational diffusion (D_R). From Sanderson, 2012 [5].

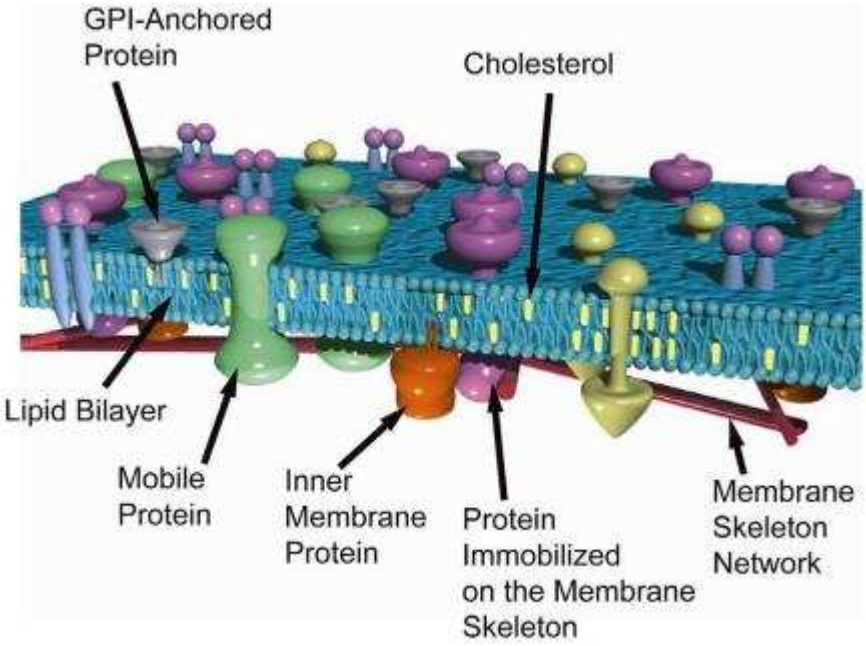

Figure 1.3: Schematic representation of the complexity of the membrane. The plasma membrane consists of a lipid bilayer with embedded cholesterol and proteins. The proteins are either free to move or bound to the actin-based cytoskeletal network. From Ritchie *et al.*, 2003 [7].

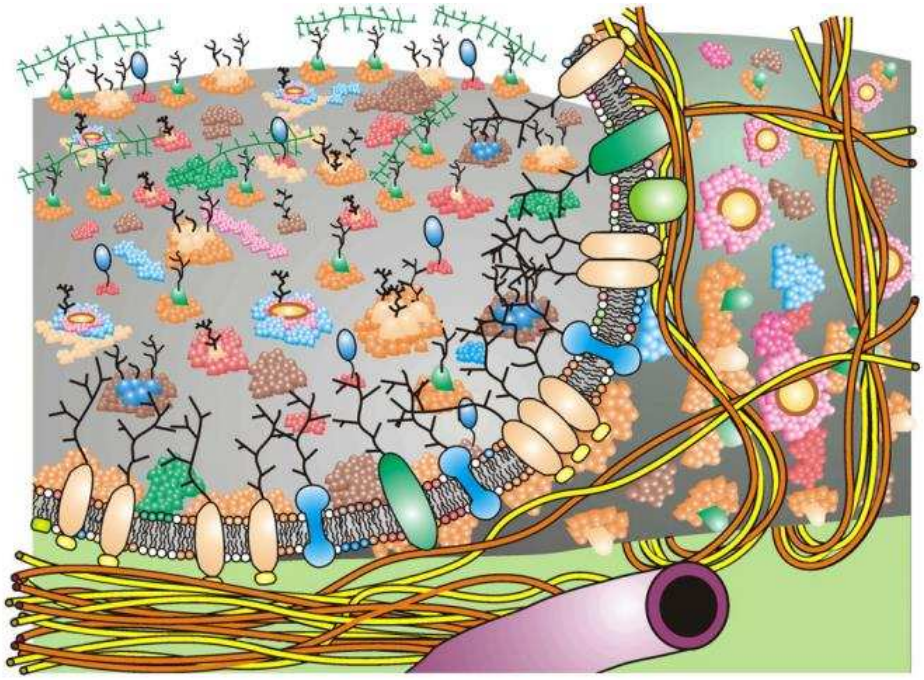

Figure 1.4: Fluid-mosaic cell membrane model that contains updated information on membrane skeleton, extracellular and membrane domain. From Nicolson *et al.*, 2014 [6].

and molecular events in the plasma membrane. There are three mesoscale domains which serve as membrane compartments (40–300 nm diameter), raft domains (2–20 nm) and dynamic protein complex domains which contain oligomers and greater complexes of membrane-associated and cell surface receptors with sizes generally between 3 nm and 10 nm but as large as several hundred nanometers. Raft domains have been extensively characterized and are known to be enriched in cholesterol, glycosphingolipids, and glycosyl-phosphosphatidylinositol (GPI)-anchored proteins and defined by cytoskeletal structures. Figure 1.5 shows the three types of cell membrane domains.

I.B. Dynamics of cell membrane proteins

Plasma membrane receptors are integral membrane proteins with diverse structures and functions which bind specific ligands to trigger cellular responses. These receptors can be broadly classified as G-protein coupled receptors, ion channel-linked receptors and catalytic receptors [9]. Receptors are inserted in the fluid phase of the lipid bilayer and are capable of rotational and lateral motion within the bilayer. Due to compartmentalization of the plasma membrane and the formation of membrane microdomains, receptors are distributed non-homogeneously in the cell membrane bilayer. Thus both lateral and rotational diffusion of membrane receptors reflects different kinds of intermolecular interactions within the plasma membrane environment. Understanding protein diffusion within the membrane is very important to further understanding biomolecular interactions *in vivo* during complex biological processes including receptor-mediated signaling.

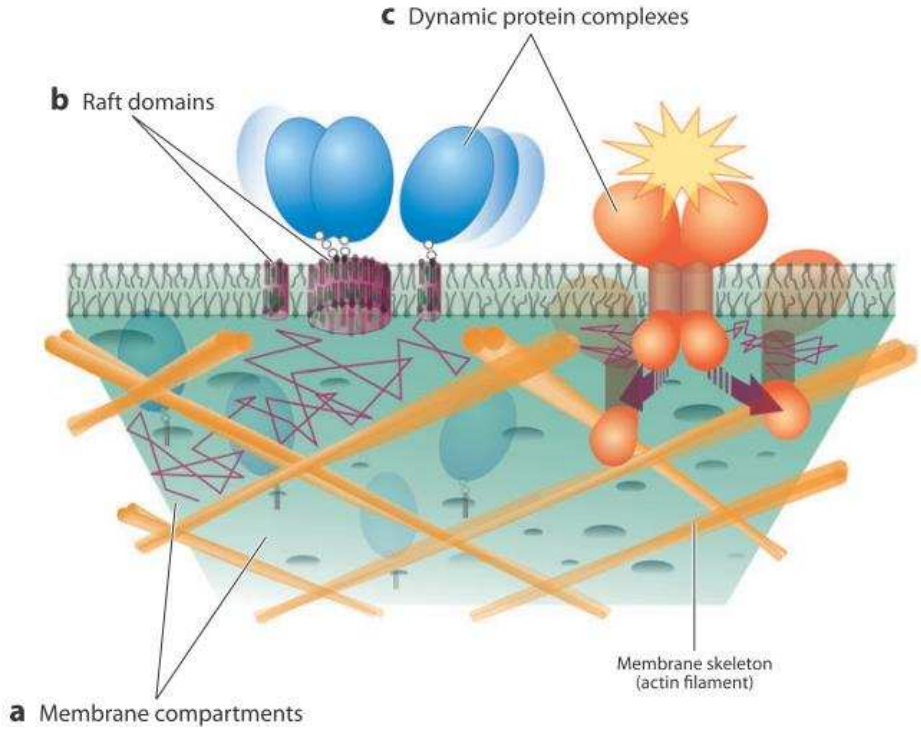

Figure 1.5: Three types of mesoscale domains of cell membrane. (a) Membrane compartments generated by the partitioning of the entire plasma membrane. (b) Raft domains with sizes limited by the membrane compartments. (c) Dynamic protein complexes domain composed of oligomers of integral membrane proteins. From Kusumi *et al.*, 2012 [8].

I.B.1. Lateral diffusion

Redistribution of surface proteins after binding ligands and antibodies in the plasma membrane indicate that the receptors interact with each other at specific locations in the cell membrane and transit information that starts the cascades leading to signaling processes [10]. Frye and Edidin first demonstrated lateral mobility of membrane proteins in 1970 using antigen markers. Their results, used by Singer and Nicolson in the development of the Fluid Mosaic Model [4], showed that the cell membrane is fluid and that there is lateral diffusion of surface antigens [11]. However, because of membrane compartmentalization and the formation of membrane microdomains, most receptors have diffusion coefficients that are ten to one hundred-fold slower than predicted for freely diffusing molecules [5, 12-15]. Lateral diffusion measurements of cell membrane receptors are possible at the single molecule level. This has been demonstrated for individual molecules in the plasma membrane by Kusumi and his coworkers [16] who studied the mobility of E-cadherin, epidermal growth factor receptors and transferrin receptors in the plasma membrane of a mouse keratinocyte cell line using single particle tracking (SPT) methods. For these studies, they labeled the receptors with 40 nm colloidal gold particles and tracked the movements of the gold particles using differential interference contrast (DIC) microscopy. Single molecule dynamics were compared with lateral motions measured for groups of molecule using fluorescence photobleaching recovery (FPR). They found that particles undergoing Brownian diffusion were confined within a limited area that was defined by the membrane-associated cytoskeleton. The data obtained by SPT and FPR also suggested that the plasma membrane is compartmentalized into many small domains 300-600 nm in diameter and receptors can move successively to adjacent compartments [16]. The confined diffusion also has been confirmed by other similar studies [17, 18]. Receptors have

been shown to diffuse freely in limited size compartments with infrequent "hops" to new compartments. The main lateral movements of cell membrane receptors are divided to four modes that include transient confinement by obstacles or by the cytoskeletal meshwork in defined areas [8, 16], directed motion by direct or indirect attachment to the cytoskeleton and random diffusion in the fluid cell membrane [19]. Figure 1.6 shows four kinds of diffusion movements of cell membrane receptors.

The average diffusion time in a compartment depends on the degree of protein oligomerization or association with other membrane proteins. With sufficient clustering, receptors can be completely confined to a single compartment. Figure 1.7 shows the oligomerization-induced trapping model for membrane receptors upon oligomerization or molecular complex formation. Receptor monomers may hop across the "picket-fence" formed by the cytoskeleton and associated proteins easily but, upon oligomerization, complexes are likely to have a much slower rate of hopping between compartments [20, 21]. Thus, oligomerized receptors can exhibit substantially restricted diffusion. Complexes presumably protrude deeper into cytoplasm than the receptor cytoplasmic domain alone and so interact more strongly with the membrane cytoskeleton. Thus active receptors and/or aggregates tend be restricted to smaller compartment sizes and/or have longer residence time within compartments [22].

I.B.2. Protein rotational diffusion

The rate of lateral diffusion reflects protein motion over macroscopic distances of one micrometer or slightly less and, moreover, lateral diffusion rates are only logarithmically dependent weakly on the molecular weight of the diffusing entity [23]. In comparison with

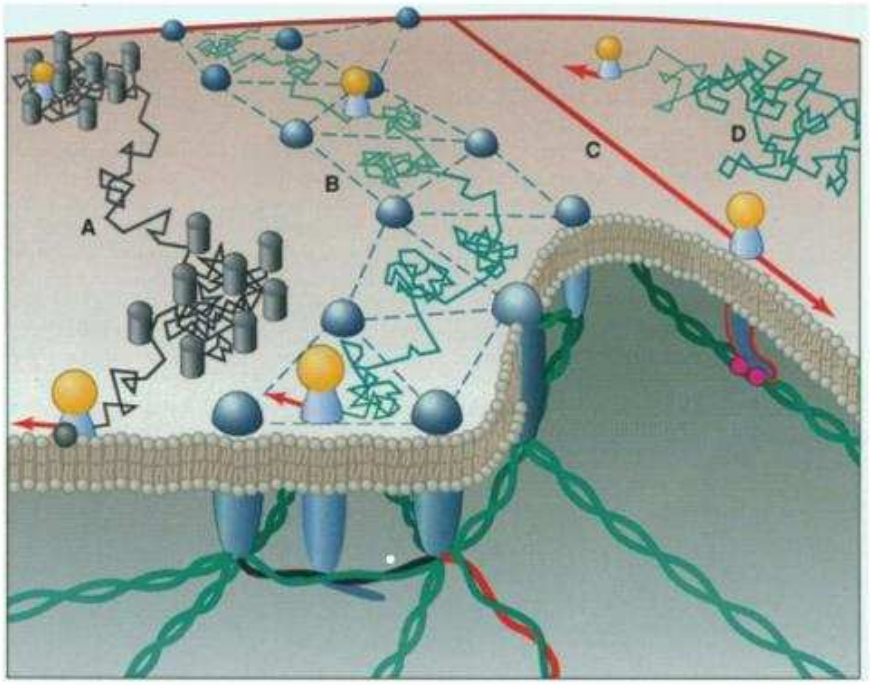

Figure 1.6: Four kinds of lateral movement seen for cell membrane receptors: Transient confinement by obstacle clusters (A), transient confinement by the cytoskeleton (B), directed motion by attachment to the cytoskeleton (C) and random diffusion in the cell membrane plane (D). From Jacobson et al., 1995 [19].

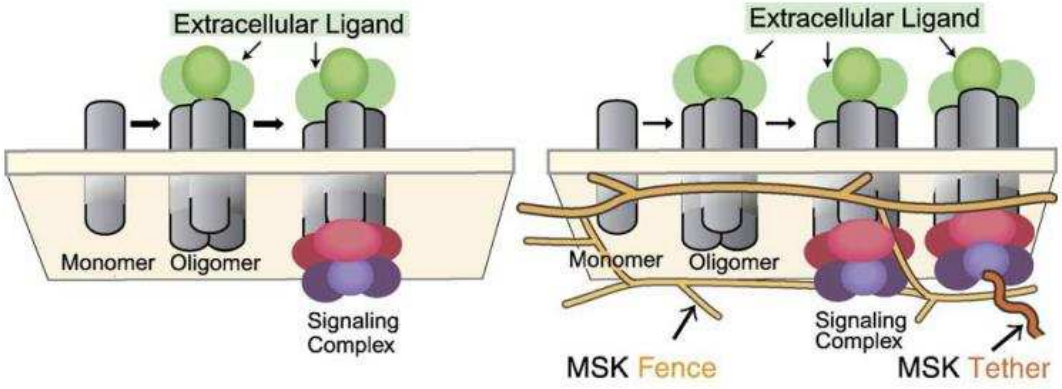

Figure 1.7: Oligomerization-induced trapping model for membrane receptors upon oligomerization or molecular complex formation. From Kusumi and Suzuki, 2005 [22].

lateral diffusion, the protein rotational correlation time varies according to the in-membrane volume of the rotating protein [24, 25]. In particular, for a spherical particle of volume V in a medium of viscosity η, this correlation time is 6ηV. Thus measurements of rotational motions are highly sensitive to the shape and size of the protein and as well as to the viscosity of the surrounding environment. For these reasons, rotational diffusion measurements provide a rather sensitive method to investigate the structure of large macromolecular complexes and are sensitive enough to reveal receptor oligmerization and aggregation events [26-28]. Moreover, studies of rotational diffusion in living cells may help researchers reveal the causes of diseases such as Alzheimer's [29] and facilitate development of effective drug targeting and gene delivery.

Rotational motions of cell membrane receptors occur essentially around their long axis perpendicular to the plane of the membrane [30]. Like lateral diffusion, the rotational diffusion of cell surface receptors also has mobility restrictions; many membrane receptors rotate rapidly only when the receptor has no cytoskeletal interactions or the cytoskeleton is disrupted [31, 32]. Cone demonstrated rotational motion of membrane proteins in 1972 using a method based on rapid absorption changes from flash illumination of the rhodopsin molecule located in rod outer segment membranes. His results showed that rhodopsin was rotating with a 20 μsec relaxation time [33], a result experimentally verified by Chapman and co-workers in 1973 [34].

I.C. Measuring molecular rotation with dye labels

To measure rotation of a particular receptor type on a selected single cell, only optical methods have adequate sensitivity. All such optical approaches to measuring molecular rotation involve measuring polarization of light emitted from molecules, since only polarization phenomena reflect the orientation of molecules involved. Rotational diffusion can be evaluated

through changes in fluorescence polarization over time as computed through two different functions derived from experimental data. Raw data are obtained by exciting fluorophores using polarized light and recording emitted fluorescence intensities $I_{\parallel}$ and $I_{\perp}$, polarized parallel and perpendicular with respect to exciting light polarization [35]. Figure 1.8 is a schematic diagram showing the measurement of anisotropy. The orientation of the fluorophore can provide interesting information about the molecule to which the fluorophore is attached.

The first function reflecting molecular orientation is polarization p, defined as a function of the observed parallel $I_{\parallel}$ and perpendicular intensities $I_{\perp}$

$$p = \frac{(I_{\parallel} - I_{\perp})}{(I_{\parallel} + I_{\perp})} \tag{1.1}$$

While fluorescence emission anisotropy r is defined as

$$r = \frac{(I_{\parallel} - I_{\perp})}{(I_{\parallel} + 2I_{\perp})} \tag{1.2}$$

These two functions contain the same information but are most useful in different circumstances, polarization for measurements in a 2-dimension measurement geometry like that of a microscope and anisotropy for a 3-dimensional optical system like a T-format fluorometer. Different detection efficiencies are introduced into the measurements when collecting $I_{\parallel}$ and $I_{\perp}$ in different channels. A correction factor called the g-factor (g) is used in anisotropy calculations [36] and is defined as

$$g = I_{vv} / I_{vh} \tag{1.3}$$

where I_{vv} and I_{vh} are emitted fluorescence intensities polarized parallel and perpendicular with respect to vertically polarized exciting light respectively. Then, r becomes

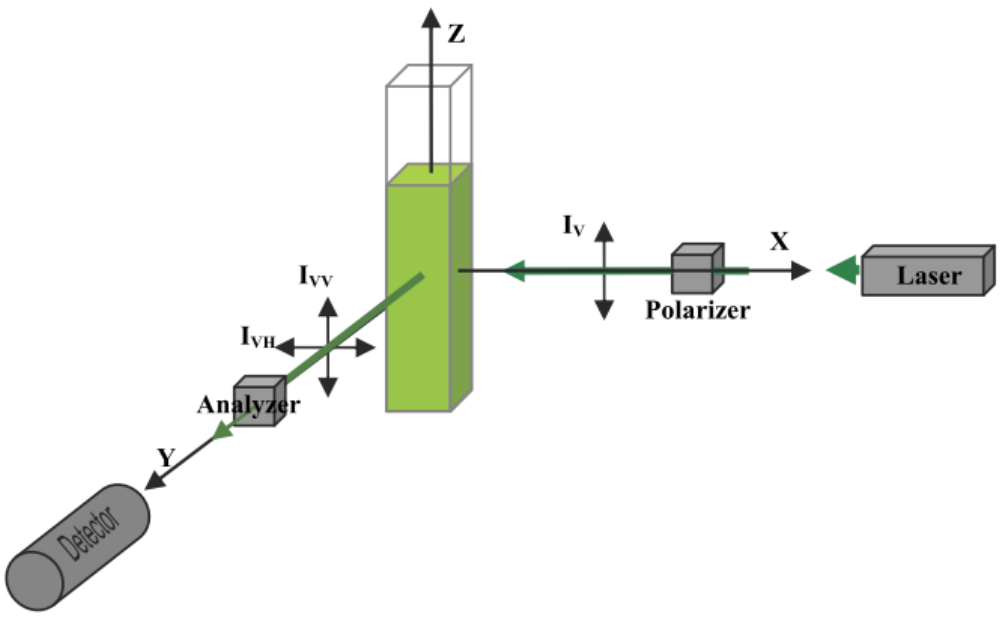

Figure 1.8: Schematic diagram of instrumentation for the measurement of anisotropy. Exciting light travels along the x direction and is polarized along the z direction. The polarized exciting light will be absorbed by the fluorophore and the fluorescence is split into two channel, each of which is used to measure horizontally polarized intensity $I_{\parallel}$ and vertically polarized $I_{\perp}$ light. From Lakowicz, 2006 [35].

$$r = \frac{(I_{\|} - gI_{\perp})}{(I_{\|} + 2gI_{\perp})} \tag{1.4}$$

In comparison with lateral diffusion measurements, protein rotational diffusion measurements are much more difficult. Although rotational diffusion can be measured through optical methods in various ways [37, 38], only a very few methods can be applied to molecules *in vivo*. Most such measurements have employed time-resolved phosphorescence anisotropy (TPA) or fluorescence depletion anisotropy (FDA). These techniques use fluorescent dye molecule as probes. Molecules with their absoption dipole parallel to the polarization of the incoming light are preferentially excited via photoselection. Anisotropy is detected as polarization of light emitted from molecules in the excited state. Figure 1.9 shows photoselection of fluorophores. We can calculate the rotational diffusion of the molecule by analyzing the polarization dependence of the emitted fluorescence over time when the molecules have been excited by linearly polarized light.

I.C.1. Time-resolved phosphorescence anisotropy.

Time-resolved phosphorescence anisotropy (TPA) uses phosphorescent dyes such as erythrosin isothiocyanate (ErITC) or eosin isothiocyanate (EITC) which have triplet-state, and therefor phosphorescence, lifetimes up to 1 ms. Such long lifetimes are essential because the rotation of unhindered protein in cell surfaces is on the order of 100 us and the label dyes must emit luminescence throughout the rotational decay of the molecule to which the probe is attached.

These dyes can be conjugated to an antibody, lectin, or hormone which, in turn, binds the membrane protein of interest. This technique has been used extensively to measure the rotational

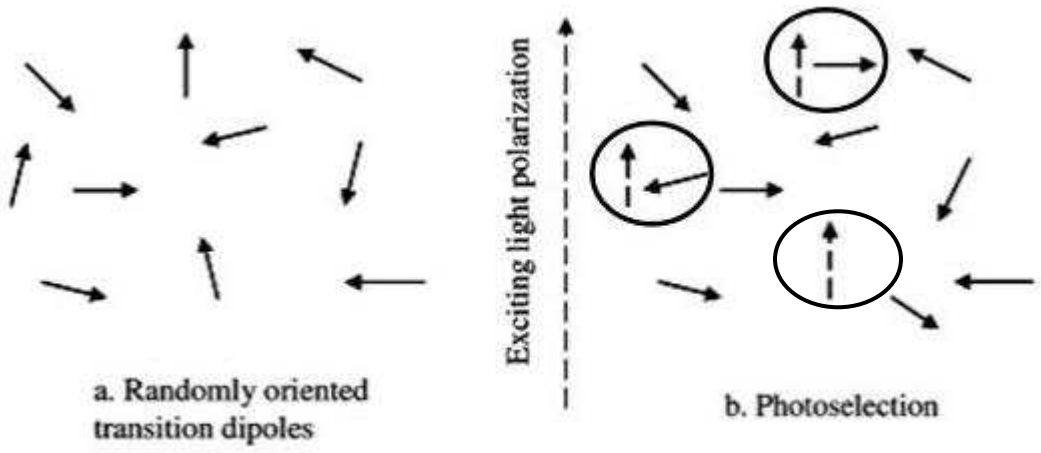

Figure 1.9: Photoselection of fluorophores. Panel a. Fluorophores with randomly-oriented transition dipoles. Panel b. When shining polarized light on fluorophores, a subset of the fluorophores are oriented parallel to the polarization of the exciting light and are excited via photoselection.

diffusion of macromolecules on living cell surfaces. Austin *et al.* in 1979 were the first group to perform time-resolved rotational diffusion measurements on intact cells. They examined the rotational diffusion of eosin-concanavalin A bound to mouse spleen cells transformed with Friend erythroleukemia virus using time-dependent phosphorescence emission intensity and measurement of the anisotropy of eosin excited by a 5 nsec laser pulse. From this and other studies, total polarized luminescence has been shown to provide information about rotational motions in the range of about 0.1 nsec to 1 sec [39].

Figure 1.10 is a diagram showing how TPA measurements work. In TPA the linearly polarized output from a sub-μsec laser pulse excites the subset of phosphor molecules oriented along the laser polarization axis. Subsequent phosphorescence is polarized along molecule's current transition dipole. Molecular orientation at time of emission is measured. The polarization decays as rotational motion randomizes phosphor orientation prior to phosphorescence emission. Anisotropy decays exponentially in time as $r = r_\infty + (r_0 - r_\infty) \exp(-t/\varphi)$ when phosphor-labeled molecules re-orient after the pulse. The rotational parameters of interest, especially rotational correlation time φ, can be obtained from the emission anisotropy function.

I.C.2. Fluorescence depletion anisotropy.

Fluorescence depletion anisotropy (FDA) was first described by Johnson and Garland [40, 41]. This method combines the high sensitivity of fluorescence detection with the long lifetimes of molecular triplet states to measure rotational motions on the 10 μsec to 1 msec or longer timescale. In this method, a dye like eosin that has substantial quantum yields both for prompt fluorescence and for triplet formation is excited by a nanosecond pulse of polarized light. The sample is then probed by a continuous beam of light polarized either parallel or perpendicular to

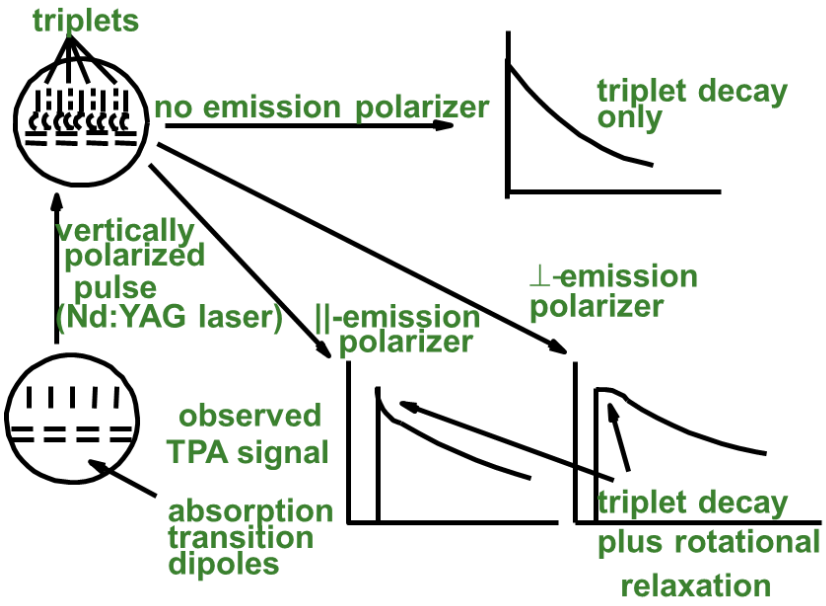

Figure 1.10: Concept of time-resolved phosphorescence anisotropy (TPA). The linearly polarized output from a sub-μsec laser pulse excites the subset of phosphor molecules oriented along laser polarization. Subsequent phosphorescence is polarized along molecule's current transition dipole. Molecular orientation at time of emission is measured.

the pump pulse to excite fluorescence. The signal is initially depleted by triplet formation but then recovers as triplets decays to the ground state and thus become available for fluorescence excitation. FDA overcomes the low sensitivity of phosphorescence-based techniques such as TPA. It can be used for single cell measurements and improves sensitivity by perhaps 100-fold. The technique has been used to measure protein rotation on erythrocyte ghosts [37] and suspensions of A431 cells [42]. This method has also been used to study protein rotation on individually selected intact mammalian cells [43-47].

I.C.3. Time-resolved fluorescence anisotropy

Dye molecules and fluorescent proteins rotate extremely rapidly in solution on the nanosecond timescale. In such cases, fluorescence lifetime are long enough to allow rotation measurements by the anisotropy decay of their fluorescence. This is most conveniently measured by time-correlated single-photon counting (TCSPC), a sensitive method for measuring fluorescence kinetics with a time resolution of tens to hundreds of picoseconds. In this technique, the arrival times of a fluorescence photons after repetitive excitation pulses are measured and these times used to generate a histogram which is effectively a fluorescence decay curve. Rotational information can be obtained by comparing decay curves for signals where detector polarization is parallel and perpendicular to the excitation [48]. The apparatus for TCSPC measurements includes a photon detector, a pulsed excitation source and an electronic circuit. In TCSPC measurements the information from fluctuations on the microsecond to second timescale is discarded. Time-tagged TCSPC is a data collection mode of TCSPC which is performed using the arrival times of each individual photon from the start of the experiment instead of building up photon distributions (Figure 1.11). Time-tagged TCSPC can be used to examine the slow

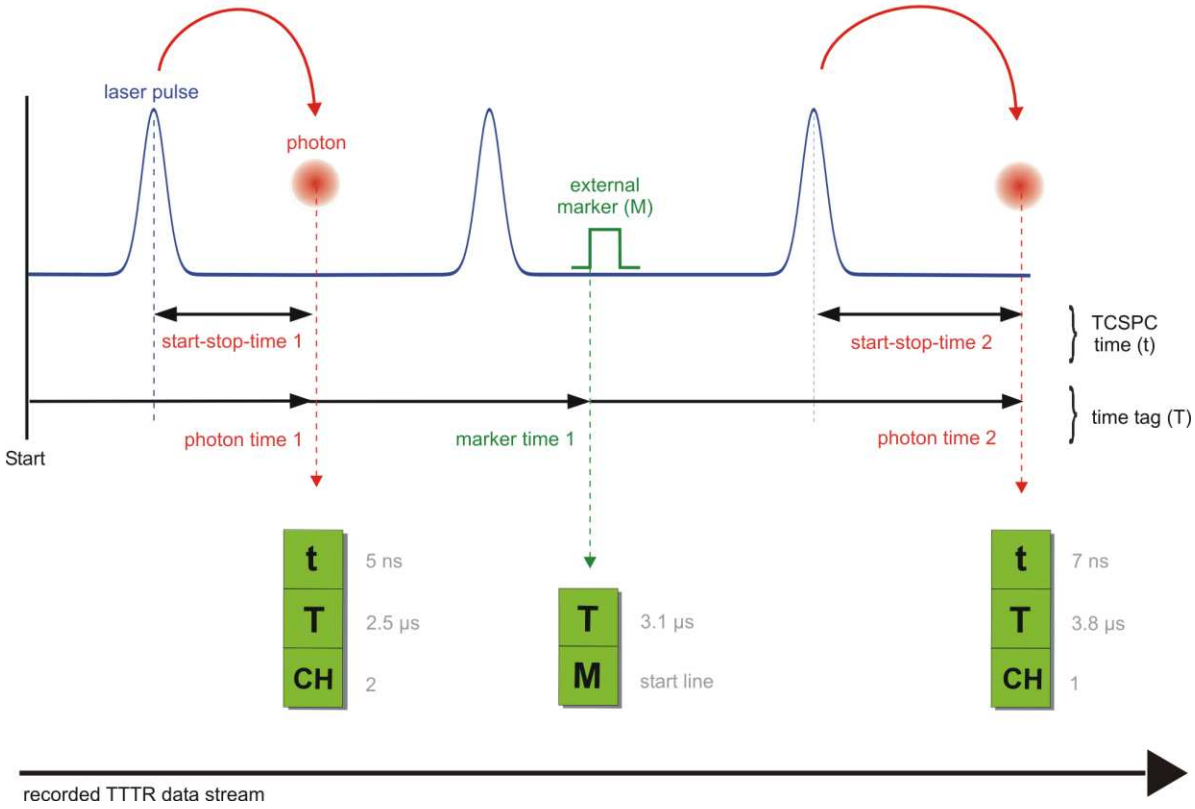

Figure 1.11: Scheme of time-tagged TCSPC data collection mode. The start-stop events in TCSPC are stored directly along with additional time information, the time tag (T). The time tag represents the macroscopic arrival time of the photon with respect to the beginning of the measurement. Courtesy of PicoQuant GmbH, Berlin, Germany.

fluctuations in flurescence lifetime and anisotropy and it is particularly important in study dynamics of complex cell system at the single-molecule level [49].

I.D. Rotation measurements using nanoparticle probes

I.D.1. Quantum dots

Quantum dots (QD) can be to evaluate lateral and rotational diffusion of membrane components. It is necessary to tag the cell surface receptors of interest with a highly visible probe for observation against the strong background signal that exists in *vivo.* QDs are fluorescent semiconductor nanocrystals that have unique optical properties [50-53] that make them attractive probes to study the receptors of cell surface. QDs are often superior to traditional fluorophores due to their wide absorbance and narrow emission spectra which can be easily controlled by varying dot size (Figure 1.12). Resistance to photobleaching makes QDs useful for most fluorescence studies. Although QDs have been shown to photobleach under intense laser [54, 55] or arc lamp illumination [56], in comparison with fluorophores, QDs reach a permanent dark state gradually. QDs have high quantum yields that make them much brighter than fluorophores [57]. QDs also have long fluorescent lifetimes on the order of a few tens of nanoseconds after excitation, while the fluorophores are limited by their lifetime which is typically <10 ns. This means that QDs have high signal-to-noise ratio and can be used with time-gated imaging [58].

QDs are about 2 to 10 nm wide, and contain a few hundred to a few thousand atoms [59]. QDs for biological applications are made with a cadmium selenide (CdSe) core and a zinc sulfide (ZnS) shell. The ZnS shell protects the core surface from oxidation surrounding solution [61]. Surface coatings are able to reduce nonspecific interactions and can be designed for

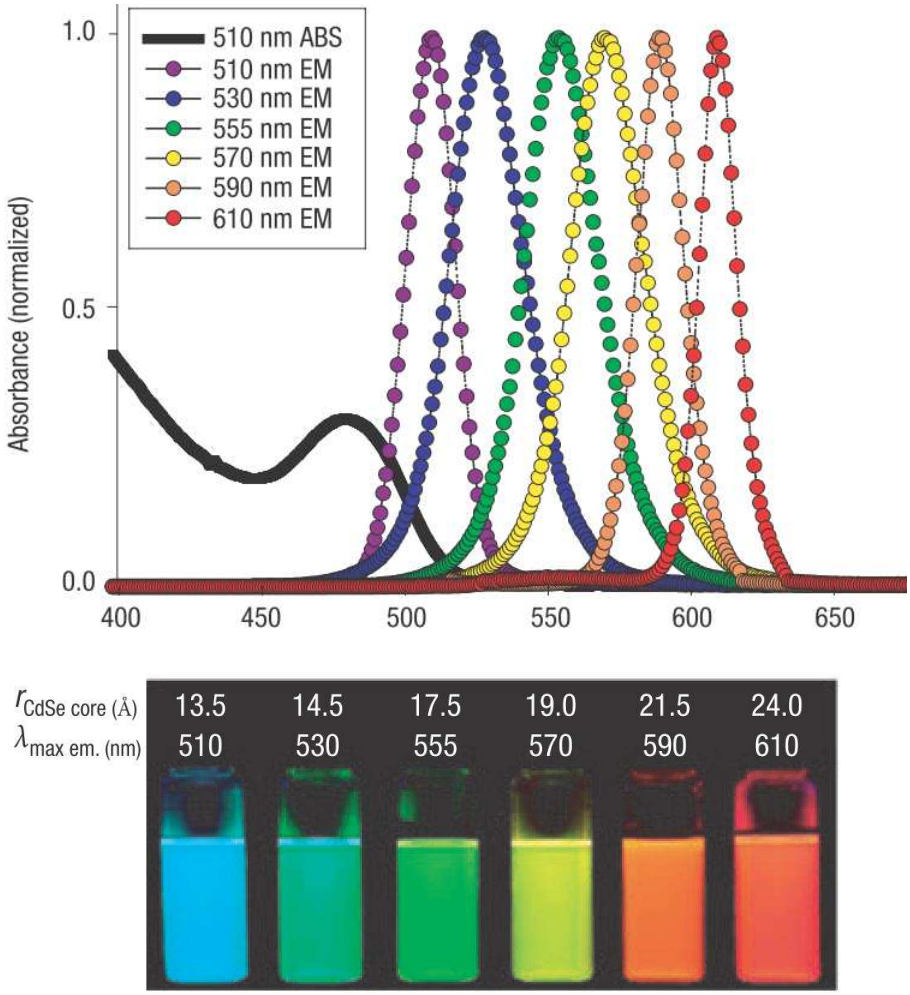

Figure 1.12: Absorption and emission of six different QD dispersions (top panel), and a picture demonstrating the size-tunable fluorescence properties and spectral range of the six QD dispersions plotted in top versus CdSe core size (bottom panel). Adapted from Medintz *et al.*, 2005 [60].

conjugation of biomolecules [62]. Outer organic coatings can be peptides, amphiphilic micelles or polymers. Biomolecules can be streptavidin, DNA, or antibodies which are conjugated to biological targets by specific binding [50] (Figure 1.13).

One property that limits QD utility in time-dependent measurements of protein rotational diffusion is QD "blinking". The phenomenon of QD blinking was first described by Nirmal *et* al. in 1996 [63]. Individual QDs display intermittent blinking with continuous excitation, alternating between an emitting state (on) and a non-emitting state (off) with blinking timescales ranging from nanoseconds to hundreds of seconds [52, 64]. The presence of a single QD can be confirmed from this blinking. Figure 1.14 is an intensity time trace of a single dot which shows the random alternation between "on" and "off" states of blinking. Low molecular weight agents such as mercaptoethylamine, dithiothreitol and β-mercaptoethanol have been reported to partially reduce QD blinking [65-67]. Non-blinking CdZnSe/ZnSe QDs have been reported, but these QDs are not useful because they have very broad emission spectra [68]. Keller and coworkers exploited non-blinking 'giant' QDs to study IgE-FcεRI receptor lateral motion in live cells using a confocal-based 3D single particle tracking microscope [69]. However these giant QDs are not suitable for measuring the rotational motions of individual molecules.

The on/off time distribution for quantum dot blinking follows power-law statistics, and is unchanged for sample temperature, nanoparticle shape and excitation intensity of the QD [70]. The blinking "off" time periods τ are described by a probability distribution that follows the power law [71] below where the exponent α is typically between 1 and 2.

$$P(\tau) \propto \tau^{-\alpha} \tag{1.5}$$

Several models have been proposed to explain QD blinking. Efros and Rosen proposed Auger ionization model in 1997 to explain the dark state in QDs [72]. They suggested that long-

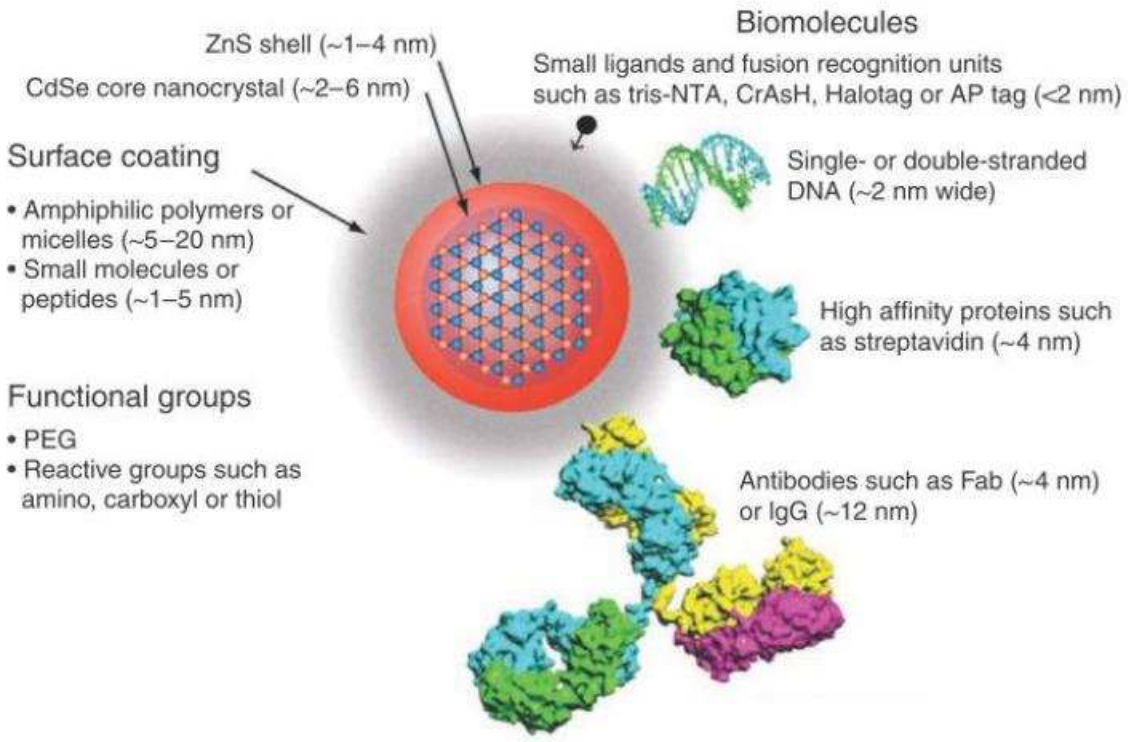

Figure 1.13: Schematic representation of a QD probe. The inorganic CdSe core nanocrystal and ZnS shell (red) dictate the optical properties in a size-dependent manner. Organic surface coatings or biomolecules are shown in gray. Adapted from Pinaud *et al.*, 2010 [50].

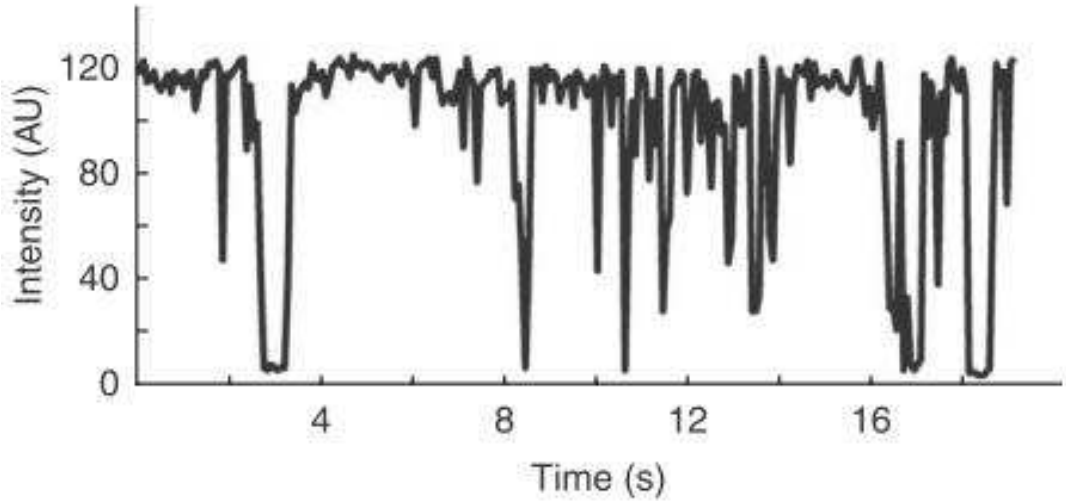

Figure 1.14: Quantum dot blinking. The intensity time trace indicates the random alternation between "on" and "off" blinking states which is a feature of fluorescence from an individual QD. Adapted from Pinaud *et al.*, 2010 [50].

lived electron trapping results in blinking. The trapping and detrapping of electrons regulates the changes between "on" and "off" state which are governed by Auger processes. Most recently Frantsuzov and co-workers proposed a phenomenological model of multiple recombination centers (MRC) to account for blinking [73]. The model considers the nonradiative relaxation of QD excitation through multiple recombinations. Voznyy and Sargent have proposed the atomistic model where surface vacancies in the QD improve the quantum yield in comparison with the vacancy-free surfaces. Dynamic vacancy aggregation is able to turn fluorescence off temporarily. They found that the vacancies can be stabilized by foreign cations; the cations can inhibit blinking and improve quantum yield [74].

Compensating for QD blinking is a challenge in lateral diffusion measurements such as single particle tracking where an "off" state leads to interruptions in QD-tagged receptor tracking. However, trajectories in which QDs stay "on" can be selected to determine the lateral coefficients for receptors of interest [75]. For rotational motion measurements, it is even more critical to remove the effects of blinking to obtain correct rotational diffusion time for molecules of interest, a problem which is addressed in this dissertation.

I.D.2. Gold nanoparticles

Rotational motion of membrane proteins can only be measured within a critical time window that is determined by the limited lifetime of fluophore. Traditional TPA methods can only measure rotational diffusion times comparable to the luminescence lifetime of the probe, typically <500 μs for phosphors like erythrosin, and so provide little information on motions slower than about 5ms. Polarized photobleaching requires at least 100 ms to bleach fluophores and cannot be used to examine faster rotational motions.

The development of rod-shaped nanoparticles make it possible to measure rotational dynamics of individual molecules *in vivo*. The commonly-used rod nanoparticles are gold nanorods and asymmetric fluorescent nanocrystals including commercial quantum dots. These probes are small enough not to perturb the rotation of proteins to which they are attached. Quantum dots emit fluorescence polarized along the long axis of the rod while gold nanorods scatter light polarized along the long axis of the rod. Compared with dye molecules, gold nanorods produce several orders of magnitude higher absorption and scattering cross section [76]. Quantum dots have superior optical properties with brightness and resistance to bleaching.

Nanoparticle rotational motion can be directly monitored using suitable techniques and rotational information from spontaneous orientational fluctuations of single molecules can be obtained. Figure 1.15 shows an asymmetric nanoparticle with polarized fluorescence emission or polarized scattered light along its axis. It is possible to measure such signals through two orthogonal polarizers. The two detector signals would vary but their sum would be constant. The polarization would reflect orientation independent of any change in light source intensity [77].

Rotational motion measurement of gold nanorods was first performed using dark field microscopy by Sönnichsen and Alivisatos [77]. Gold nanorods were attached to a glass surface in a solution with pH 8.0. They demonstrated time resolution of msec and an observation times of hours by observing the two-dimentional rotational diffusion of gold nanorods confined at the interface of glass and water. Pierrat and his coworker monitored rotational diffusion of polymer-coated gold nanorods attached to artificial biomembranes on solid supports using polarization contrast microscopy [78]. Rotational diffusion times of about 100 msec could obtained depending on the biotin concentrations in the membrane. Spetzler and his coworkers observed

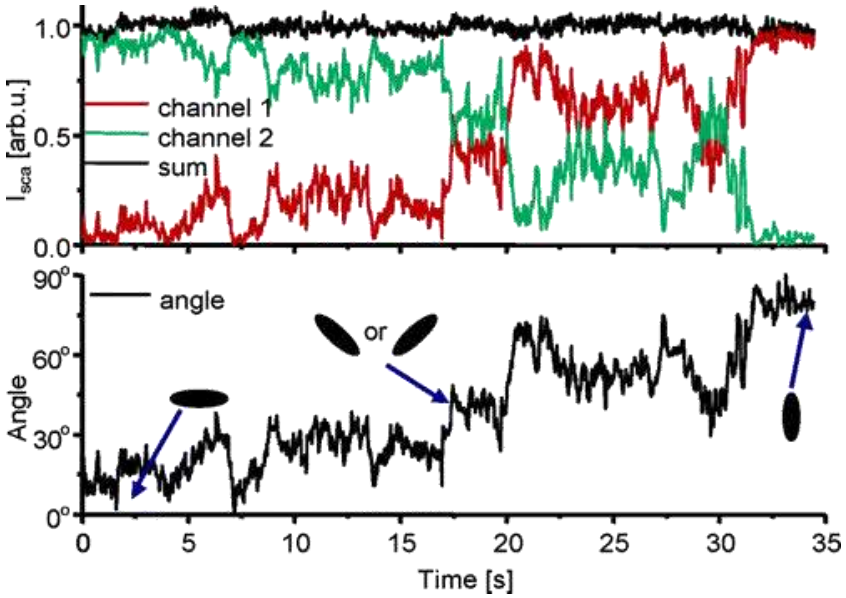

Figure 1.15: Time traces of the intensity and orientation of the gold nanorod. Upper panel: Time traces of the intensity observed for the two orthogonal polarization channels of an individual gold nanorod (green/red). The intensity adds up to an almost constant total intensity (black). Lower panel: The orientation (angle) of the rod may be computed from the relative intensity in the two channels. Adapted from Sönnichsen *et al.*, 2005 [77].

the rotation of ATPase molecular motors using dark-field microscopy. A single gold nanorod was attched to the rotating γ-subunit of an immobilized F1-ATPase molecule on a glass slide. They measured rotation rates of 7.62 rad/ms with a time resolution of 2.5 μsec. Histograms of scattered light intensity from ATP-dependent nanorod rotation as a function of polarization angle allowed the determination of the nanorod orientation with respect to the axis of rotation and plane of polarization. Figure 1.16 shows consecutive dark-field micrographs of a stationary nanorod and a schematic representation of a nanorod attached to the F1 γ-subunit [79]. Chang and his coworkers determined the rotational motion of gold nanorods using a polarization-sensitive instrument to measure the orientation of a 25×73 nm nanorod from either the longitudinal or the transverse surface plasmon resonance. The gold nanorods were deposited on a glass slide and surrounded by water [80].

Wang and coworkers were the first investigators to successfully use gold nanorod probes to track the rotational motions of proteins on a live cell. They used Nomarski-type differential interference contrast (DIC) microscopy and anisotropic gold nanorods. The TAT-modified gold nanorods were internalized by A549 human lung cancer cells and transported by the cytoskeleton. They monitored the intensities of the black and white components of nanorod and obtained dynamic orientation information from gold nanorods involved in cell transport processes [81]. Figure 1.17 shows the DIC images of two 25 nm x 73nm gold nanorods at different orientations in 2D space. Xiao and coworkers directly tracked the rotational diffusion of individual nanorods being transported by kinesin motor protein along microtubule networks inside live cells. They illuminated gold nanorods with two orthogonal sheets of light instead of using dark-field illumination. This method allowed determination of three-dimensional orientation of single gold nanorod [82].

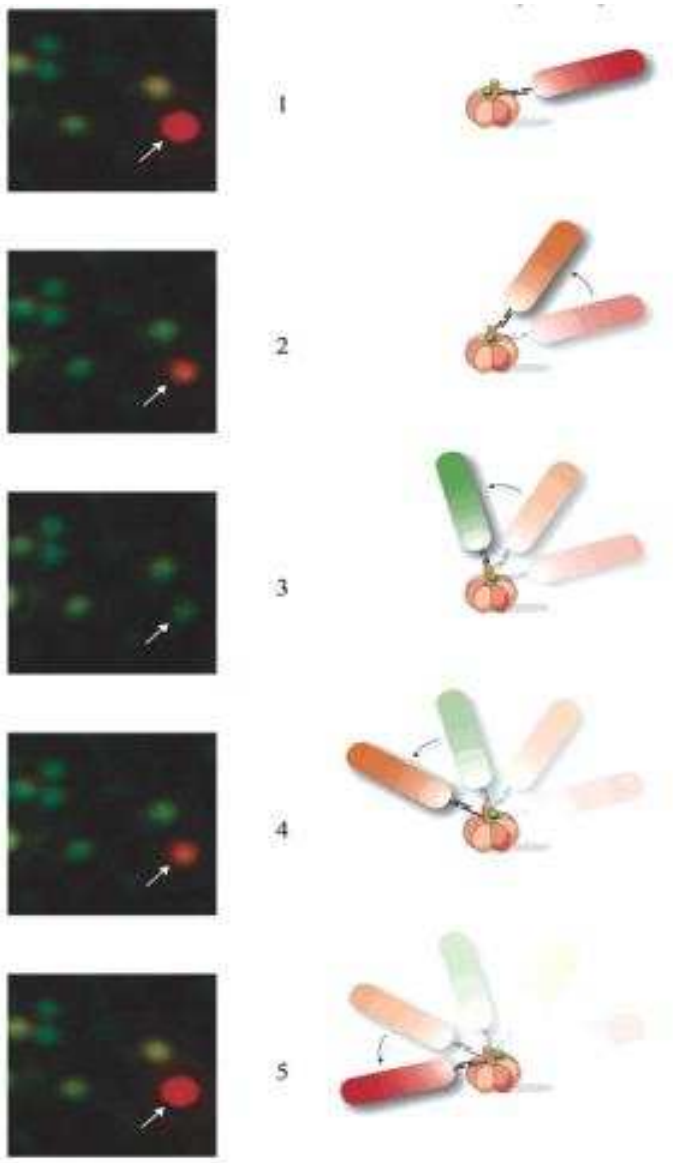

Figure 1.16: Consecutive dark-field micrographs of a stationary nanorod. These images Correspond diagrams of a nanorod attached to the F1 γ-subunit, the rod demonstrates rotation from position 1 where rotates when (1) the plane of polarization is parallel to the long axis of the rod. In 2-5, the filter was rotated in 45° increments. Adapted from Spetzler *et al.*, 2006 [79].

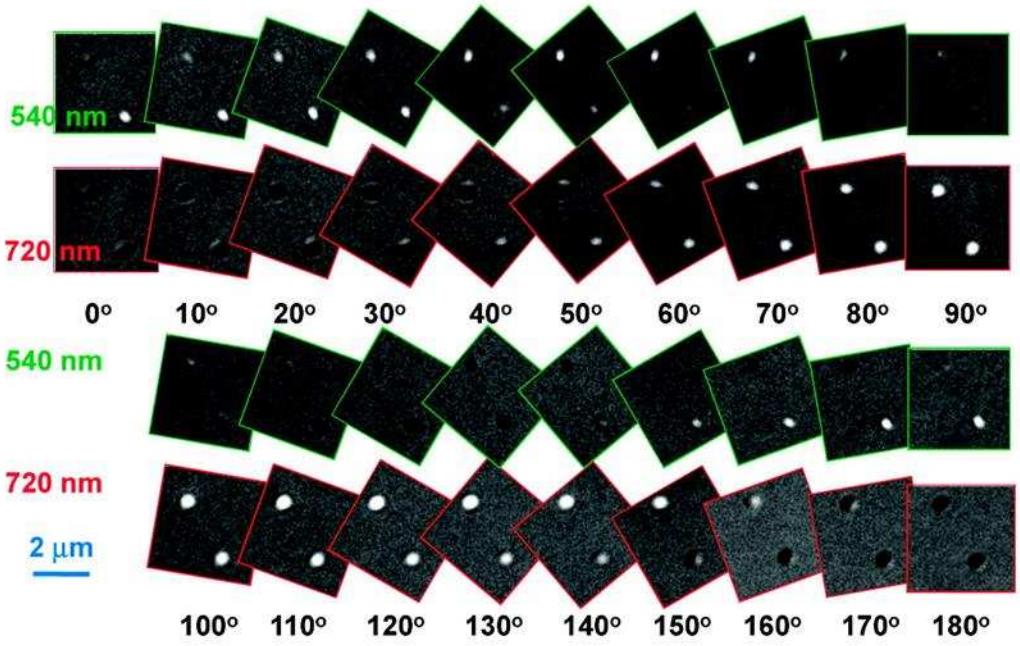

Figure 1.17: DIC images of two 25 nm x 73nm gold nanorods at different orientations in 2D space. Adapted from Wang *et al.*, 2006 [81].

I.E. Type I Fcε Receptor as a model system for rotation studies

The Type I Fcε Receptor **(**FceRI) as expressed on RBL-2H3 mucosal mast cells is a useful model system for studying protein rotational diffusion. The protein is a high-affinity receptor for the Fc portion of IgE. IgE is a sub-type of antibody molecules that is characterized by two identical heavy chains and two identical light chains. Figure 1.18 shows a schematic diagram of a typical antibody. Each arm of the antibody is composed of four domains: two variable domains (VH, VL) and two constant domains (CH, CL). The variable domains are connected to the constant domains. The variable domains provide the immune system with the ability to target foreign invaders via amino acid sequences that vary from one antibody molecule to another. Heavy chains of IgE are denoted by the corresponding lower-case Greek letter ε. The antigen binding site is formed where a heavy chain variable domain (VH) and a light chain variable domain (VL) come close together. The heavy chain contains 2 regions; the Fab (antigen-binding portion) and Fc (constant region).

FcεRI, a prototypic activating receptor, is composed of an immunoglobulin E (IgE) binding subunit consisting of a single membrane-pass α-subunit, the four membrane-pass β-subunits which contains a single immunoreceptor tyrosine-based activation motif (ITAM), and two γ-subunits, which exist as a disulfide-linked homodimer and contain one ITAM on each subunit [83]. The α-subunit of the FcεRI forms the binding site for the Fc region of IgE. β and γ subunits are the functional signal transduction units of FcεRI.

FcεRIs expressed on mast cells and basophils are responsible for allergic reactions triggered by allergens and play a role in the pathogenesis of allergies. FcεRI bind IgE with a stoichiometry of 1:1. Receptor crosslinking by polyvalent allergen initiates a signaling cascade leading to mast cell degranulation, *i.e.* the release of vesicle contents from the cell. Chemical

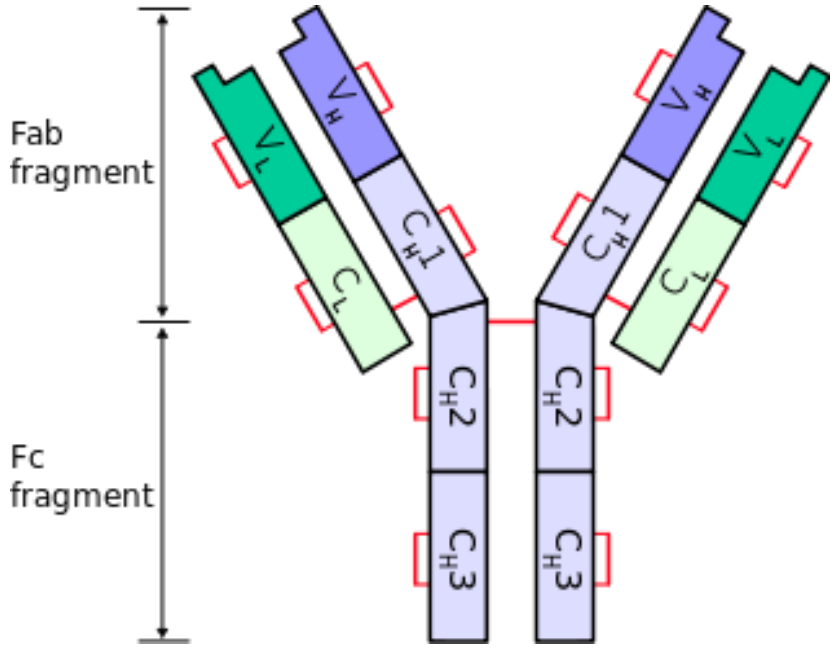

Figure 1.18: Schematic diagram of an IgG antibody molecule. It has heavy chains shown in blue linked by disulfide bonds to two light chains shown in green. The constant (C) and variable (V) domains are shown. The heavy chain contains 2 regions; the Fab (antigen-binding portion) and Fc (constant region). From https://en.wikipedia.org/wiki/immunoglobulin_light_chain

mediators within the vescles including histamines cause the characteristic symptoms of allergy [84]. FcεRI on 2H3 rat basophilic leukemia cells have been widely studied as a model system for receptor dynamics and signaling. Figure 1.19 shows a schematic of the entire IgE molecule bound to the FcεRI.

II. RESEARCH GOALS

In this study we have developed methods to use commercial QDs as probes for protein rotational diffusion measurements. Invitrogen QD655 have a size of about 5.8 x 12.8 nm and rotate in water at 0.46 μsec [85] which is much faster than unhindered small proteins on cell surfaces. Fluorescence of QDs is vertically or horizontally polarized according to their orientation. Changes in QD orientation can be detected either through polarization images comparing intensities in two detector channels or through rotation-caused polarization changes in a single detector channel. As a quantum dot diffuses rotationally from one orientation to another, its relative fluorescence intensity detected through a single polarizer will vary. Fluctuations in intensity due to rotation can be detected and analyzed by correlation methods.

Successful use of QD probes requires the development of instrumentation and procedures for examining QD655s conjugated to A_2DNP-specific IgE bound to FcεRI on RBL-2H3 cells. A suitable approach for such measurements needs to be robust, *i.e.* applicable to a wide range of problems without major changes, ideally without requirements for complex instrumentation. Such a method also needs to be capable of measuring a wide range of molecular rotation rates.

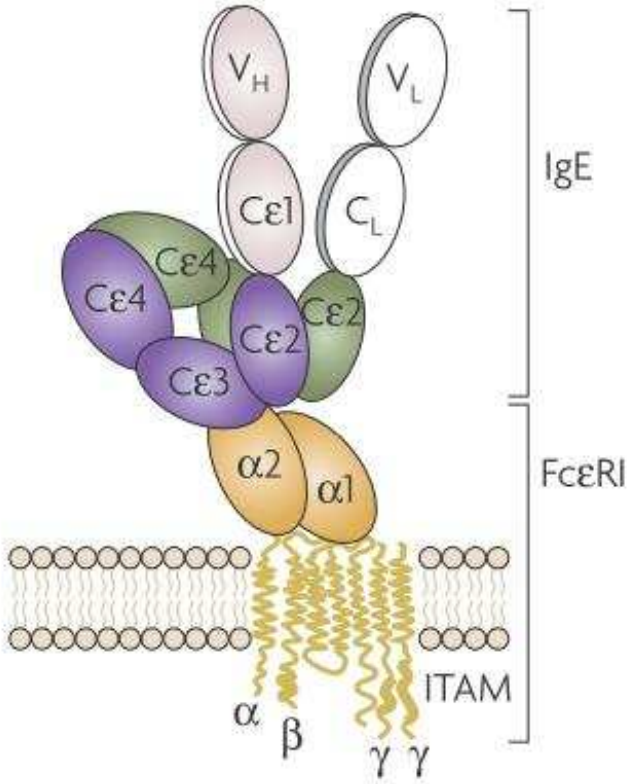

Figure 1.19: Schematic of the entire IgE molecule bound to the extracellular domains of the FcεRI, according to the structural information from the Fcε 3-4 complex and the bent IgE- FcεRI structure. From Gould and Sutton, 2008 [86].

Additionally, we wished to answer important questions concerning rotational dynamics of cell surface molecules. TPA measurements on cell have been used to study μsec timescale rotational motions. Such studies have also raised additional questions about molecular reorientation on slower timescales. TPA measurements on protein of cell membrane are limited by the lifetime of organic phosphorescent probes and thus molecules rotating more slowly than about 1 msec appears rotationally immobile. Figure 1.20 shows the rotation of erythrosin-labeled IgE-type I Fcε receptor complex on suspended 2H3 mast cells [87]. The initial FcεRI anisotropy of 0.068 decays only to 0.039 over 350 μsec, while MAFA anisotropy decays from 0.061 to 0.047. Use of QDs would permit us to identify the origin of these limiting anisotropies. All other cell surface proteins examined to date in rotation studies exhibit similar long-time anisotropy values. The developed approach could also answer another question, namely whether the molecule in question resides in a restricted lateral compartment such as a membrane microdomain or in the bulk membrane.

III. MATERIALS AND METHODS

III.A. Sources of materials

2H3-RBL cells were purchased from ATCC (Manassas, VA). Penicilin G and L-glutamine solution were purchased from Gemini Bio-Products (West Sacramento, CA). FBS was purchased from Atlas Biologicals (Fort Collins, CO). Bovine albumin, cytochalasin D, paraformaldehyde, methyl-β-cyclodextrin and ethylenediamine tetraacetic acid (EDTA) were purchased from Sigma-Aldrich (St. Louis, MO). QD655 streptavidin conjugate and DNP-BSA were purchased from Life Technologies (Eugene, OR). Rhodamine 6G was purchased from

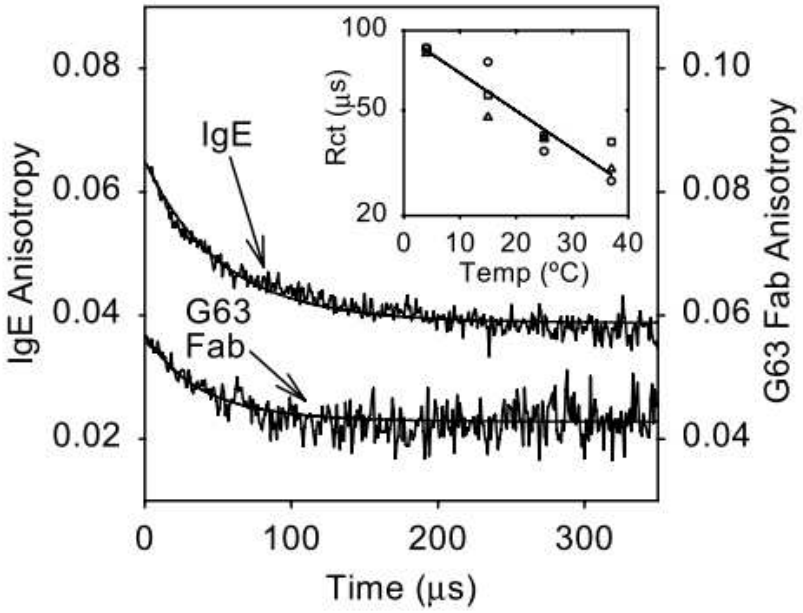

Figure 1.20: Time-resolved phosphorescence anisotropy measurements of Er-IgE-FcεRI rotation on 2H3 cells. Adapted from Song *et al.*, 2002 [88].

Eastman Kodak (Rochester, New York). Glass bottom cell culture dishes with 35mm diameter and 14mm diameter glass bottoms were purchased from In Vitro Scientific (Sunnyvale, CA). 22x22mm micro cover glass and microscope slides were purchased from VWR (Denver, CO)

III.B. Preparation of QD655 on the glass

To prepare QD655 on glass, 1µM QD655 streptavidin conjugate was diluted in ethanol to 0.005 nM. 20 µL of this solution was deposited dropwise onto a glass coverslip with a spin coater at 3000 rpm. The glass coverslips were then put on the microscope slides using tape.

III.C. Cell culture

2H3-RBL cells were maintained in 25 cm^2 culture flasks in MEM supplemented with 10% FBS, 200 mM L-glutamine, 10,000 U/mL penicillin G, 10 µg/mL streptomycin and 25µg/mL fungizone. 24-36 hours before experiments, cells were seeded onto sterile #1.5 glass-bottom culture dishes and grown to approximately 50% confluence. All cells were maintained in 5% CO_2 and a 37°C humidified environment.

III.D. QD 655 labeling of FcεRI

QD 655 was used to bind biotinylated IgE antibody which has very high affinity for FcεRI. The Invitrogen protocol was used to achieve one protein molecule conjugated per quantum do to label cells, RBL-2H3 cells were seeded onto sterile #1.5 glass bottom culture dishes to 50% confluence. Cells were washed 2x with 1mL pH 7.4 PBS/0.1%BSA (PBS/BSA) and then labelled with 1nM biotinylated IgE for 20 mins. After labelling, cells were washed 4x with PBS/BSA. One dish had no further treatment. For the other 4 dishes, cells were subjected

to one of four treatments. Table 1.1 shows concentrations and labelling times for various 2H3 cell treatments. After being treated, cells were washed 4x with PBS/BSA and cells in each of the five dishes were incubated with QD 655-streptavidin at 100 pM for 10 mins and washed 6x before imaging. There were 10-20 quantum dots bound per cell. Every step was done in pH 7.4 PBS/BSA solution. All cell labeling were conducted at room temperature.

III.E. Imaging rotation measurements

III.E.1. Image collection

Untreated and treated cells were maintained in pH 7.4 PBS/BSA solution. Images from cells were collected by fluorescence microscopy using a Zeiss Axiovert 200M microscope with a 100x oil objective and custom QD 655 filter set including excitation filter 460/50, dichroic beam splitter 475 and emission filter 655/40. Fluorescence from cell-bound quantum dots was excited by illumination from a 100W arc lamp. A Princeton Instruments Dual View image splitter equipped with polarizing beamsplitter allowed recording of image sequences containing simultaneous x- and y-polarized sub-images in each frame. Orthogonally polarized images were collected every 10ms for up to 1000 frames at a final magnification of 500x using an Andor Ixon EMCCD camera. For dry QDs 655 on the glass, image sequences were obtained by repeating the same steps as collection of cell image sequences. Figure 1.21 shows a diagram of image data acquisition. An example of QD 655 conjugated to IgE antibody bound to FcεRI on 2H3 mast cells is shown in Figure 1.22.

Table 1.1: Concentrations and labelling times for various 2H3 cell treatments.

Treatment	Concentration	Labeling/treatment time
DNP-BSA	0.01%	1 h
paraformaldehyde	4%	45 min
MβCD	0.01%	1 h
Cytochalasin D	40μM	1 h

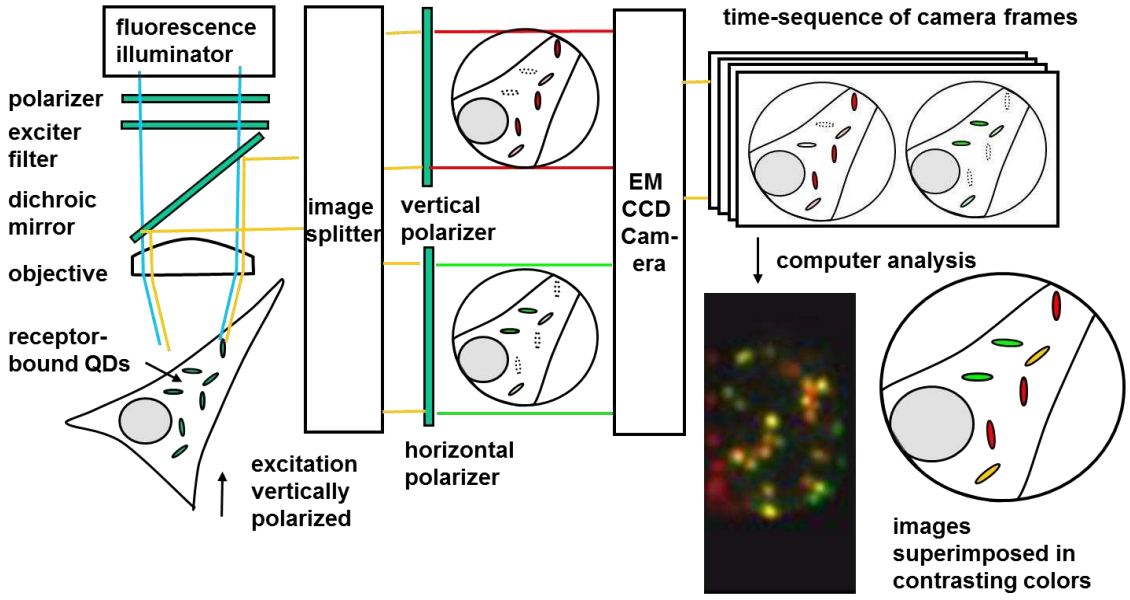

Figure 1.21: Diagram of image data acquisition for rotation measurements. Fluorescence from cell-bound quantum dots was excited by arc illumination. A Princeton Instruments Dual View equipped with a polarizing beam splitter allowed recording image sequences containing simultaneous x- and y-polarized sub-images in each frame. Orthogonally polarized images were collected every 10msec for up to 1000 frames at a final magnification of 500x onto an Andor Ixon EMCCD camera.

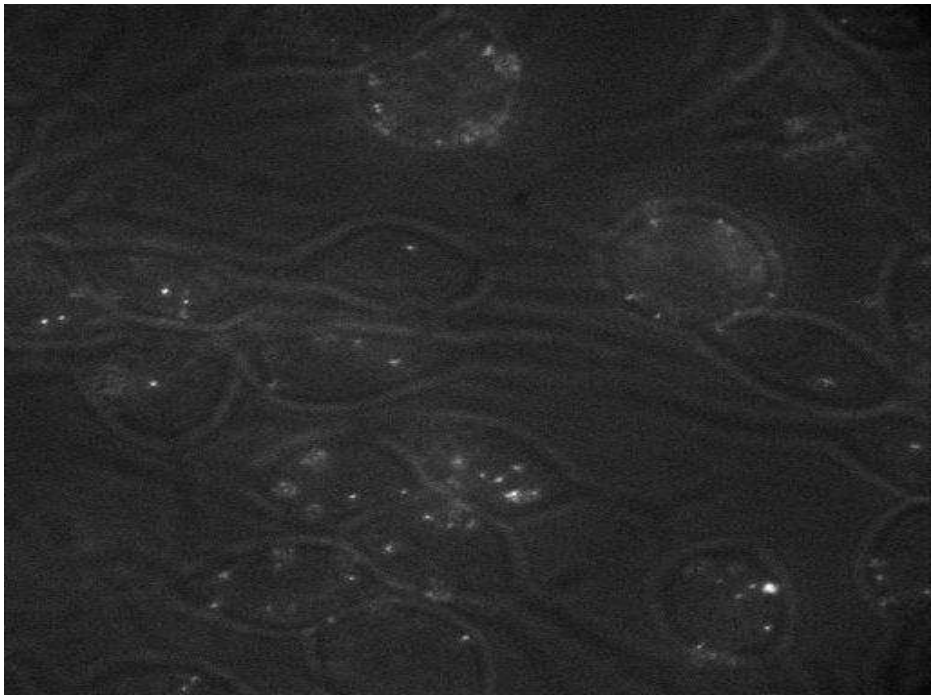

Figure 1.22: Quantum dots 655 conjugated to biotinylated IgE antibody and bound to RBL-2H3 cell FcεRI.

III.E.2. Data analysis procedures

Image stacks collected as above were analyzed using NIH Image J. Sub-pixel alignment of the vertically- and horizontally-polarized sub-images is necessary for rotational correlation calculations but cannot be achieved mechanically, even with careful alignment of the Dual-View before the start of every experiment. Hence the following procedure was used. Image stacks of QD 655 on a cell or surface were segmented into separate stacks containing vertically and horizontally-polarized images. Each stack was flattened, i.e. averaged, and the horizontally-polarized average image adjusted with respect to the vertically polarized one to correct for displacement, rotation and dilation of one image relative to the other. The parameters of this adjustment were then used to correct the entire horizontally-polarized stack to achieve sub-pixel alignment with the vertically-polarized one. This alignment was visualized by superimposing the horizontal polarized image (red) atop the vertically polarized image (green). Figure 1.23 and Figure 1.24 show examples of QD 655 quantum dots on an RBL-2H3 cell surface and on glass, respectively.

Regions of interest (ROI) around individual QD in different images were defined using Image J after realignments were finished. Typically 10-20 QD were examined per cell. Background ROIs well away from any QD were also selected, typically four background areas were chosen for each cell. All ROI were created at exactly the same size. Figure 1.25 shows image examples of the defined QD regions and the defined background regions.

For each image sequence, the average intensities in each dot's ROI and in each background ROI were measured in Image J and exported as a CSV file. The result file includes average intensities in the ROI around each QD in the horizontally- and vertically-polarized

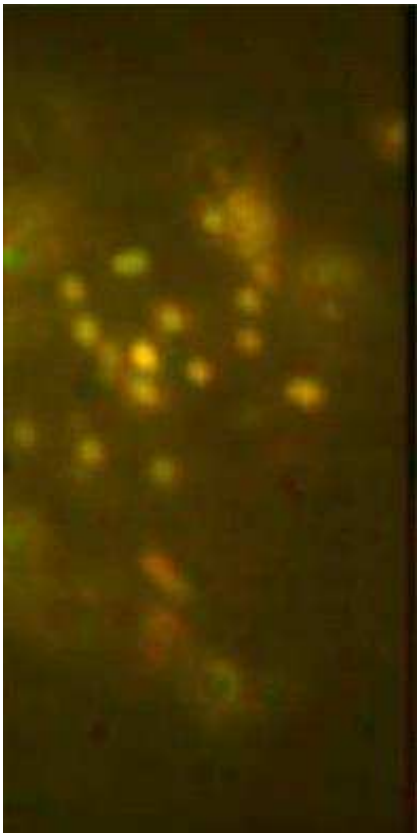

Figure 1.23: RGB images of QD 655 conjugated to biotinylated IgE antibody and bound to RBL-2H3 cell FcεRI. Horizontally polarized fluorescence (red) and vertically polarized fluorescence (green) images are superimposed.

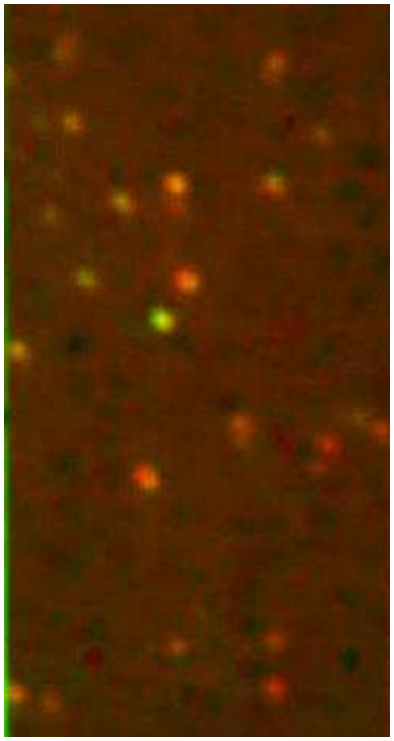

Figure 1.24: RGB images of QD 655 on glass. The orientation of individual QD 655s on glass is readily observable from pseudo-colored overlays of horizontally- and vertically- polarized images.

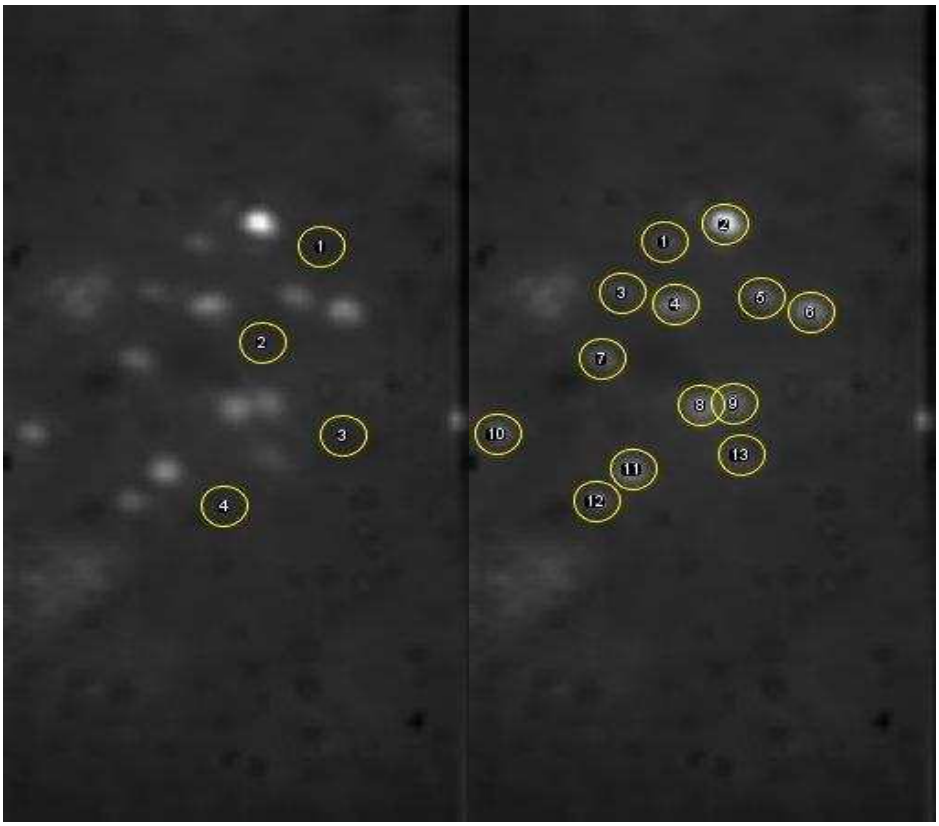

Figure 1.25: Regions-of-interest on cell images. Left panel: Defined background regions. Right panel: Defined QD regions.

images plus the background intensities averaged over the four background ROI. Table 1.2 shows an example of QD and background intensities in an exported CSV file.

Complete removal of quantum dot blinking effects is the critical step in data analysis. Polarization is defined as (v-h)/(v+h) where v and h are true intensities of the two fluorescence signals. However, correction of observed fluorescence v_{obs} and h_{obs} to obtain true values involves experimental parameters such as the "g-factor", camera background and local cell background which can change between QDs, even in the same image. Therefore depending on instrumental parameters used in data analysis, calculated polarization values can contain a contribution from the intensity function (v+h) which varies with QD blinking. When, in turn, polarization fluctuations are correlated to obtain the polarization time autocorrelation function (TACF) intended to quantitate molecular rotation, errors in these parameters can introduce into polarization fluctuation TACF a contribution from the intensity fluctuation TACF arising from QD blinking.

Thus, to confidently remove effects of quantum dot blinking on the polarization fluctuation time autocorrelation function, optimum values for instrumental parameters must be selected based on the necessary statistical independence of the polarization and intensity function. Other factors, such as non-negativity of corrected intensities are additional necessary constraints applied within this non-linear optimization which was performed in Mathematica. When complete, this data analysis software will be available through the CSU Digital Repository upon request. For some QD, less than 20 % of the total, optimizations of instrumental parameters failed, typically by failure to converge at all or by converging to physically impossible values such as negative g-factors. Such QD were not examined further.

Table 1.2: An example of a CSV file created from one image sequence. Only a portion of the file is shown here. The "L-avg" and "R-avg" columns are the average of the background intensities in four background ROI. "L001" and "R001" are the average intensities in the left (vertically-polarized) and right (horizontally-polarized) for QD 1.

Frame	L-avg	R-avg	Frame	L001	R001	Frame	L002	R002
1	356.7343	335.5625	1	409.753	356.378	1	401.391	357.409
2	358.6898	335.5993	2	416.497	359.865	2	392.622	348.035
3	358.2905	335.5118	3	411.548	356.513	3	397.763	353.096
4	356.451	335.9393	4	408.84	355.2	4	377.241	343.464
5	357.7245	334.6485	5	418.082	355.746	5	378.446	347.172
6	356.1408	336.4105	6	420.53	359.127	6	400.611	355.607
7	356.3973	334.7348	7	408.726	356.622	7	390.135	352.391
8	357.1488	336.1268	8	420.043	357.053	8	399.611	356.636
9	358.5978	335.5743	9	422.472	358.17	9	392.528	355.769
10	356.367	336.8833	10	417.46	360.419	10	411.47	366.589
11	355.8733	335.926	11	416.063	359.546	11	400.73	355.387
12	357.519	335.7815	12	406.881	351.922	12	400.849	356.973
13	358.0573	335.9693	13	396.697	347.922	13	400.043	356.249
14	357.9903	335.6135	14	414.916	356.497	14	384.413	350.415
15	356.8933	335.0915	15	403.421	353.98	15	395.566	354.221
16	357.022	335.0955	16	413.65	355.258	16	398.892	354.505
17	357.5503	335.9283	17	400.493	354.669	17	412.11	359.266
18	357.8585	335.1365	18	401.665	353.403	18	420.526	366.859
19	358.042	335.2808	19	407.112	357.616	19	394.881	353.309
20	357.1708	335.8855	20	420.898	359.378	20	401.56	355.812
21	357.0555	335.056	21	399.755	352.585	21	401.538	359.472
22	356.4658	335.3885	22	400.403	349.834	22	374.129	343.965
23	356.8415	336.1965	23	413.892	354.245	23	393.454	353.701
24	357.9698	335.4015	24	402.292	350.963	24	383.791	348.845
25	356.598	336.2615	25	375.996	341.726	25	396.595	354
26	357.474	335.0905	26	407.059	352.728	26	403.875	357.018
27	358.0798	334.9255	27	416.031	358.479	27	393.503	352.605
28	356.9903	336.1818	28	409.822	352.552	28	391.963	355.767
29	357.379	336.2328	29	415.276	356.209	29	396.871	357.08
30	357.1703	336.2448	30	410.497	356.685	30	372.581	343.254
31	357.8195	336.4578	31	407.781	351.982	31	388.902	351.151
32	358.2518	336.0768	32	417.434	356.389	32	380.391	345.603
33	357.7495	336.4955	33	420.847	357.272	33	369.91	341.816
34	358.106	335.663	34	416.969	358.55	34	375.487	342.227
35	357.9558	336.4975	35	420.892	359.393	35	367.585	339.566
36	357.9408	335.3178	36	430.1	359.196	36	357.063	336.389

Once corrected intensities were obtained for a given QD, polarization p was calculated for each frame. The time-autocorrelation functions $g_p(\tau)$ and $g_s(\tau)$ for polarization and intensity fluctuations, respectively, about the appropriate long–time means are given by

$$g_p(\tau) = \frac{1}{T}\sum_{t=0}^{T-\tau-1}\left[p(t)-\overline{p_t}\right]\left[p(t+\tau)-\overline{p_{t+\tau}}\right] \tag{1.6}$$

$$g_s(\tau) = \frac{1}{T}\sum_{t=0}^{T-\tau-1}\left[s(t)-\overline{s_t}\right]\left[s(t+\tau)-\overline{s_{t+\tau}}\right] \tag{1.7}$$

Where τ is correlation time in frames and T is the total number of frames recorded. For each dot analyzed, the various numeric parameters obtained were saved automatically in a CSV file and graphs were saved in a PDF file.

III.F. Rotation measurements using time-tagged single photon counting

III.F.1 Experimental apparatus

The time-tagged single photon counting system is based on Olympus IX-71 microscope equipped with B&H DPC-230 photon correlator card and an ALV-7004 digital hardware correlator. A 100x 1.4NA oil objective was used for all QD experiments. A ModuLaser StellarPro multiline argon ion laser operating at 488 nm was coupled into a Point Source KineFLEXTM–P-3-S-488-640-0.7-FCP-P2 fiber and the fiber output recollimated by a 4.6 mm FL collimating lens. In actual QD experiments a 0.5x Galilean telescope reduced the beam diameter 2-fold to increase the size of the illuminated spot on the sample. An Olympus dual lamp adapter allowed side access to the fluorescence illumination path and a 40 cm plano-convex lens positioned on the side of the adapter projected the microscope image plane to infinity while re-creating the objective back focal plane a convenient distance to the side of the microscope. A 2.5OD neutral density filter was typically applied to the above lens mount to reduce laser

intensity. The unique part of this system is the use and location of a gimbal mount for the laser collimator and optional beam-expanding telescope. The gimbal axis was positioned at the re-created back focal plane of the microscope objective and the collimating lens, or the output lens of the telescope if used, was positioned at this point. Tilting the gimbal axes moved the focused laser spot in the sample plane while insuring that the beam remained centered on the objective back aperture. The microscope objective collected fluorescence from a QD in the focal volume of the laser beam. A unique 4-channel photon counting detector capable of acquiring 4 fluorescence signals selected independently by fluorescence polarization and/or wavelength was used (Figure 1.26). In the detection path, a 300μm pinhole located in an image plane ahead of the detector was used to reject out-of-focus light. Two orthogonal polarization components were separated by a polarizing beamsplitter. Each signal could be sub-divided by a non-polarizing beamsplitter. This allows cross-correlation and pseudo-autocorrelation calculations for each polarization. Figure 1.27 illustrates data acquired by this apparatus.

III.F.2. Determination of laser spot size

Two methods were used to determine the spot size of the focused laser beam. One method measured the laser beam diameter by imaging the beam and calculated the focused spot size. The other method measured the diffusion time of rhodamine 6G dye in solution using fluorescence correlation spectroscopy (FCS).

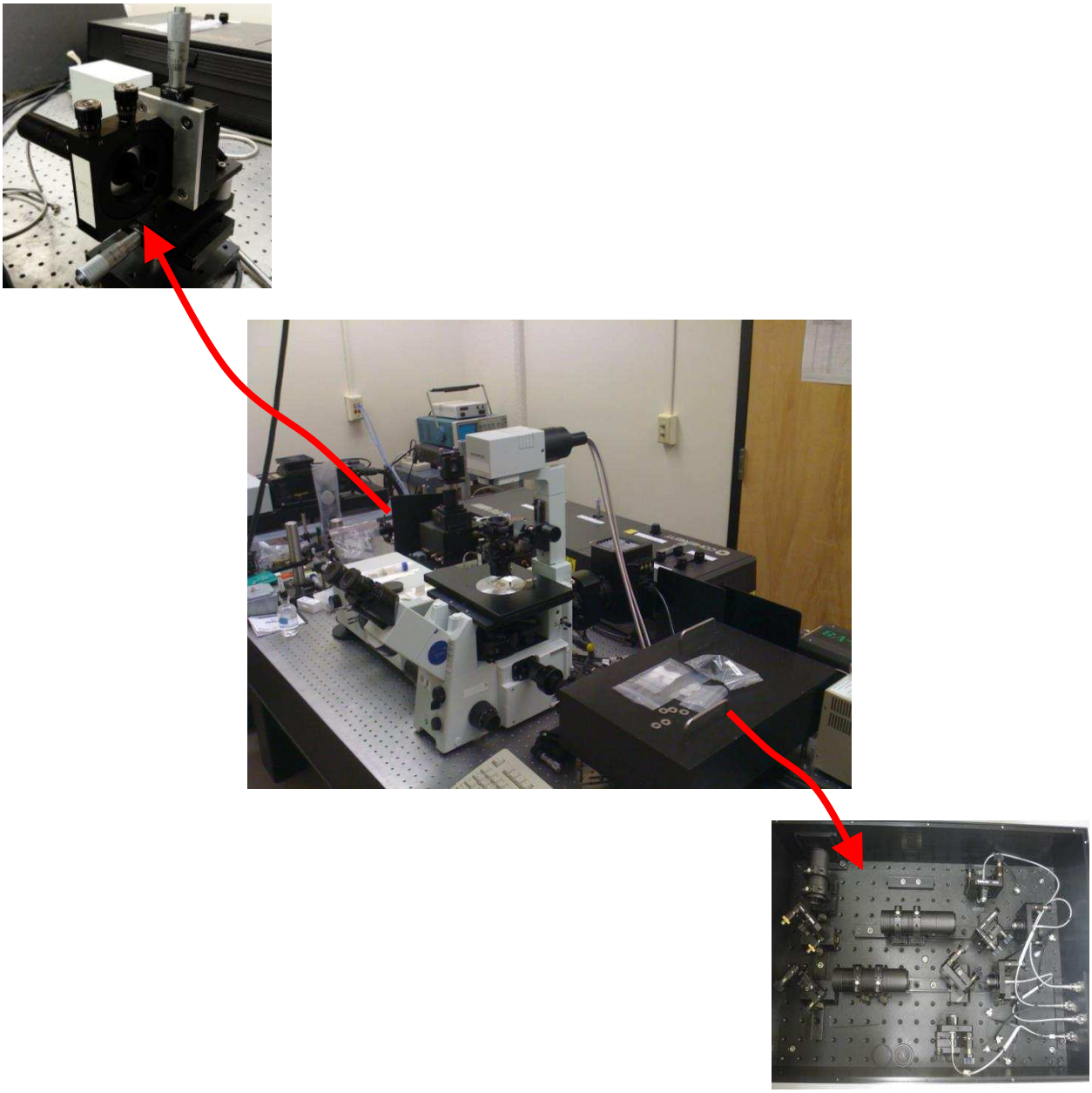

Figure 1.26: Time-correlated photon counting system. The upper-left photograph shows the gimbal-mounted laser with its output lens situated in recreated a back focal plane of the microscope objective.

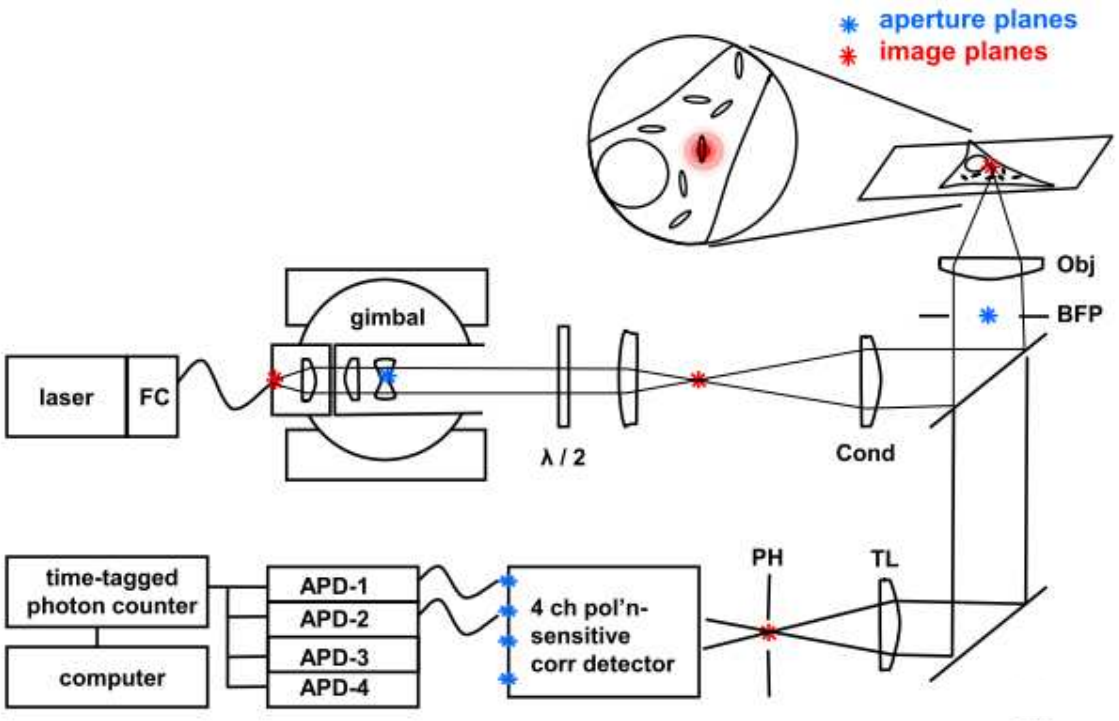

Figure 1.27: Diagram of data acquisition by time-tagged single photon counting. The polarized illumination was carried out using a 488nm laser beam sent through a gimbal-mounted collimator and telescope and an objective toward the sample. The objective was used to collect fluorescence from the QD in the focal volume of the laser beam. A pinhole was used to reject the out-of-focus light. In the detection path the two orthogonal polarization components were split by a polarization beamsplitter. Each signal was sub-divided to two detectors which detected by photodiodes working as polarization channels with intensity I_v and I_h.

III.F.2.a. Imaging measurement of laser beam diameter

Translucent tape was fixed to a microscope slide and three parallel thin pencil lines were made on the tape. An objective was the removed from the microscope turret and the taped portion of the slide set atop the hole. With laser light entering the microscope, the slide was aligned so that the beam fell between a pair of pencil lines. The laser beam illuminating the translucent tape was then photographed as shown in Figure 1.28a. Counting the pixels between two adjacent lines via Image J and measuring the distance between the lines with a ruler provided the number of millimeter per pixel. The image was imported into SigmaPlot as a TIF file and fitted to a two-dimensional Gaussian function, as shown in the 3D plot in Figure 1.28b. The fitted beam radius R in pixels was converted to the actual beam radius in mm and the focused spot size r calculated as $\lambda f/(\pi R)$ where λ is the laser wavelength and f is the focal length of the objective.

III.F.2.b. FCS determination of focused spot size

Fluorescence correlation spectroscopy (FCS) extracts information on dynamics of physical processes from spontaneous fluctuations in fluorescence intensity over time. The method is based on examination of a small number of molecules, for example within the femtoliter volume of solution illuminated by a focused laser beam. Fluctuations in the number of molecules in the volume and hence in the fluorescence measured are analyzed by applying time auto- or cross-correlation analysis to the fluorescence intensity. FCS data for rhodamine 6G (R6G) diffusion were analyzed using methods similar to those previously described by Schwille *et al.* [89].

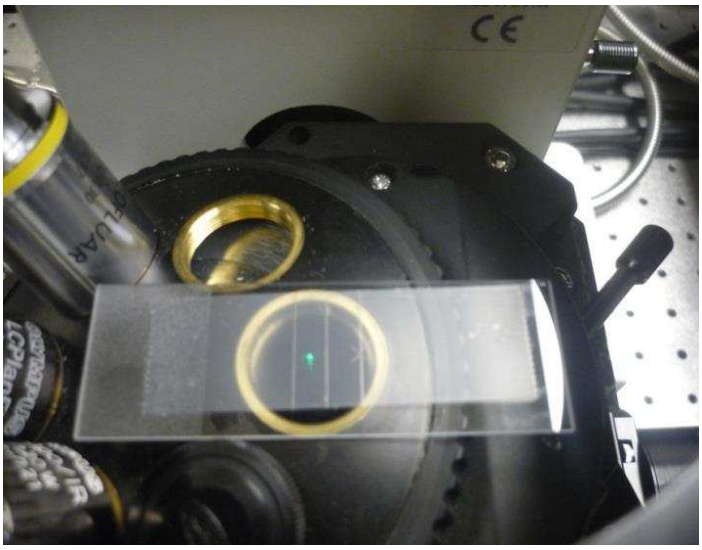

(a)

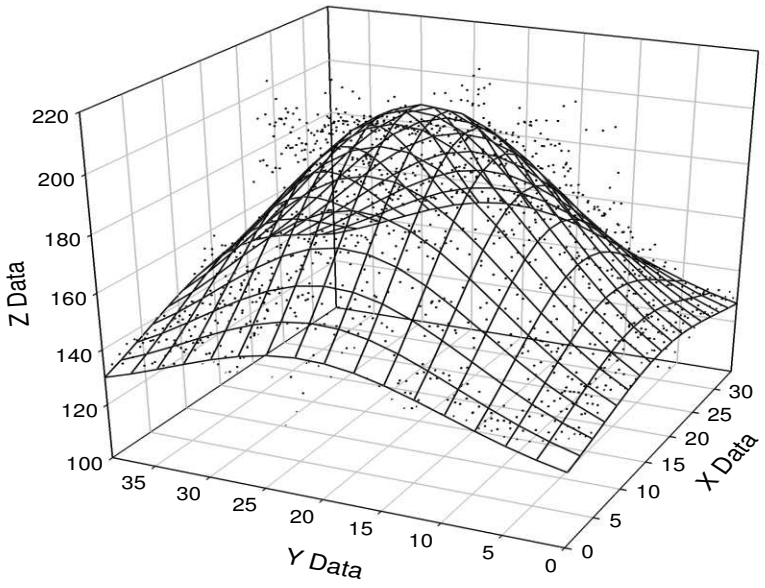

(b)

Figure 1.28: (a). 514 nm laser beam illuminating translucent target in the approximate back focal plane of a microscope objective (b). 3D plot of laser beam profile. The grid represents the best-fitting 2D Gaussian with a $1/e^2$ radius of 0.859 mm.

If F(t) is the fluorescence intensity fluctuation at time t, the fluctuations δF(t) about the mean <F(t)> are $\delta F(t) \equiv \mathrm{F}(t)\text{-}\langle F(t)\rangle$ and the normalized fluctuation time autocorrelation function g(τ) is then calculated as

$$g(\tau) = \langle \delta F(t) \delta F(t+\tau) \rangle / \langle F(t) \rangle^2 \tag{1.8}$$

For lateral diffusion within a Gaussian spot of radius r_0, the autocorrelation function g(τ) describing this diffusion is given by

$$g(\tau) = \frac{1}{N_{eff}} \left(\frac{1}{1 + \tau / \tau_d} \right) \tag{1.9}$$

where the diffusion correlation time τ_d is $r_0^2/(4D)$.

Figure 1.29 shows an example of R6G autocorrelation trace. FCS data were fitted to equation 1.8 using SigmaPlot to determine the focused laser spot size. Both methods, calculation from laser beam diameter at the objective and measured from R6G diffusion yielded a focused spot radius r_0 of 291 nm without the beam reducing telescope. In actual QD experiments, a larger illuminated spot was required to insure that QD random lateral motion did not take the particle outside the illuminated region during the duration of the experiment.

III.F.3. Photon counting data collection

Treated and non-treated cells were maintained in 0.1% BSA pH 7.4 in a culture dish and ready for photon counting experiments. Before measurements a dye slide was used to insure that the laser spot was located in the cross mark of the illumination area center. To make a measurement, the arc lamp was turned on to identify a single QD. The slide or Petri dish was moved to put the dot on the cross area where the laser spot was located. The single dot was also visible from the monitor connected to the microscope. The objective was used to collect

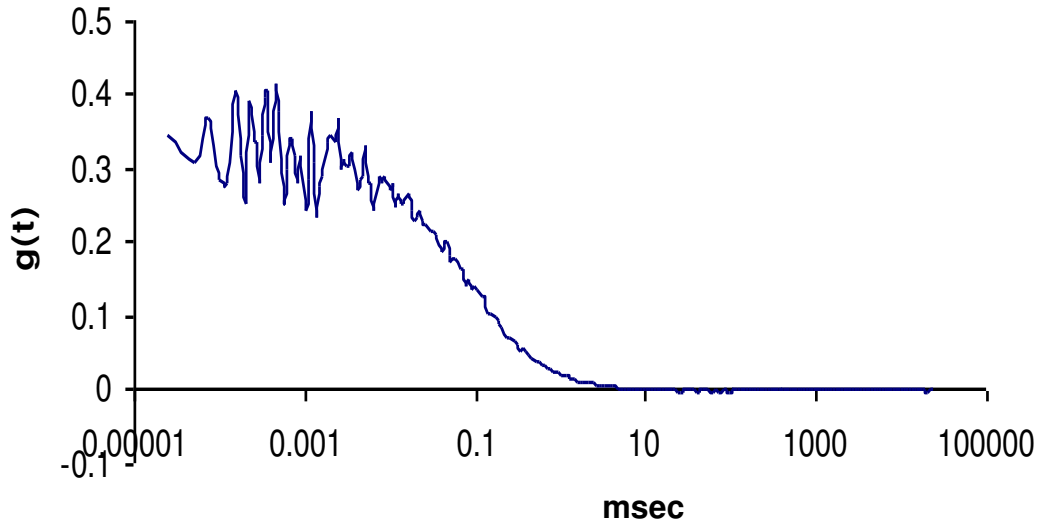

Figure 1.29: Time auto-correlation function for 200 nM R6G fluorescence fluctuations.

fluorescence from the QD in the laser spot. A 300 µm pinhole in front of the polarizing beam splitter was used to reject the out-of-focus light and adjusted to obtain the maximum signal. Horizontal polarized and vertical polarized signals were sent to two detectors detected by photodiodes individually. Figure 1.30 shows an example of a photon counting trace for a single QD 655 on a 2H3 cell.

IV. RESULTS AND DISCUSSION

IV.A. Imaging rotation measurements

IV.A.1. Initial data analysis

Image stacks of cell-bound QD produced by the Dual View image splitter appear as shown in Figure 1.25 but without the overlaid regions-of-interest indicators. The 102x102 pixel image stack is divided into left and right stacks, each of which is flattened into a single image. These images are expanded 5-fold to 255x510 pixels and the cell-containing image area of the left (vertically polarized) image aligned atop the right (horizontally polarized) image as described previously. Given the image expansion, the alignment parameters are accurate to ± 1/5 of a pixel with respect to the original image. These parameters are used to create a new right image stack now in sub-pixel registration with the left.

Regions of interest were then drawn around individual QD and around 4 QD-free background regions in the vertically-polarized image. Because of precise alignment just achieved, these regions apply equally well to the horizontally-polarized image. Intensity in each region was averaged in each region of both stacks, including the QD-free background regions.

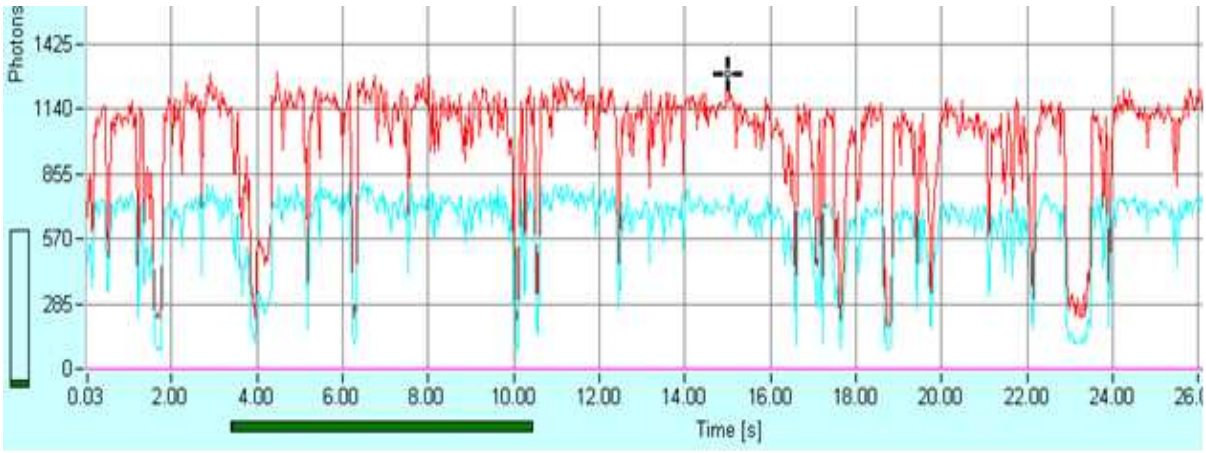

Figure 1.30: Photon counts per 30 msec interval vs. time for single QD 655 on a RBL-2H3 cell.

Figure 1.31 shows a typical example of intensity trace of individual dot. The dot displays intermittent blinking and alternating between an emitting state (on) and a non-emitting state (off).

The actual fluorescence intensity emitted with each polarization by a given QD would be expected to be average intensity in its region minus the average cell background fluorescence in a comparably sized region. However, because of slightly uneven illumination of the image area, the g-factor varies slightly across the image. Moreover, the non-specific cell background fluorescence varies across the cell surface. Hence, true intensities for each polarization must be calculated from raw data using three constants – g-factor, camera background and cell background – which vary across the image. This is a critical problem since, if constants differ even slightly from those physically causing the observed image, polarizations $(I_v-I_h)/(I_v+I_h)$ calculated from corrected dot intensities will contain some of the intensity function I_v+I_h. Since the true polarization is a ratio of the sum and difference of true intensities, the true polarization must be completely independent of fluorescence intensity. If this occurs, then the time autocorrelation function of the polarization will contain an amount of the intensity time autocorrelation function in which QD blinking appears. Hence, QD blinking could be mistaken for QD rotation.

To minimize this possibility, a Mathematica program was devised to minimize the cross-correlation coefficient of polarization p. Initial values for adjustable coefficients were those implied by the averaged background traces and changes from those values were held to a minimum. This optimization, together with the sub-pixel image alignment, was felt to guarantee that calculated polarization fluctuation TACFs actually represent QD rotational motion.

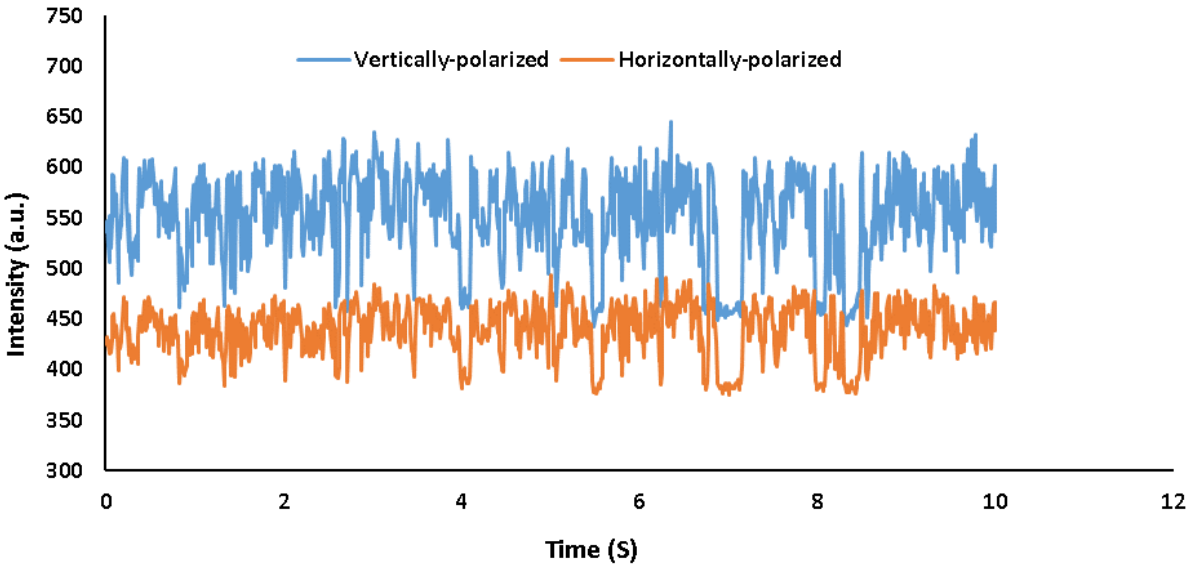

Figure 1.31: A typical example of an intensity trace for an individual cell-bound QD.

IV.A.2. Relative immobility of dry QD

This was tested by extensive studies of dry QD on glass slides. Figure 1.32 and Figure 1.33 shows the averaged polarization and intensity fluctuation TACF for 56 dry QD while Figures 34 and 35 shows similar data for 205 QD attached to 2H3 cell-bound biotin IgE. It is clear that the initial polarization fluctuation TACF is much smaller for dry dots than for cell-bound ones. Moreover, the intensity fluctuation TACF for cell-bound dots has substantially different kinetics from the polarization fluctuation TACF. The shapes of these curves were very similar before running the optimization program in Mathematica (results not shown). For these reasons, we believe that our polarization fluctuation TAC values represent real mechanical motion of receptor-bound QD.

Figures 1.36-1.41 show polarization fluctuation TACFs for dry dots and for differently-treated cells. Figure 1.42 shows the average polarization fluctuation for dry QDs on glass, IgE on untreated cells and on cell subjected to four different treatments. In these traces, the first point, showing correlation time τ of zero is omitted because this point contains a large contribution for the square of shot noise. The results (Figure 1.42) show that dry QD on glass move only 25% or less compared to QDs on IgE and also move less than QDs on cells exposed to other treatments.

Figure 1.43 compares difference of fitted polarization fluctuation TACFs between correlation time $\tau=0$ and $\tau=\infty$ for dots on glass and on untreated and treated cells. This difference for IgE on untreated and treated cells is much larger than for QD on glass, again suggesting true movement for cell-bound QD. In summary, these various results indicate that the dry dots show little, if any, motion and that effects of QD blinking on the polarization fluctuation TACF traces has been successfully eliminated.

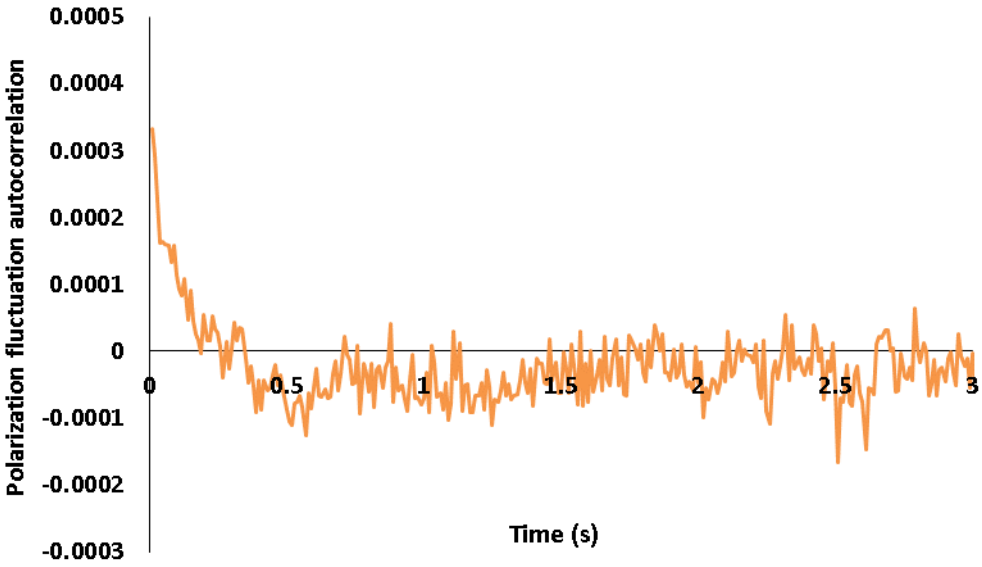

Figure 1.32: The average of fluorescence polarization fluctuation time-autocorrelation function for 56 dry QD655 dots on glass.

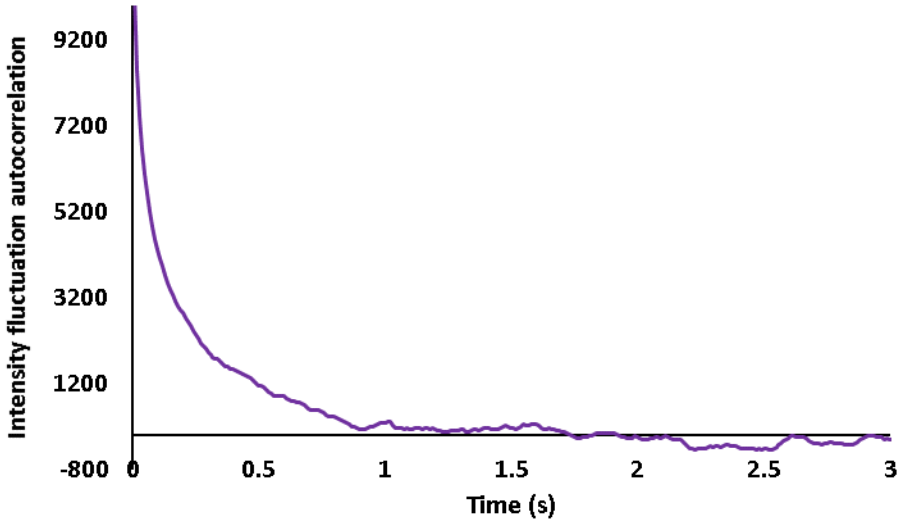

Figure 1.33: The average of fluorescence intensity fluctuation time-autocorrelation function for 56 dry QD655 dots on glass.

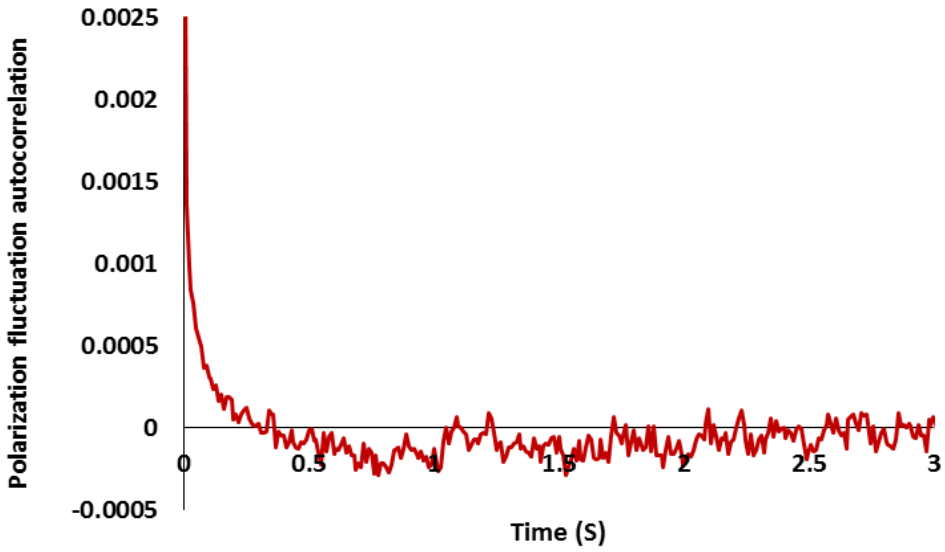

Figure 1.34: The average of fluorescence polarization fluctuation time-autocorrelation function for 205 FcεRI-bound QD655 on untreated cells.

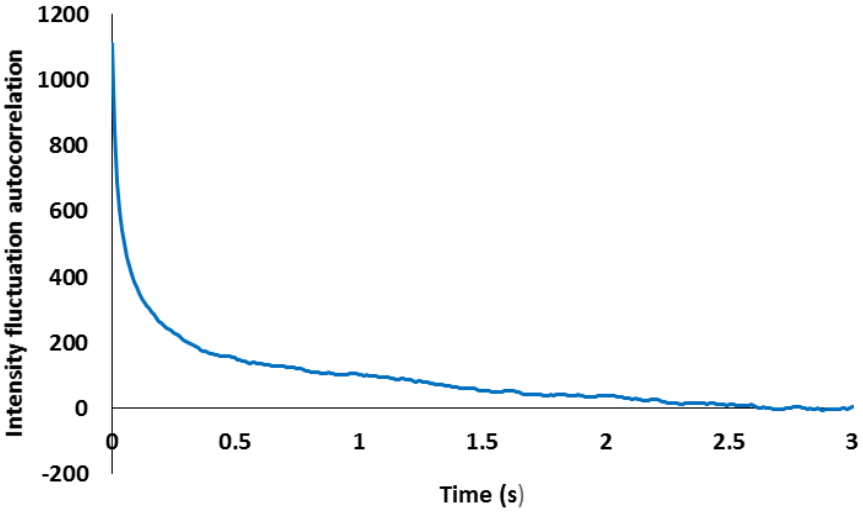

Figure 1.35: The average of fluorescence intensity fluctuation time-autocorrelation function for 205 FcεRI-bound QD655 on untreated cells.

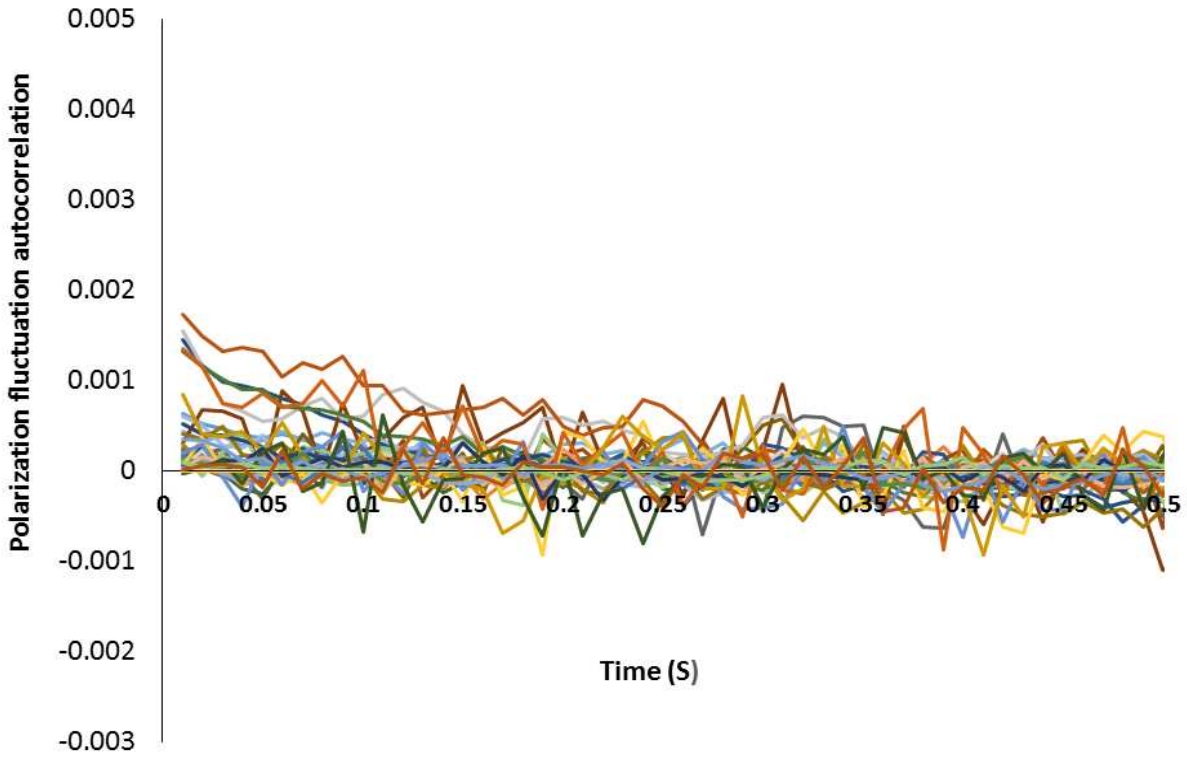

Figure 1.36: Fluorescence polarization fluctuation time-autocorrelation functions for 56 dry QD655 on glass.

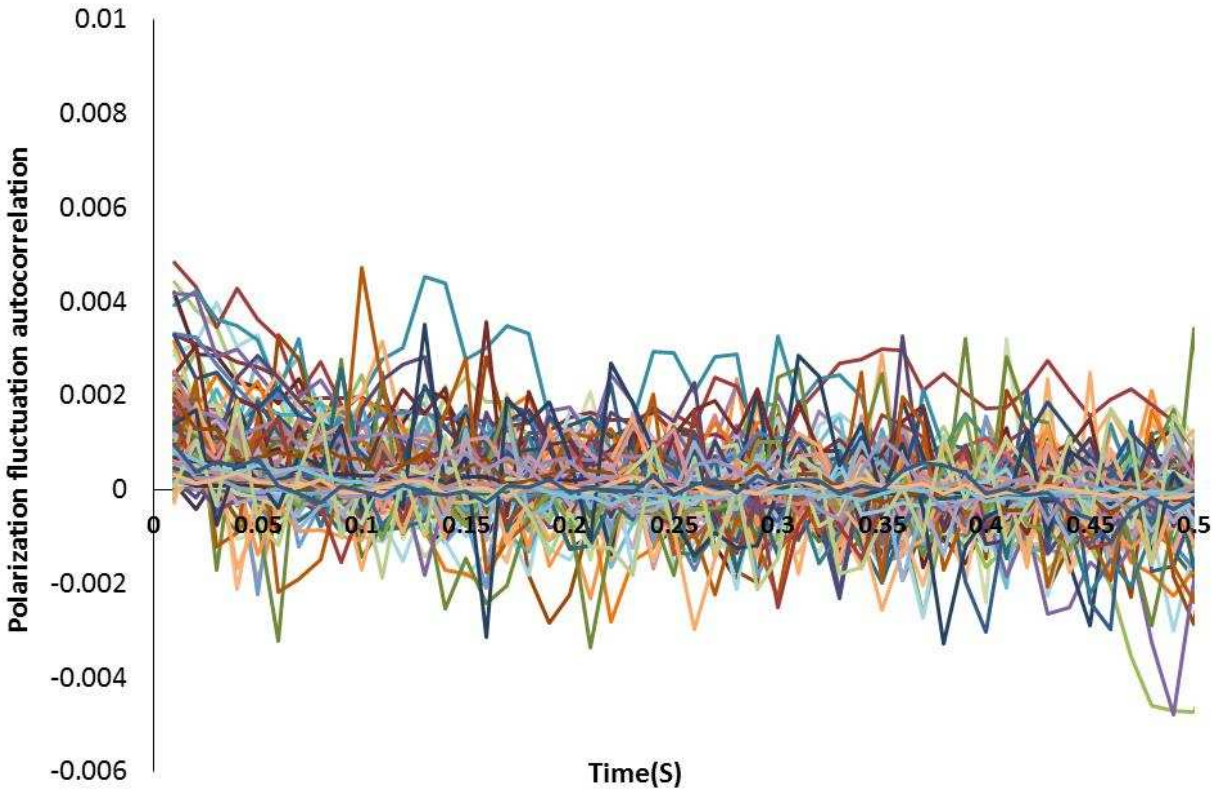

Figure 1.37: Fluorescence polarization fluctuation time-autocorrelation functions for 205 FcεRI bound QD655 on untreated cells.

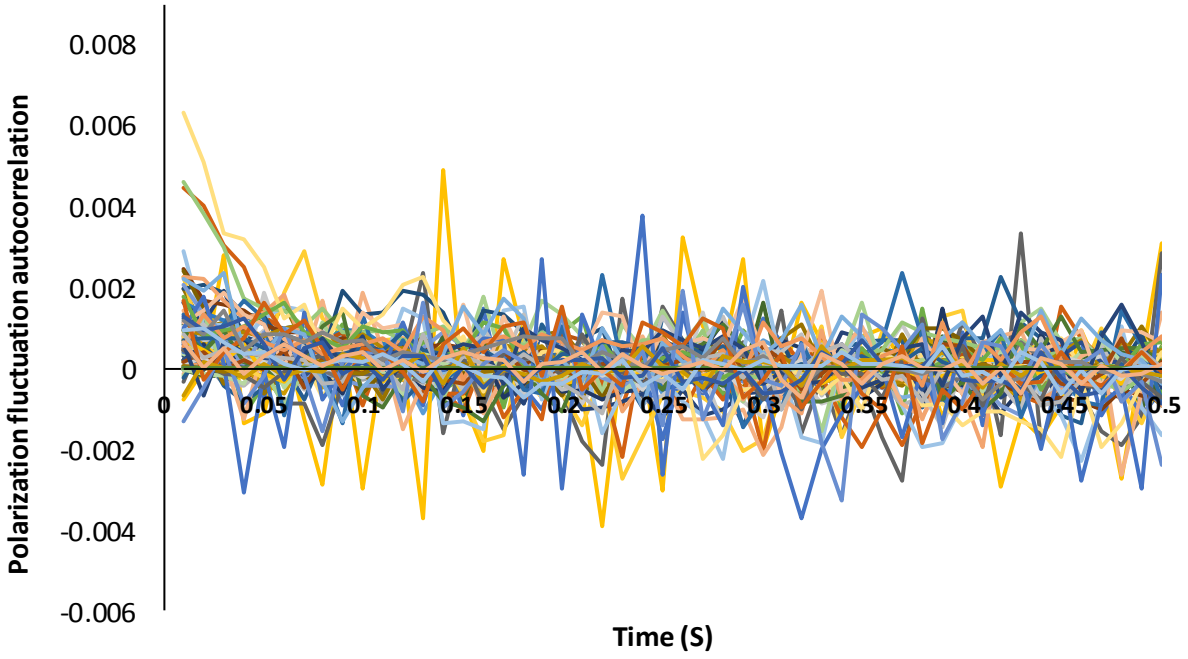

Figure 1.38. Fluorescence polarization fluctuation time-autocorrelation functions for 92 FcεRI-bound QD655 on DNP-BSA-treated cells.

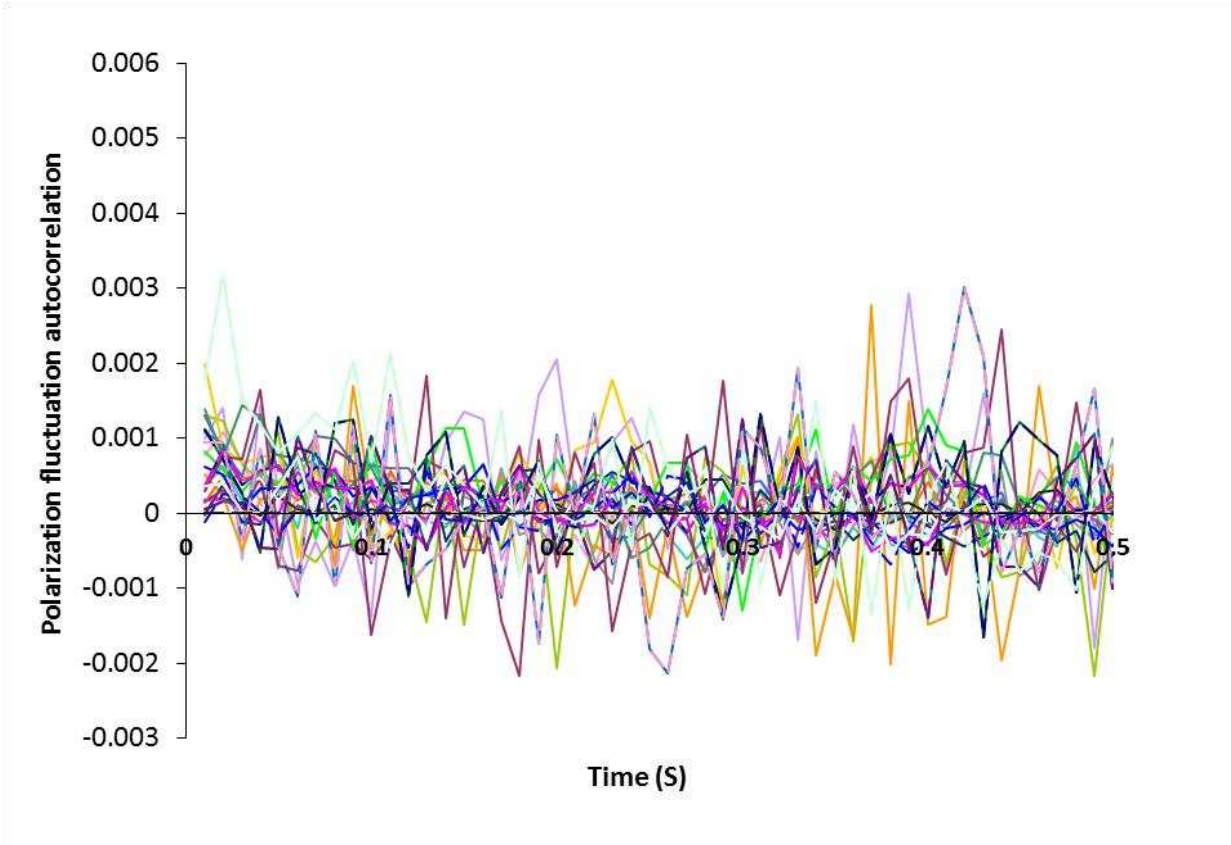

Figure 1.39: Fluorescence polarization fluctuation time-autocorrelation functions for 54 FcεRI-bound QD655 on paraformaldehyde-treated cells.

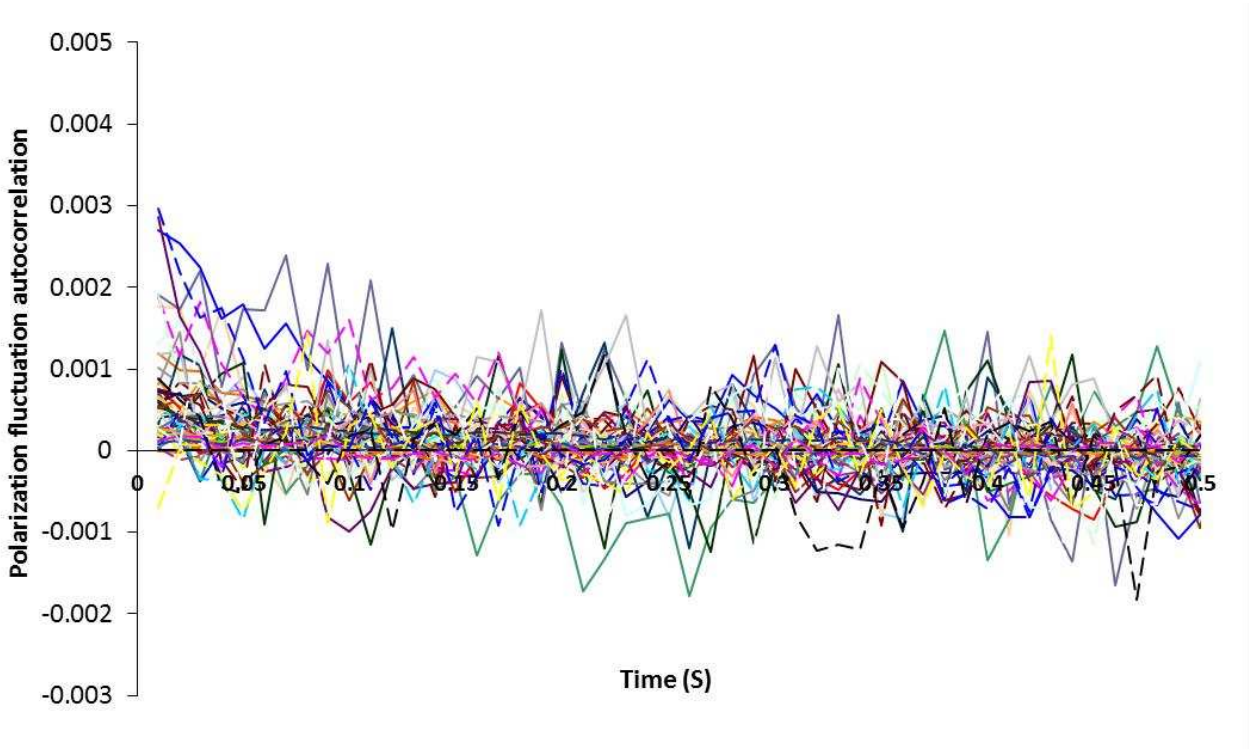

Figure 1.40: Fluorescence polarization fluctuation time-autocorrelation functions for 62 FcεRI-bound QD655 on MβCD-treated cells.

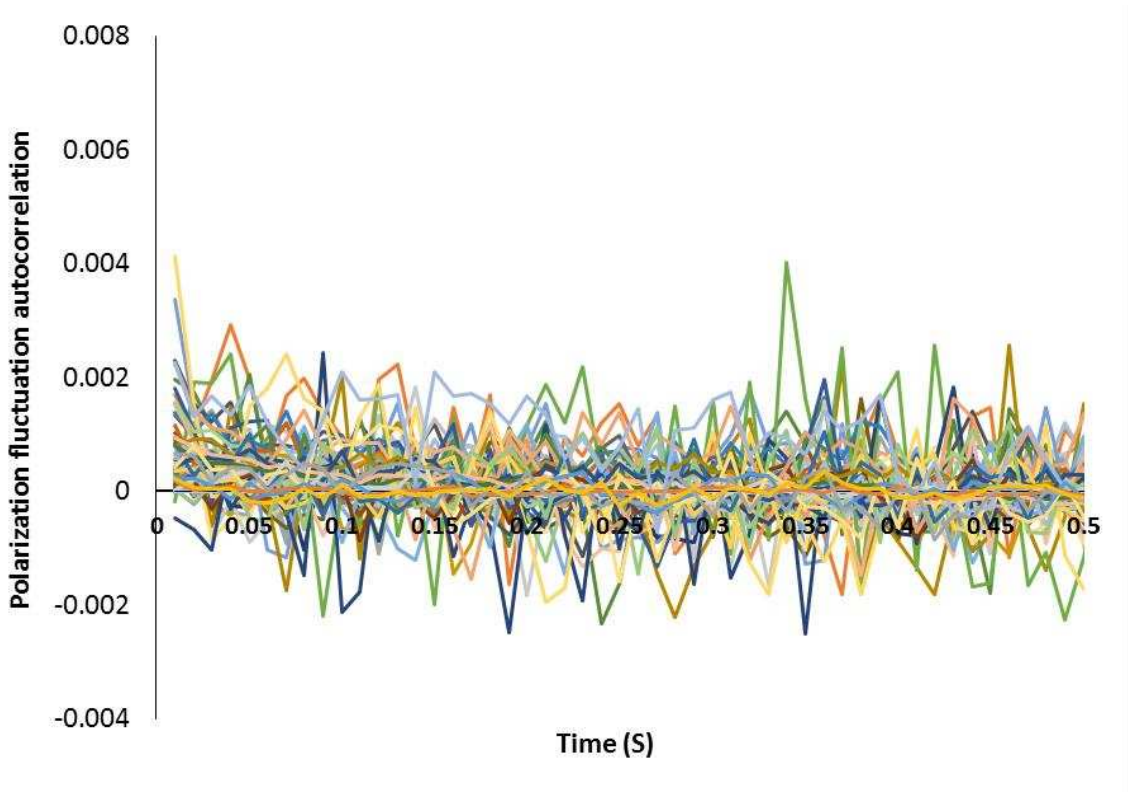

Figure 1.41: Fluorescence polarization fluctuation time-autocorrelation functions for 65 FcεRI-bound QD655 on cytochalasin D-treated cells.

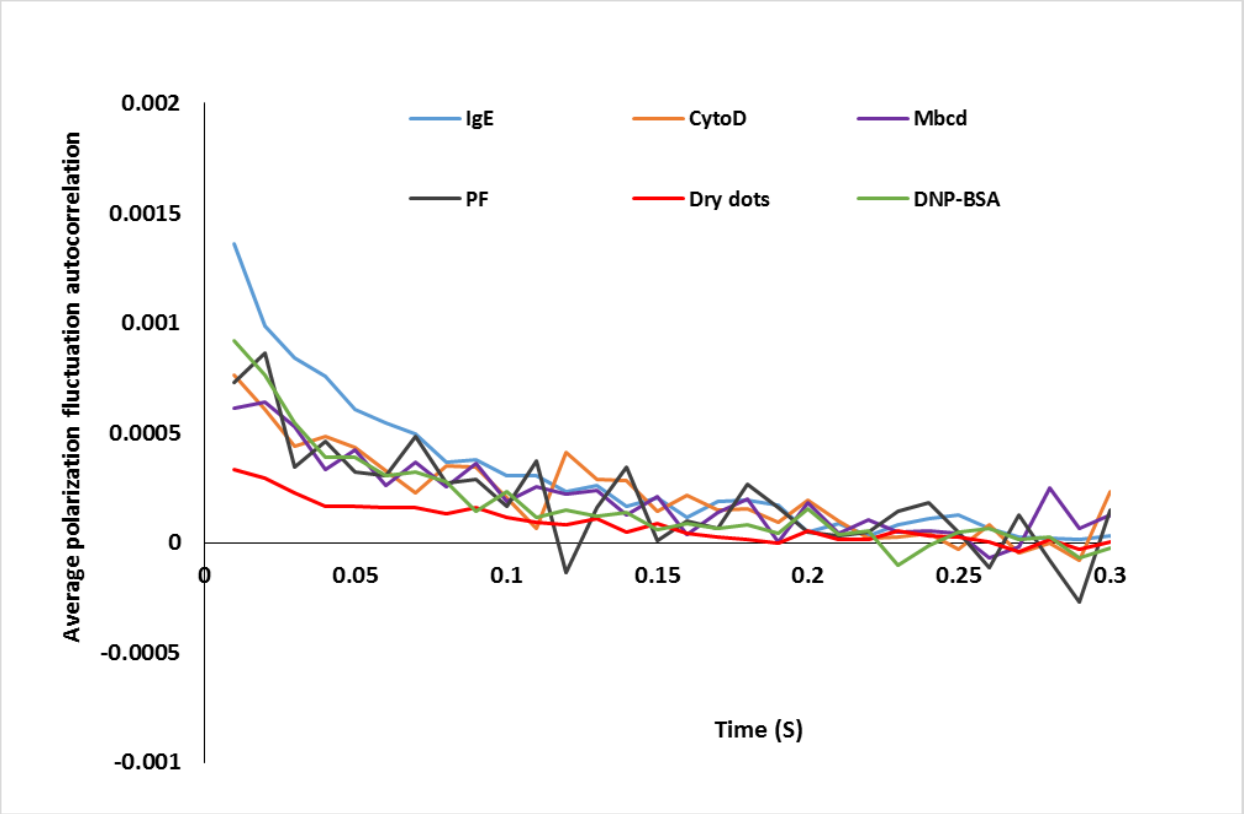

Figure 1.42: Average polarization fluctuation time-autocorrelation function for dry dots on glass, FcεRI on untreated cells and on cells treated with Methyl-β-Cyclodextrin (MβCD), paraformaldehyde (PF), DNP-BSA and cytochalasin D (CytoD).

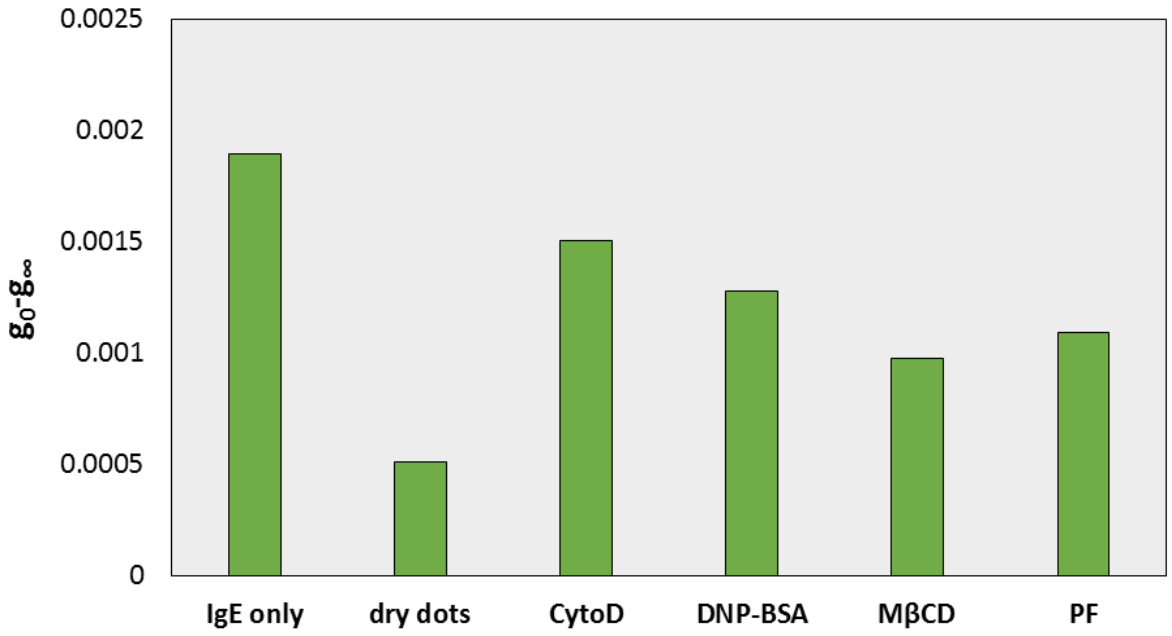

Figure 1.43: Comparison of difference between polarization fluctuation TACF at $\tau=0$ and $\tau=\infty$ for dry dots on glass, for FcεRI on untreated cells and for cells treated with methyl-β-cyclodextrin (MβCD), paraformaldehyde (PF), DNP-BSA and cytochalasin D (CytoD).

IV.A.3. Treatment effects on FcεRI rotational motions.

RBL-2H3 cells were treated with DNP-BSA, paraformaldehyde, MβCD or cytochalasin D. Results shown in Figure 1.44 demonstrate that FcεRI on untreated and treated cells exhibits a range of rotational correlation times (RCT), namely the time constant for exponential decay of the polarization TACF. The difference in correlation times might be attributable to differing sizes of complexes being formed on the membrane cytoplasmic face and/or to receptors being in differing local environments. Membrane compartments can be disrupted when MβCD removes cholesterol from the membrane. Cytochalasin D is an inhibitor of actin polymerization and disrupts the filament component of cytoskeletal networks. FcεRI are aggregated by treatment with DNP-BSA. Paraformaldehyde causes covalent crosslinking of molecules which effectively collects molecule into an insoluble meshwork. Compared with untreated cells, FcεRI are expected to have faster rotational correlation times on cells treated with Cytochalasin D or MβCD. FcεRI is expected to move slowly after DNP-BSA treatment and proteins generally will exhibit their slowest rotational times with paraformaldehyde fixation. Figure 1.44 shows histograms of fitted rotational correlation times. These histograms suggest broad, grossly log-normal, distributions of RCT for QD each cell sample. No clear differences are apparent; the histograms are very similar regardless of treatment with geometric averages of 60-80 ms. As indicated by the histogram shapes, the geometric average is the most appropriate statistic since even a few very slow decays will yield a misleading linear average. These rotational motions thus appear to be a property of the membrane, not of the molecule itself. The results of average rotational correlation times for each condition are described in Table 1.3.

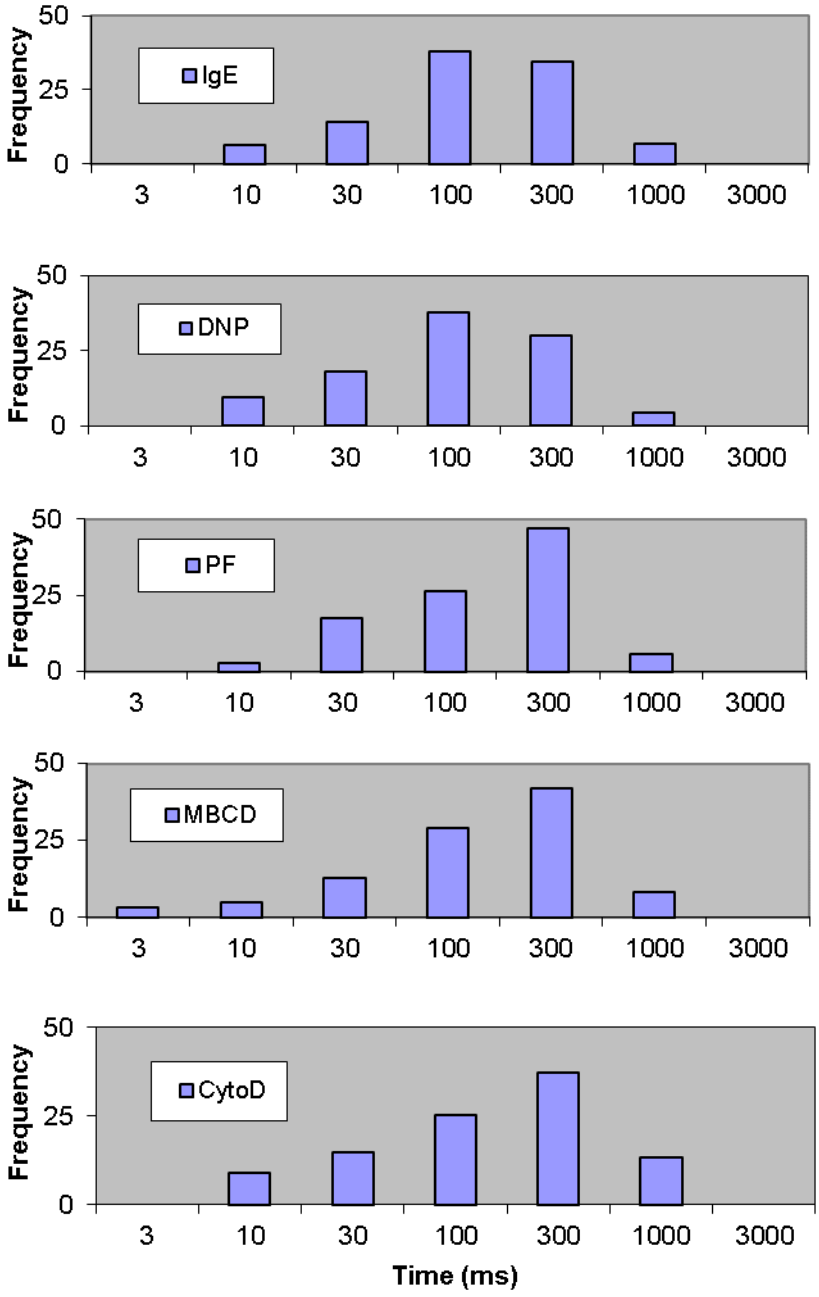

Figure 1.44: Histograms of rotation correlation time distributions for QD on 2H3 cells treated with methyl-β-cyclodextrin (MβCD), paraformaldehyde (PF), DNP-BSA (DNP) and cytochalasin D (CytoD).

Table 1.3: Average rotational correlation times of FcεRI on surface of RBL-2H3 cells subjected to different treatments.

Treatment	Number of QDs examined	Geometric Average Rotational Correlation Time (msec)	Linear Average Rotational Correlation Time (msec)	SD of $\log_{10}$ RCT	SD of linear RCT (msec)
None	205	69	112	0.47	110
DNP-BSA	92	57	98	0.50	104
Paraformaldehyde	54	83	125	0.45	107
MβCD	62	72	126	0.60	109
CytoD	65	75	137	0.55	130

IV.A.4. Implication for membrane dynamics

The question that arises from these results is whether the observed motion represent could represent concerted motion of a larger membrane region surrounding each receptor, namely rotation or libration of individual membrane regions within the larger lipid environment. We know that lipid rafts exhibit lateral motion within the cell surface [90]. Moreover, calculation based on the Saffman-Delbrück model [25] show that a 90 nm diameter membrane region could exhibit unhindered rotational motion with an RCT of about 70 msec (calculation not shown). It is very possible that rotation on our observed time scales could arise from smaller domains with motion hindered by particular membrane regions in which the receptor in embedded. Therefore our results may indicate that individual mesoscale membrane regions rotate or librate with respect to the overall cell surface. *This is an extremely important finding since it suggests the possibility of a type of membrane motion not heretofore considered.*

IV.B. Time-tagged single photon counting rotation measurements

Frame rates of low-light cameras used for our method limit timescale of measurements as previously discussed to >1 msec. Time-tagged photon counting allows measurements on individual QD with measurable correlation times limited only by the photon count rate and acquisition time. Time-tagged single photon counting data as obtained from Becker & Hickl DPC-230 digital photon counter contains a four-byte file entry showing the arrival times for each collected photon. A custom program written in PowerBasic permitted unpacking photon count arrival times into intensity traces showing counts per selected time interval.

It was noted that blinking of single QDs on glass or on cells changed with the excitation power. Blinking was less frequent as laser excitation power on the QD decreased. For example,

Figure 1.45 and Figure 1.46 show intensity traces for same single QD on a cell surface. It is clear that the dot exhibits faster blinking when the laser intensity is attenuated 100x by a 2.0OD neutral density filter than when attenuated 300x by 2.5OD neutral density filter. Dots also exhibit abnormal behavior at very high illumination levels. For example, Figure 1.47 shows the intensity trace for a single dot illuminated by a 300x-attenuated (2.5OD) laser beam while Figure 1.48 shows a dot illuminated with the unattenuated laser beam. At the higher power level, the trace cannot be recognized as arising from a quantum dot. Laser power and count rates were measured the power for different filter attenuations with results shown in Table 1.4. Based on these results, subsequent measurements were performed using a 2.5 OD filter.

The goal in these experiments is to extend the time range of polarization fluctuation TACF towards shorter correlation times. The ultimate goal is to reach, and examine by this method, the 80 µs RCT exhibited by unrestricted FceRI and which agrees with hydrodynamic calculation based on the receptor size. Thus it is convenient to bin data at 1 µs intervals. However, this demonstrates the difficulty of dealing with data intended to reveal such rapid RCT. Experiments thus far have had durations of 10-100s. At 1 µs per point, the binned files would require 40-400 MB. While this does not pose serious difficulties, calculating polarization and intensity fluctuation TACFs from such arrays does. Normal methods for such calculations involve FFT-based correlations and these are not practical for arrays of such sizes. For preliminary studies, an approach based on "multi-tau" correlation calculations has been employed which in effect calculates the TACF at logarithmically-distributed points. This is the approach employed in commercial correlators used in FCS apparatuses. However, such correlators save only an evolving TACF and do not permit re-analysis of raw data. The program developed in our laboratory opens a raw time-tagged single photon counting data files, produces

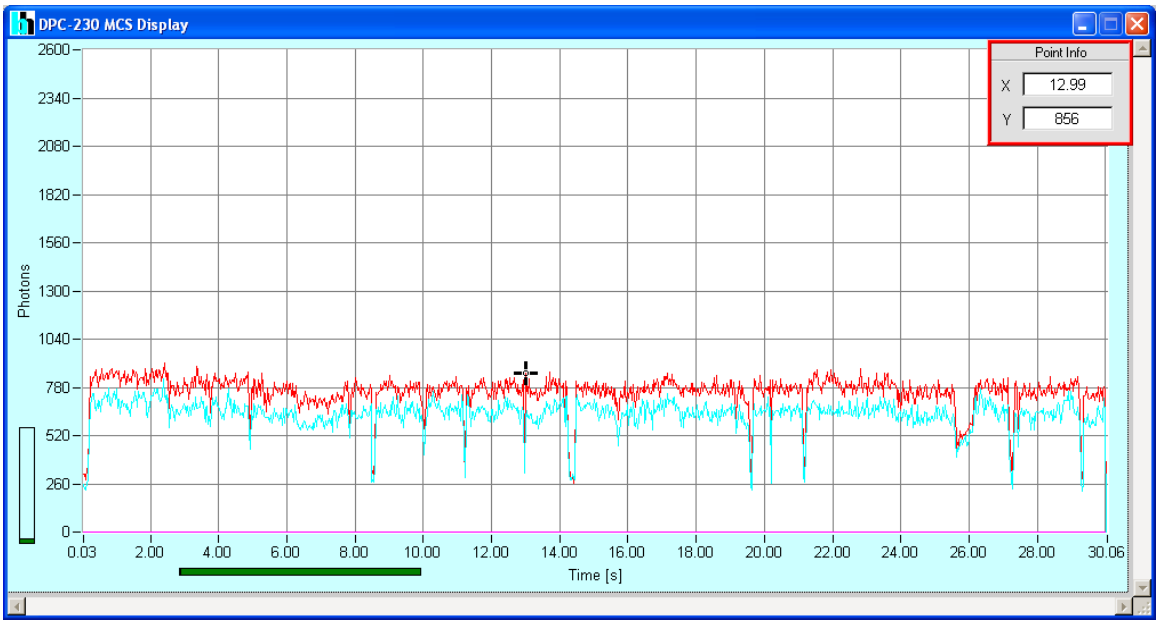

Figure 1.44: Photon counts per 30 msec interval vs. time for single QD 655 on 2H3 cell. Laser attenuation by 2.5OD neutral density filter.

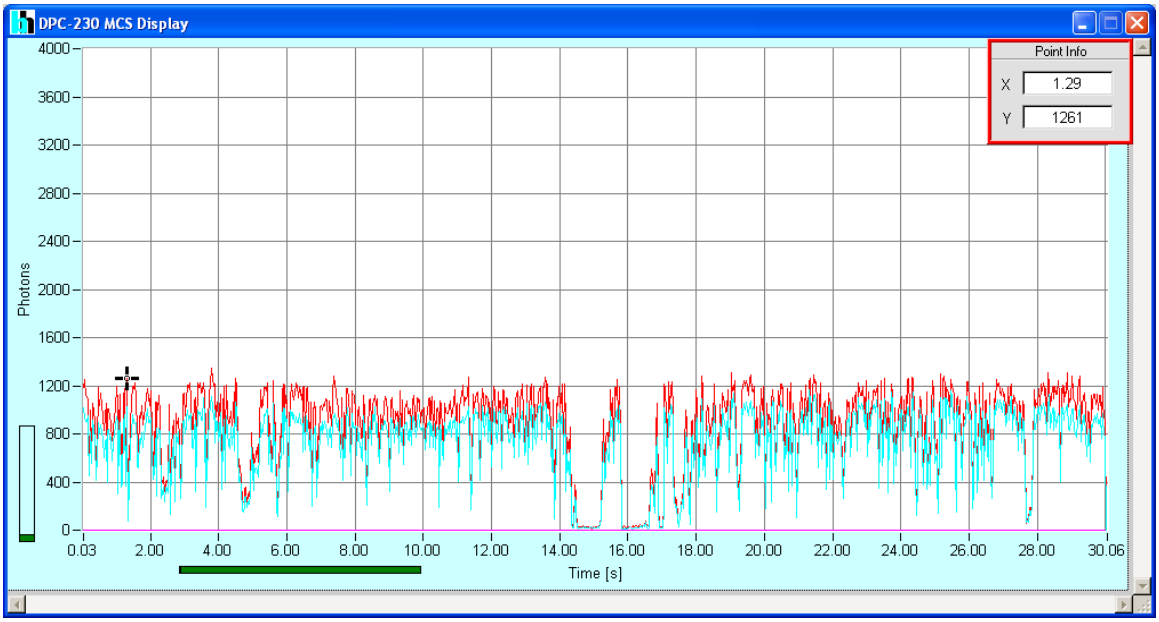

Figure 1.45: Photon counts per 30 msec interval vs. time for single QD 655 on a 2H3 cell. Laser attenuation by 2.0OD neutral density filter.

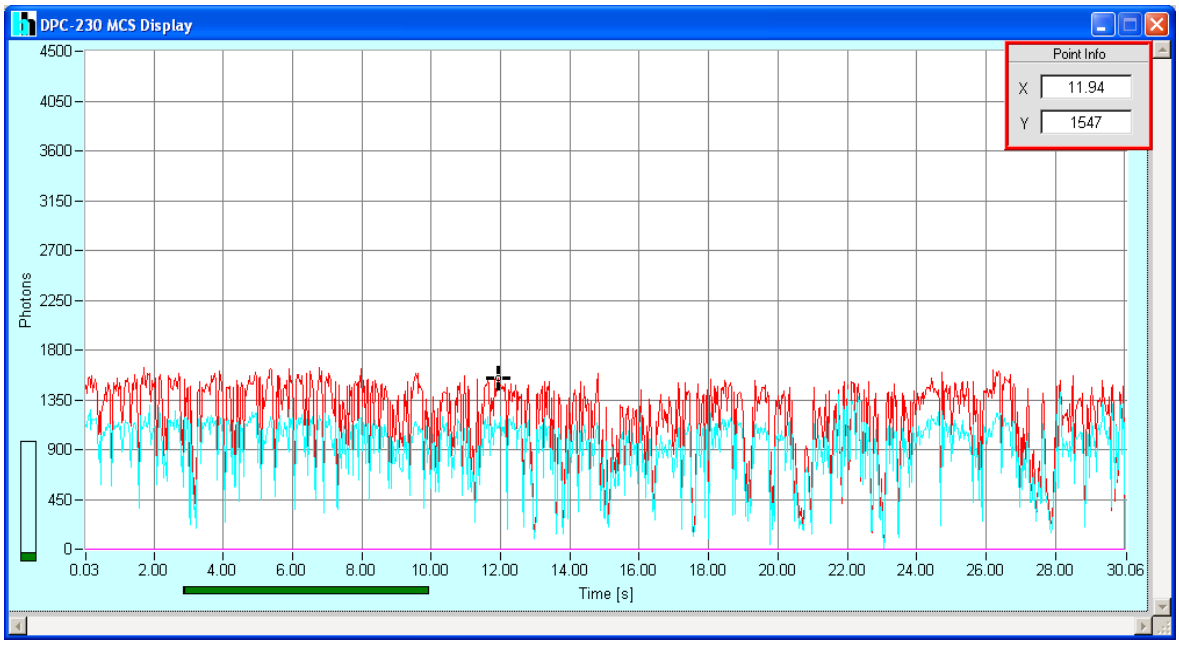

Figure 1.46: Photon counts per 30 msec interval vs. time for single QD 655 on 2H3 cell. Laser attenuation by 2.5OD neutral density filter.

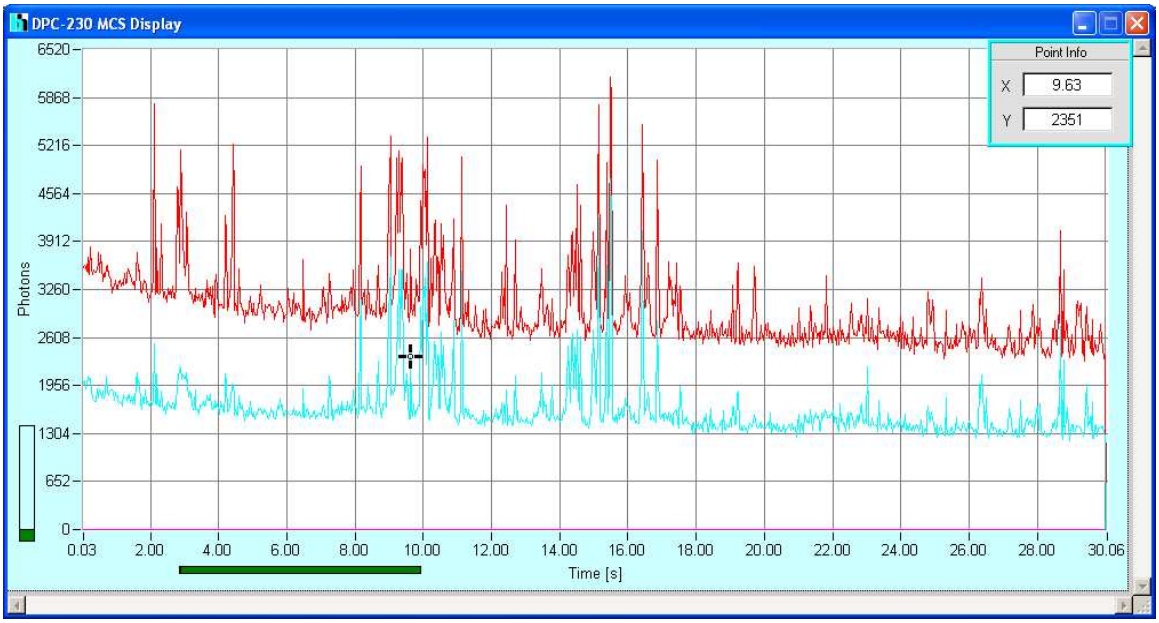

Figure 1.47: Photon counts per 30 msec interval vs. time for single QD 655 on 2H3 cell. Laser unattenuated – no neutral density filter.

Table 1.4: Fluorescence intensities measured for single QDs illuminated by various laser intensities and with imaging by objectives of differing light collection efficiencies.

Optical density of filter attenuating laser beam	Excitation intensity on dot ($W\ cm^{-2}$) Objective 60x 1.2NA	Excitation intensity on dot ($W\ cm^{-2}$) Objective 100x 1.4NA
1.0	1513.6	_
1.5	473.8	_
2.0	140.8	715.1
2.5	49.6	233.7
3.0	16.9	84.2
3.5	4.1	35.6

a multi-channel scaling (MCS) intensity trace at any desired bin width and for a specified set of instrument parameters corresponding to the g-factor and camera and cell background parameters discussed for imaging data, calculates polarization and intensity fluctuation TACFs for 90 correlation times from 1 µs to 26 s. Integrating this correlation calculation with experimental parameter optimization like that used with imaging data has yet to be accomplished.

Figures 1.49-1.52 show MCS intensity traces, as provided by Becker & Hickl software, for single QD 655s on glass and bound to FceRI on a RBL-2H3 cell. Figure 1.53 shows a polarization fluctuation TACF correlation trace with a minimum 1 µsec correlation obtained from the software developed in our laboratory. Given the photon count rate of ~15,000 cps exhibited by the QD shown in this trace, only TACF values for correlation times above ~100 µsec are significant. However, the data make clear that our methods can successfully calculate polarization fluctuation TACFs down to microsecond correlation times.

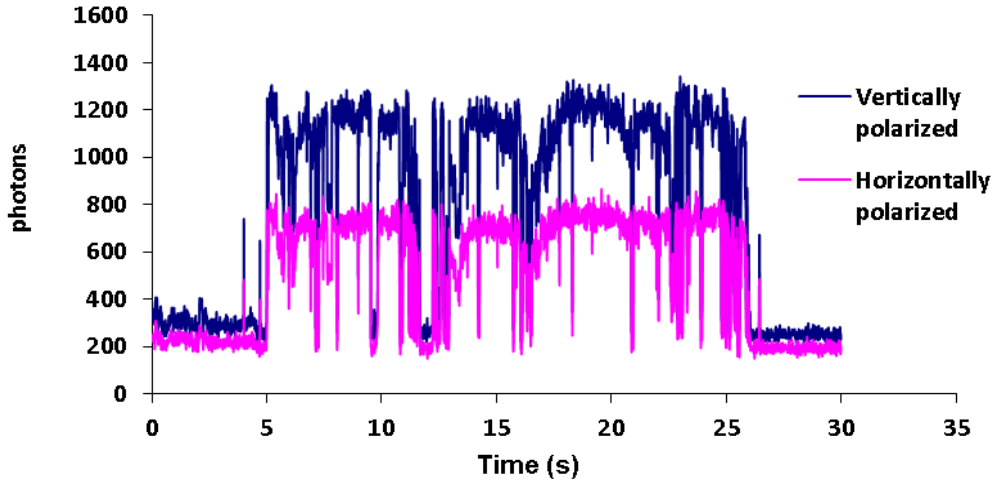

Figure 1.48: Photon counts per 30 msec interval vs. time for single QD 655 a on glass.

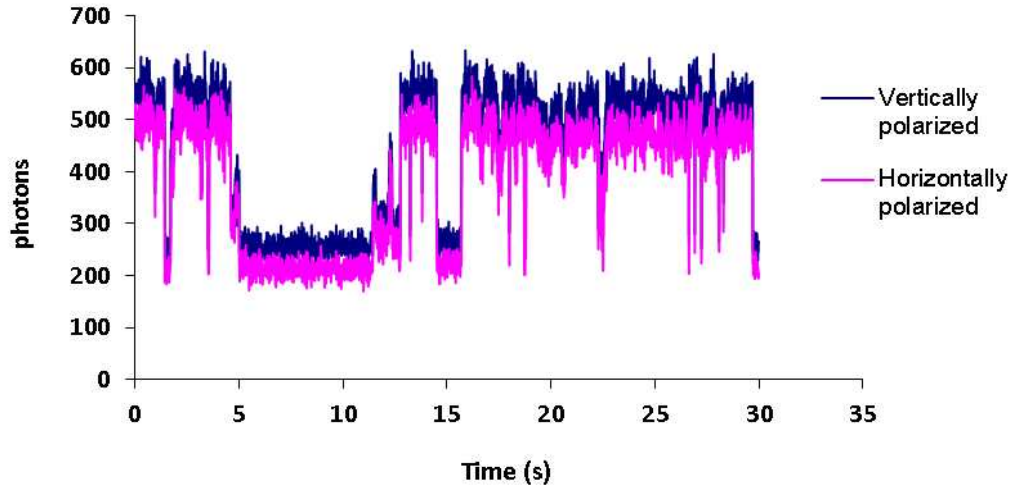

Figure 1.49: Photon counts per 30 msec interval vs. time for a single QD 655 b on glass.

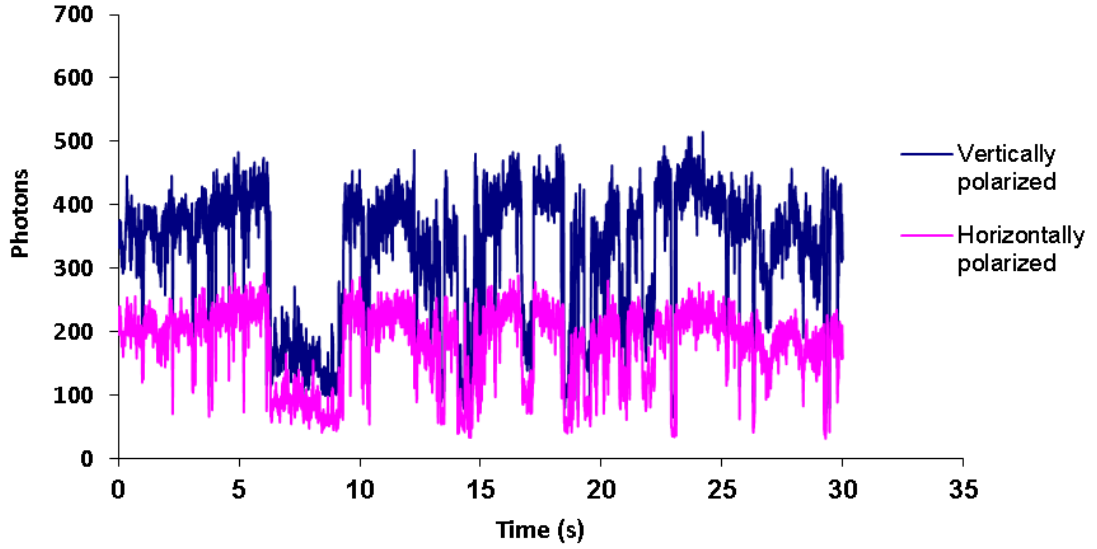

Figure 1.50: Photon counts per 30 msec interval vs. time for single QD 655 a on a RBL- 2H3 cell.

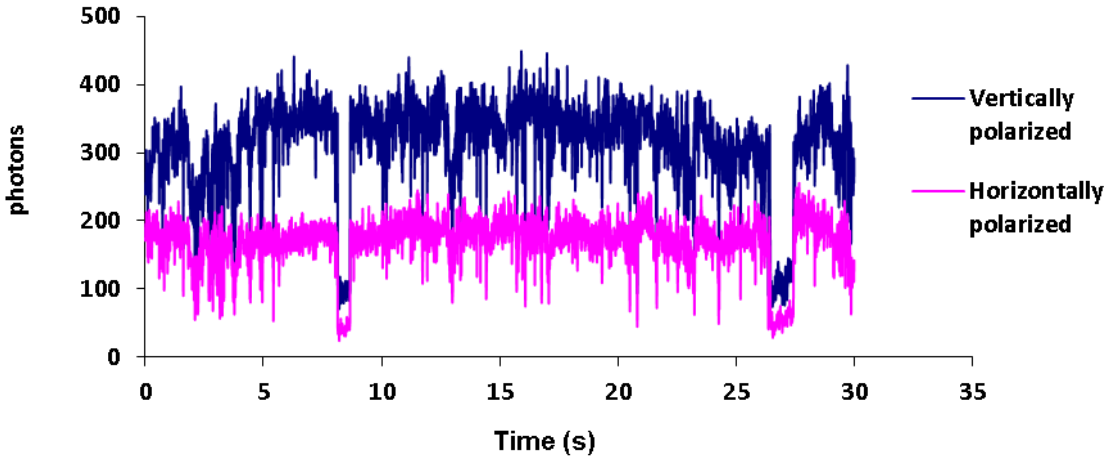

Figure 1.51: Photon counts per 30 msec interval vs. time for single QD 655 b on a RBL- 2H3 cell.

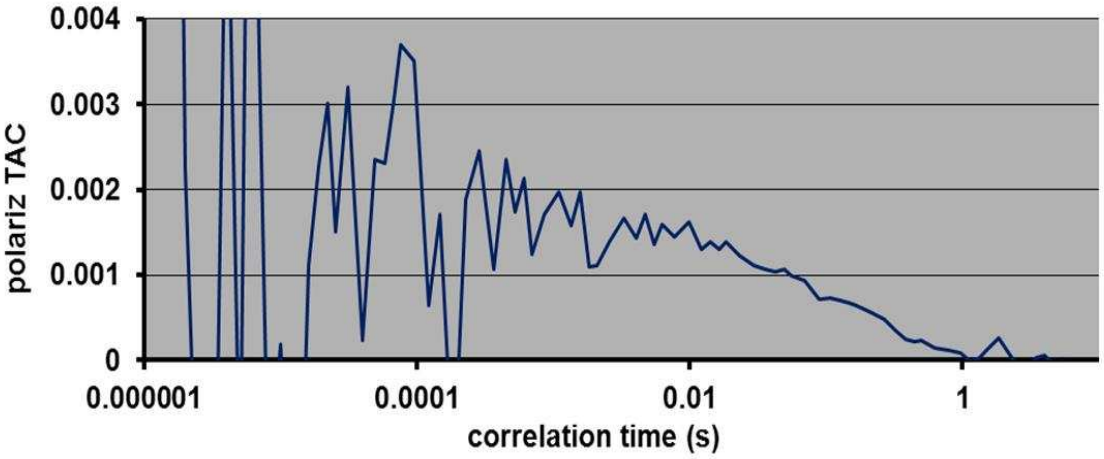

Figure 1.52: A polarization correlation trace with 1 µsec time resolution for a QD 655 on 2H3 cell.

V. CONCLUSIONS AND FUTURE DIRECTIONS

The study of biomolecular dynamics *in vivo* is essential to our understanding of complex biological systems and affects our capacity to identify physical phenomena and treat disease. We have developed two techniques to measure rotation of single molecules on the cell surface. These rotational motion measurements allow examination of membrane motions over the microsecond to multiple-second timescale. This is an improvement on previous methods where frame rates of low-light cameras limited imaging techniques to rotational correlation times greater than 1 msec. Time-tagged photon counting of single quantum dots provides polarization fluctuation data on sub-μsec timescales.

The real time FcεRI rotation on 2H3 cell surface via QD probes has been studied for the first time. It represents a qualitative improvement in bioanalytical methods. Quantum dot probes have also enabled imaging measurements of RBL-2H3 cell FcεRI rotation, on the >10 msec timescale. Imaging results demonstrate a range of rotational behavior among individual molecules. Observed slow rotation accounts for a substantial part of the apparent molecular immobility suggested by previous work [91]. Such slow motions, not observable previously, may occur with large signaling complexes, which are important targets of study in cell biology. These slow motions appear to be a property of the membrane itself, not of the receptor state. Our results may indicate that individual mesoscale membrane regions rotate or librate with respect to the overall cell surface.

Future imaging studies will explore polarized illumination whereas, the current fluorescence imaging method, non-polarized illumination has been used. Another imaging improvement to be explored is the use of higher-speed cameras becoming available which

combine sub-millisecond frame times with adequate low-light sensitivity. Compared with imaging methods, the removal of QD blinking is more complex in photon counting methods. A program is currently being developed for use on time-tagged single photon counting data to optimize experimental parameters like g-factor and so eliminate blinking effects on polarization fluctuation TACFs. To facilitate measurements by both imaging and photon counting approaches, we will examine new non-blinking QD to see if their size, asymmetry and photophysics are suitable for our experiments. The absence of QD blinking would facilitate both methods.

We anticipate applying both imaging and photon-counting methods to examine the rotational dynamics of other cell surface receptors and how these dynamics reflect receptor aggregation, interaction with other molecules or more nonspecific environmental factors such as local membrane microviscosity,

REFERENCES

1. van Meer, G., Cellular lipidomics, *Embo Journal* **24**, 3159-3165 (2005).
2. Gorter, E., and Grendel, R., On biomolecular layers of lipid on the chromacytes of the blood, *Journal of Experimental Medicine* **41**, 439-443 (1925).
3. Danielli, J. F., and Davson, H., A contribution to the theory of permeability of thin films, *J. Cell. Physiol.* **5**, 495-508 (1935).
4. Singer, S. J., and Nicolson, G. L., The fluid mosaic model of the structure of cell membranes. Cell membranes are viewed as two-dimensional solutions of oriented globular proteins and lipids, *Science* **175**, 720-731 (1972).
5. Sanderson, J. M., Resolving the kinetics of lipid, protein and peptide diffusion in membranes, *Molecular Membrane Biology* **29**, 118-143 (2012).
6. Nicolson, G. L., The Fluid-Mosaic Model of Membrane Structure: Still relevant to understanding the structure, function and dynamics of biological membranes after more than 40 years, *Biochimica Et Biophysica Acta-Biomembranes* **1838**, 1451-1466 (2014).
7. Ritchie, K., Iino, R., Fujiwara, T., Murase, K., and Kusumi, A., The fence and picket structure of the plasma membrane of live cells as revealed by single molecule techniques (review), *Molecular Membrane Biology* **20**, 13-18 (2003).
8. Kusumi, A., Fujiwara, T. K., Chadda, R., Xie, M., Tsunoyama, T. A., Kalay, Z., Kasai, R. S., and Suzuki, K. G. N., Dynamic Organizing Principles of the Plasma Membrane that Regulate Signal Transduction: Commemorating the Fortieth Anniversary of Singer and Nicolson's Fluid-Mosaic Model, *Annual Review of Cell and Developmental Biology*, **28**, 215-250 (2012).

9. Nishida, N., Osawa, M., Takeuchi, K., Imai, S., Stampoulis, P., Kofuku, Y., Ueda, T., and Shimada, I., Functional dynamics of cell surface membrane proteins, *Journal of Magnetic Resonance* **241**, 86-96 (2014).

10. Lasne, D., Blab, G. A., Berciaud, S., Heine, M., Groc, L., Choquet, D., Cognet, L., and Lounis, B., Single nanoparticle photothermal tracking (SNaPT) of 5-nm gold beads in live cells, *Biophysical Journal* **91**, 4598-4604 (2006).

11. Frye, L. D., and Edidin, M., The rapid intermixing of cell surface antigens after formation of mouse-human heterokaryons, *Journal of Cell Science* **7**, 319-335 (1970).

12. Kusumi, A., Koyama-Honda, I., and Suzuki, K., Molecular dynamics and interactions for creation of stimulation-induced stabilized rafts from small unstable steady-state rafts, *Traffic* **5**, 213-230 (2004).

13. Jacobson, K., Ishihara, A., and Inman, R., Lateral diffusion of proteins in membranes, *Annual Review of Physiology* **49**, 163-175 (1987).

14. Nicolson, G. L., and Poste, G., Medical progress. the caner cell: dynamic aspects and modifications in cell-surface organization (first of two parts), *The New England Journal of Medicine* **295, no. 4**, 197-203 (1976).

15. Zhang, F., Lee, G. M., and Jacobson, K., Protein lateral mobility as a reflection of membrane microstructure, *BioEssays* **15**, 579-588 (1993).

16. Kusumi, A., Sako, Y., and Yamamoto, M., Confined lateral diffusion of membrane receptors as studied by single particle tracking (nanovid microscopy). Effects of calcium-induced differentiation in cultured epithelial cells, *Biophysical Journal* **65**, 2021-2040 (1993).

17. Haggie, P. M., Kim, J. K., Lukacs, G. L., and Verkman, A. S., Tracking of quantum dot-labeled CFTR shows near immobilization by C-terminal PDZ interactions, *Molecular Biology of the Cell* **17**, 4937-4945 (2006).

18. Crane, J. M., Van Hoek, A. N., Skach, W. R., and Verkman, A. S., Aquaporin-4 dynamics in orthogonal Arrays in live cells visualized by quantum dot single particle tracking, *Molecular Biology of the Cell* **19**, 3369-3378 (2008).

19. Jacobson, K., Sheets, E. D., and Simson, R., Revisiting the Fluid Mosaic Model of Membranes, *Science* **268**, 1441-1442 (1995).

20. Iino, R., Koyama, I., and Kusumi, A., Single molecule imaging of green fluorescent proteins in living cells: E-cadherin forms oligomers on the free cell surface, *Biophysical Journal* **80**, 2667-2677 (2001).

21. Murase, K., Fujiwara, T., Umemura, Y., Suzuki, K., Iino, R., Yamashita, H., Saito, M., Murakoshi, H., Ritchie, K., and Kusumi, A., Ultrafine membrane compartments for molecular diffusion as revealed by single molecule techniques, *Biophysical Journal* **86**, 4075-4093 (2004).

22. Kusumi, A., and Suzuki, K., Toward understanding the dynamics of membrane-raft-based molecular interactions, *Biochimica Et Biophysica Acta-Molecular Cell Research* **1746**, 234-251 (2005).

23. Saffman, P. G., and Delbruck, M., Brownian motion in biological membranes, *Proc. Nat. Acad, Sci.* **72, no. 8**, 3111-3113 (1975).

24. Fooksman, D. R., Edidin, M., and Barisas, B. G., Measuring rotational diffusion of MHC class I on live cells by polarized FPR, *Biophys Chem* **130**, 10-16. Epub 2007 Jul 2006. (2007).

25. Saffman, P. G., and Delbrück, M., Brownian motion in biological membranes, *Proceedings of the National Academy of Science (USA)* **72**, 3111-3113 (1975).

26. Rahman, N. A., Philpott, C. J., Barisas, B. G., and Roess, D. A., Gonadotropiin effects on luteinizing hormone receptor structure examined by time-resolved phosphorescence anisotropy and photoproximity labeling, *The FASEB Journal* **6**, A018 (1992).

27. Damjanovich, S., Tron, L., Szollosi, J., Zidovetzki, R., Vaz, W. L. C., Regateiro, F., Arndt-Jovin, D. J., and Jovin, T. M., Distribution and mobility of murine histocompatibility H-2K^k antigen in the cytoplasmic membrane, *Proceedings of the National Academy of Science (USA)* **80**, 5985-5989 (1983).

28. Zidovetzki, R., Yarden, Y., Schlessinger, J. D., and Jovin, T. M., Rotational diffusion of epidermal growth factor complexes to cell surface receptors reflect rapid microaggregation and endocytosis of occupied receptors, *Proceedings of the National Academy of Science (USA)* **8**, 1337-1341 (1985).

29. Gu, Y., Sun, W., Wang, G., Jeftinija, K., Jeftinija, S., and Fang, N., Rotational dynamics of cargos at pauses during axonal transport, *Nature Communications* **3** (2012).

30. Goni, F. M., The basic structure and dynamics of cell membranes: An update of the Singer-Nicolson model, *Biochimica Et Biophysica Acta-Biomembranes* **1838**, 1467-1476 (2014).

31. Cherry, R. J., Rotational diffusion of membrane proteins: measurements with bacteriorhodopsin, band-3 proteins and erythrocyte oligosaccharides, *Biochem Soc Symp*, 183-190. (1981).

32. Squier, T. C., Bigelow, D. J., and Thomas, D. D., Lipid fluidity directly modulates the overall protein rotational mobility of the Ca-ATPase in sarcoplasmic reticulum, *J Biol Chem* **263**, 9178-9186. (1988).

33. Cone, R. A., Rotational Diffusion of Rhodopsin in the Visual Receptor Membrane, *Nature New Biol.* **236**, 39-43 (1972).

34. Naqvi, K. R., Gonzalez-Rodriguez, J., Cherry, R., and Chapman, D., Spectroscopic technique for studying protein rotation in membranes, *Nature New Biology* **245**, 249-251 (1973).

35. Lakowicz, J. R. *Principles of fluorescence spectroscopy*, 3rd ed., Springer, New York, (2006).

36. Jameson, D. M., and Ross, J. A., Fluorescence Polarization/Anisotropy in Diagnostics and Imaging, *Chemical Reviews* **110**, 2685-2708 (2010).

37. Garland, P., and Johnson, P. Rotational diffusion of membrane proteins optical methods, In *Enzymes of Biological Membranes* (Martonosi, A., Ed.) 2nd ed., pp 421-439, Plenum Press, New York, (1985).

38. Song, J., Hagen, G., Roess, D. A., Pecht, I., and Barisas, B. G., Time-resolved phorescence anisotropy studies of the mast cell function-associated antigen and its interactions with the Type I Fce receptor, *Biochemistry* **41**, 880-889 (2002).

39. Austin, R. H., Chan, S. S., and Jovin, T. M., Rotational diffusion of cell surface components by time-resolved phosphorescence anisotropy, *Proceedings of the National Academy of Science (USA)* **76**, 5650-5654 (1979).

40. Johnson, P., and Garland, P., Fluorescent triplet probes for measuring the rotational diffusion of membrane proteins, *Biochemistry Journal* **203**, 313-321 (1982).

41. Johnson, P., and Garland, P. B., Depolarization of fluorescence depletion. A microscopic method for measuring rotational diffusion of membrane proteins on the surface of a single cell, *FEBS Lett* **132**, 252-256. (1981).

42. Corin, A. F., Blatt, E., and Jovin, T. M., Triplet-state detection of labeled proteins using fluorescence recovery spectroscopy, *Biochemistry* **26**, 2207-2217 (1987).

43. Barisas, B. G., Roess, D. A., Pecht, I., and Rahman, N. A., Rotational dynamics of Fc_e receptors on individual 2H3 RBL cells studied by polarized fluorescence depletion, *Biophysical Journal* **75**, 671 (1990).

44. Rahman, N. A., Pecht, I., Roess, D. A., and Barisas, B. G., Rotational dynamics of Fc receptors on individually-selected rat mast cells studied by polarized fluorescence depletion, *Biophysical Journal* **161**, 334-361 (1992).

45. Barisas, B. G., Londo, T. R., Herman, J. R., Rahman, N. A., and Roess, D. A., Advances in polarized fluorescence depletion measurement of cell membrane protein rotation, *Biophysical Journal* **59**, 351a (1991).

46. Zarrin, F., Yoshida, T. M., and Barisas, B. G., Frequency domain measurement of protein rotational motion using polarized fluorescence depletion, *Biophysical Journal* **49**, 61a (1986).

47. Yoshida, T. M., Zarrin, F., and Barisas, B. G., Measurement of protein rotational motion using frequency domain polarized fluorescence depletion, *Biophysical Journal* **54**, 277-288 (1988).

48. Schwille, P. Fluorescence correlation spectroscopy and its potential for intracellular applications, In *Cell Biochemistry and Biophysics*, pp 383-408, Humana Press Inc. (2001).

49. Peter Kapusta, M. W., Applications, :Rainer Erdmann Advanced Photon Counting .(2015) Springer International Publishing ,128-Methods, Instrumentation, pp 111

50. Pinaud, F., Clarke, S., Sittner, A., and Dahan, M., Probing cellular events, one quantum dot at a time, *Nature Methods* **7**, 275-285 (2010).

51. Bruchez, M., Moronne, M., Gin, P., Weiss, S., and Alivisatos, A. P., Semiconductor nanocrystals as fluorescent biological labels, *Science* **281**, 2013-2016 (1998).

52. Rosenthal, S. J., Chang, J. C., Kovtun, O., McBride, J. R., and Tomlinson, I. D., Biocompatible Quantum Dots for Biological Applications, *Chemistry & Biology* **18**, 10-24 (2011).

53. Michalet, X., Pinaud, F. F., Bentolila, L. A., Tsay, J. M., Doose, S., Li, J. J., Sundaresan, G., Wu, A. M., Gambhir, S. S., and Weiss, S., Quantum dots for live cells, in vivo imaging, and diagnostics, *Science* **307**, 538-544 (2005).

54. Lee, S. F., and Osborne, M. A., Photodynamics of a single quantum dot: Fluorescence activation, enhancement, intermittency, and decay, *Journal of the American Chemical Society* **129**, 8936-+ (2007).

55. van Sark, W., Frederix, P., Van den Heuvel, D. J., Gerritsen, H. C., Bol, A. A., van Lingen, J. N. J., Donega, C. D., and Meijerink, A., Photooxidation and photobleaching of single CdSe/ZnS quantum dots probed by room-temperature time-resolved spectroscopy, *Journal of Physical Chemistry B* **105**, 8281-8284 (2001).

56. Chen, H., Gai, H., and Yeung, E. S., Inhibition of photobleaching and blue shift in quantum dots, *Chemical Communications*, 1676-1678 (2009).

57. Chan, W.-Y., Molecular Genetic, Biochemical, and Clinical Implications of Gonadotropin Receptor Mutations, *Molecular Genetics and Metabolism* **63**, 75 - 84 (1998).

58. Jamieson, T., Bakhshi, R., Petrova, D., Pocock, R., Imani, M., and Seifalian, A. M., Biological applications of quantum dots, *Biomaterials* **28**, 4717-4732 (2007).

59. Kadavanich, A. V., Kippeny, T. C., Erwin, M. M., Pennycook, S. J., and Rosenthal, S. J., Sublattice resolution structural and chemical analysis of individual CdSe nanocrystals using atomic number contrast scanning transmission electron microscopy and electron energy loss spectroscopy, *Journal of Physical Chemistry B* **105**, 361-369 (2001).

60. Medintz, I. L., Uyeda, H. T., Goldman, E. R., and Mattoussi, H., Quantum dot bioconjugates for imaging, labelling and sensing, *Nature Materials* **4**, 435-446 (2005).

61. Dabbousi, B. O., RodriguezViejo, J., Mikulec, F. V., Heine, J. R., Mattoussi, H., Ober, R., Jensen, K. F., and Bawendi, M. G., (CdSe)ZnS core-shell quantum dots: Synthesis and characterization of a size series of highly luminescent nanocrystallites, *Journal of Physical Chemistry B* **101**, 9463-9475 (1997).

62. Chan, W. C. W., and Nie, S. M., Quantum dot bioconjugates for ultrasensitive nonisotopic detection, *Science* **281**, 2016-2018 (1998).

63. Nirmal, M., Dabbousi, B. O., Bawendi, M. G., Macklin, J. J., Trautman, J. K., Harris, T. D., and Brus, L. E., Fluorescence intermittency in single cadmium selenide nanocrystals, *Nature* **383**, 802-804 (1996).

64. Fu, Y., Zhang, J., and Lakowicz, J. R., Suppressed blinking in single quantum dots (QDs) immobilized near silver island films (SIFs), *Chem Phys Lett* **447**, 96-100 (2007).

65. Biebricher, A., Sauer, M., and Tinnefeld, P., Radiative and nonradiative rate fluctuations of single colloidal semiconductor nanocrystals, *Journal of Physical Chemistry B* **110**, 5174-5178 (2006).

66. Fomenko, V., and Nesbitt, D. J., Solution control of radiative and nonradiative lifetimes: A novel contribution to quantum dot blinking suppression, *Nano Letters* **8**, 287-293 (2008).

67. Hohng, S., and Ha, T., Near-complete suppression of quantum dot blinking in ambient conditions, *Journal of the American Chemical Society* **126**, 1324-1325 (2004).

68. Wang, X., Ren, X., Kahen, K., Hahn, M. A., Rajeswaran, M., Maccagnano-Zacher, S., Silcox, J., Cragg, G. E., Efros, A. L., and Krauss, T. D., Non-blinking semiconductor nanocrystals, *Nature* **459**, 686-689 (2009).

69. Keller, A. M., Ghosh, Y., DeVore, M. S., Phipps, M. E., Stewart, M. H., Wilson, B. S., Lidke, D. S., Hollingsworth, J. A., and Werner, J. H., 3-Dimensional Tracking of Non-blinking 'Giant' Quantum Dots in Live Cells, *Advanced Functional Materials* **24**, 4796-4803 (2014).

70. Pelton, M., Smith, G., Scherer, N. F., and Marcus, R. A., Evidence for a diffusion-controlled mechanism for fluorescence blinking of colloidal quantum dots, *Proceedings of the National Academy of Sciences of the United States of America* **104**, 14249-14254 (2007).

71. Cichos, F., von Borczyskowski, C., and Orrit, M., Power-law intermittency of single emitters, *Current Opinion in Colloid & Interface Science* **12**, 272-284 (2007).

72. Efros, A. L., and Rosen, M., Random telegraph signal in the photoluminescence intensity of a single quantum dot, *Phys Rev Lett* **78**, 1110-1113 (1997).

73. Frantsuzov, P. A., Volkan-Kacso, S., and Janko, B., Model of Fluorescence Intermittency of Single Colloidal Semiconductor Quantum Dots Using Multiple Recombination Centers, *Phys Rev Lett* **103** (2009).

74. Voznyy, O., and Sargent, E. H., Atomistic Model of Fluorescence Intermittency of Colloidal Quantum Dots, *Phys Rev Lett* **112** (2014).

75. Bachir, A. I., Durisic, N., Hebert, B., Grutter, P., and Wiseman, P. W., Characterization of blinking dynamics in quantum dot ensembles using image correlation spectroscopy, *Journal of Applied Physics* **99** (2006).

76. Jain, P. K., Lee, K. S., El-Sayed, I. H., and El-Sayed, M. A., Calculated absorption and scattering properties of gold nanoparticles of different size, shape, and composition: Applications in biological imaging and biomedicine, *Journal of Physical Chemistry B* **110**, 7238-7248 (2006).

77. Sonnichsen, C., and Alivisatos, A. P., Gold nanorods as novel nonbleaching plasmon-based orientation sensors for polarized single-particle microscopy, *Nano Letters* **5**, 301-304 (2005).

78. Pierrat, S., Hartinger, E., Faiss, S., Janshoff, A., and Soennichsen, C., Rotational Dynamics of Laterally Frozen Nanoparticles Specifically Attached to Biomembranes, *J Phys Chem C* **113**, 11179-11183 (2009).

79. Spetzler, D., York, J., Daniel, D., Fromme, R., Lowry, D., and Frasch, W., Microsecond time scale rotation measurements of single F1-ATPase molecules, *Biochemistry* **45**, 3117-3124 (2006).

80. Chang, W.-S., Ha, J. W., Slaughter, L. S., and Link, S., Plasmonic nanorod absorbers as orientation sensors, *Proceedings of the National Academy of Sciences of the United States of America* **107**, 2781-2786 (2010).

81. Wang, G., Sun, W., Luo, Y., and Fang, N., Resolving Rotational Motions of Nano-objects in Engineered Environments and Live Cells with Gold Nanorods and Differential Interference Contrast Microscopy, *Journal of the American Chemical Society* **132**, 16417-16422 (2010).

82. Xiao, L., Qiao, Y., He, Y., and Yeung, E. S., Imaging Translational and Rotational Diffusion of Single Anisotropic Nanoparticles with Planar Illumination Microscopy, *Journal of the American Chemical Society* **133**, 10638-10645 (2011).

83. Daeron, M., Fc receptor biology, *Annual Review of Immunology* **15**, 203-234 (1997).

84. Gilfillan, A. M., and Tkaczyk, C., Integrated signalling pathways for mast-cell activation, *Nature Reviews Immunology* **6**, 218-230 (2006).

85. Cantor, C. R. S., P. R. *Biophysical Chemistry*, Freeman, San Francisco, (1980).

86. Gould, H. J., and Sutton, B. J., IgE in allergy and asthma today, *Nature Reviews Immunology* **8**, 205-217 (2008).

87. Song, J., Hagen, G. M., Roess, D. A., Pecht, I., and Barisas, B. G., The mast cell function-associated antigen and its interactions with the type I Fcepsilon receptor, *Biochemistry* **41**, 881-889 (2002).

88. Song, J., Hagen, G., Smith, S. M., Roess, D. A., Pecht, I., and Barisas, B. G., Interactions of the mast cell function-associated antigen with the type I Fcepsilon receptor, *Molecular Immunology* **38**, 1315-1321 (2002).

89. Schwille, P., Haupts, U., Maiti, S., and Webb, W. W., Molecular dynamics in living cells observed by fluorescence correlation spectroscopy with one- and two-photon excitation, *Biophysical Journal* **77**, 2251-2265 (1999).

90. Day, C., and Kenworthy, A., Tracking microdomain dynamics in cell membranes, *Biochim Biophys Acta* **1788**, 245-253 (2009).

91. Song, J., Hagen, G., Smith, S. M. L., Roess, D. A., Pecht, I., and Barisas, B. G., Interactions of the Mast Cell Function-Associated Antigen with the Type I Fce Receptor, *Molecular Immunology* **38**, 1315-1322 (2002).

LIST OF ABBREVIATIONS

$2H_3$:	rat mucosal-type mast cells of the $2H_3$ cell line
BSA:	bovine serum albumin
CdSe:	cadmium selenide
CytoD:	cytochalasin D
DIC:	differential interference contrast
DNP:	2, 4-dinitrophenol
FCS:	fluorescence correlation spectroscopy
FcεRI:	type 1 Fc receptor for IgE
FDA:	fluorescence depletion anisotropy
FPR:	fluorescence photobleaching recovery
FPI:	fluorescence polarization imaging
GPI:	glycosylphos phatidylinositol
IgE:	immunoglobulin of type E
MCS:	multi-channel scaling
MRC:	multiple recombination centers
MβCD:	methyl-β-cyclodextrin
PF:	paraformaldehyde
QDs:	quantum dots
RCT:	rotational correlation times
ROI:	regions of interest
Second:	sec
SPT:	single particle tracking

TACF: time-auto correlation functions

TCSPC: time-correlated single-photon counting

TPA: time-resolved phosphorescence anisotropy

ZnS: zinc sulfide

CHAPTER II

USE OF THE ICUE3 cAMP REPORTER TO EVALUATE LUTEINIZING HORMONE (LH) RECEPTOR FUNCTION

I. BACKGROUND

I.A. LH and hCG

Luteinizing hormone (LH) and human chorionic gonadotropin (hCG) play key roles in reproduction. LH drives estrogen synthesis and release in the ovary and also provides the hormonal signal needed for ovulation. Following ovulation, LH and later hCG, via the LH receptor, maintain progesterone secretion by the corpus luteum. In males LH is important in male sexual differentiation during prenatal development and for production of testosterone by the testes [92].

Both LH and hCG are members of the glycoprotein hormone family together with follicle stimulating hormone (FSH) and thyroid stimulating hormone (TSH) [93]. Glycoprotein hormones are heavily glycosylated heterodimers consisting of a common α-subunit which is species specific and a β-subunit which varies for LH, TSH, FSH and hCG. The hormone subunits interact non-covalently through hydrophobic and ionic interactions.

The amino acid sequences of LH and hCG are highly conserved. These hormones share 82% homology and have 92 amino acids encoded by a single gene. The β subunit of hCG has 145 amino acids while that of LH has 117 amino acids. Compared with LH, hCG has a longer circulating half-life and higher biopotency which is due to the additional 29-amino acid C-terminal extension on hCG. hCG is the only glycoprotein hormone that contains four O-linked carbohydrate sites on the β-subunit and 30-35% of hCG's molecular weight is attributed to

carbohydrates [94, 95]. The N-terminal carbohydrates on LH and hCG are essential for physiological responses such as ligand-receptor interactions and intracellular signaling [96]. In addition, much of the carbohydrate contained on hCG can be removed to yield deglycosylated hCG [97] which is able to bind LH receptor but does not activate adenylyl cyclase (AC) [98]. As a non-functional hormone, deglycosylated hCG (DG-hCG), can be used to evaluate the LH receptor function.

For both hormones, wrapping of the β-subunits around the α-subunit forms a unique "seat-belt" arrangement by noncovalent interactions which is essential for interactions between the subunits and binding of glycoprotein hormones to receptors [94]. Both LH and hCG are able to bind the LH receptor with high affinity [99].

I.A.1. Expression and physiological role of LH receptor

Functional LH receptors are critical to fertility and maintain normal reproductive function in both females and males. LH receptors are found predominantly in the ovary and testes, but are also expressed in extragonadal organs in women such as the uterus and breasts [100]. The main physiological role for the LH receptor is mediating the action of LH in the follicles and corpus luteum of the ovary and in Leydig cells of the testis. In females, the LH receptor is expressed in granulosa cells and theca cells in the follicle and on luteal cells. In males, LH receptors are located in testis and regulate the development and function of Leydig cells [101]. Testicular LH receptors also play essential physiological role during fetal development. The fetal Leydig cells are stimulated by maternal hCG to synthesize testosterone, which is required for the differentiation of the external male genitalia and to help the testes descend into the scrotum. The LH receptors remain relatively inactive in boys after birth until the time of puberty. After

puberty, the testicular LH receptors respond to pituitary LH with increased testosterone synthesis which leads to the development of the secondary sex characteristics [102].

I.A.2. Structure of LH receptor

The LH receptor is a seven transmembrane domain receptor in the G protein-coupled receptors (GPCR) super family [103]. GPCRs are the largest gene family in human genome with over 1000 members. They are called "G protein-coupled receptors" because they activate G proteins to initiate intracellular cell signaling [5, 6]. GPCRs constitute the most abundant family of cell-surface proteins involved in signal transduction and are a major target for drugs [104]. About 30 to 50% of marketed drugs act directly on GPCRs or through GPCR-dependent mechanisms [105]. GPCRs share similar structures characterized by a hydrophobic serpentine region consisting of seven membrane-spanning α-helical segments which are connected by three intracellular loops and three extracellular loops. The α-helical segments are each comprised of 25-35 amino acids [106].

LH receptor consists a single polypeptide with 699 amino acids [107] which are divided into three domains (Figure 2.1). The extracellular domain is a glycosylated N-terminal section with 340 amino acid residues and contains the site for LH or hCG ligand binding [108]. The transmembrane domain contains seven α-helical transmembrane segments connected by three extracellular loops and three intracellular loops. The large intracellular domain is the C-terminal cytoplasmic tail domain which consisting of about 70 amino acids and plays a role in receptor-mediated signal transduction [109]. Both the rat LH receptor (rLHR) and the human LH receptor (hLHR) are about 80 kDa [108]. The amino acid sequence similarity between the hLHR and the

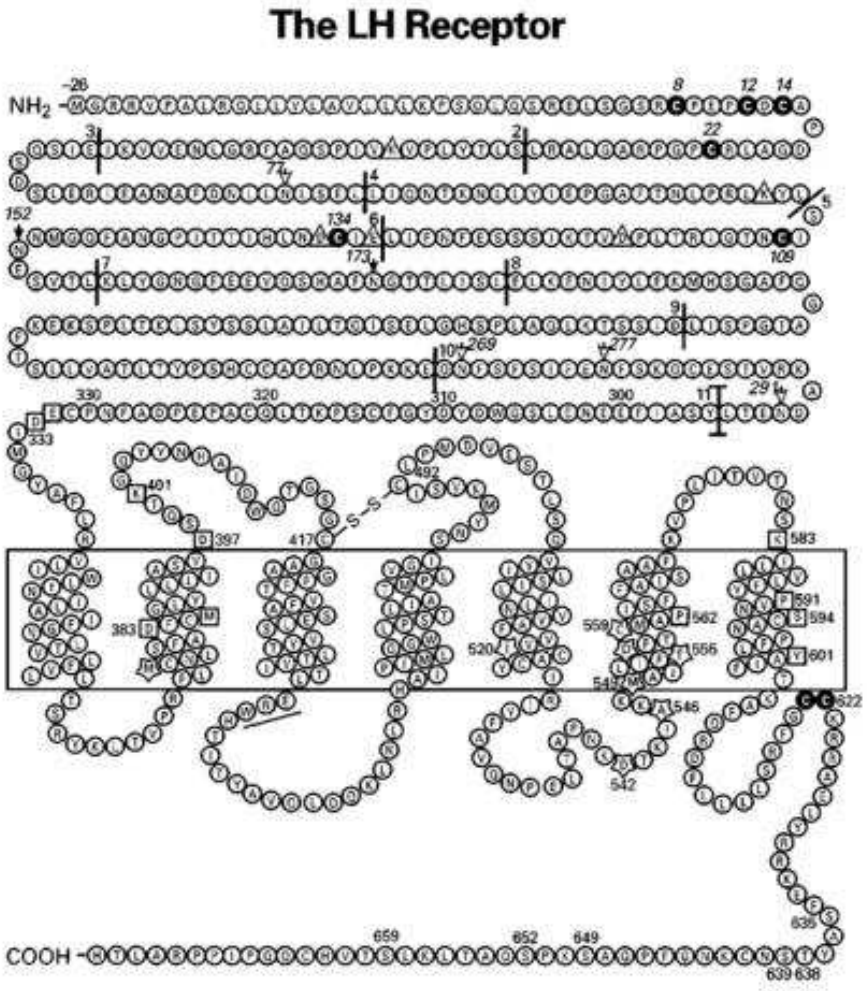

Figure 2.1: The amino acid sequence of the LH receptor. LHR consists of extracellular, transmembrane and cytoplasmic domains. The extracellular domain is heavily glycosylated and contains the single binding site for hormone. The transmembrane domain spans the phospholipid bilayer with seven segments. The intracellular C-terminal domain contains about 70% amino acids. Adapted from Dufau [103].

rLHR is approximately 88% in the extracellular domain, 92% in the seven transmembrane region and 69% in the C-terminal cytoplasmic tail [101].

I.A.3. Clinical and pathological significance of the LH receptor function

Signal transduction by LH receptors in both males and females is important for successful reproduction. Loss-of-function LH receptor mutations cause a number of diseases including Leydig cell hypoplasia [110]. Familial male-limited precocious puberty (FMPP) is caused by a genetic mutation in the LH receptor resulting in a constitutively-active LH receptor which causes early puberty in males who have high levels of testosterone and low levels of gonadotropin [111]. It has been shown that specific LH receptors can be detected in human endometrial cancer where their expression levels are related to the cancer grade [112].

I.B. cAMP

Activation of the LH receptor by binding of LH or hCG leads to an increase in intracellular levels of adenosine 3', 5'- cyclic monophosphate (cAMP; Figure 2.2), an important second messenger. cAMP plays essential roles in a large number of biological systems. As examples, cAMP is involved in regulation of glycogen metabolism, sugar metabolism, insulin secretion, lipid metabolism [113], memory formation [114], and immune function [115]. cAMP is a small molecule that can move signaling information quickly throughout the cytoplasm. Increases in cAMP result in alterations in cell metabolism or other activities via activation of different categories of effectors. Three types of cAMP effectors are cyclic nucleotide-gated channels (CNGC) [116, 117], protein kinase A (PKA) [118, 119] and an exchange protein (Epac) which is directly activated by cAMP [120]. Changes in intracellular cAMP concentrations can

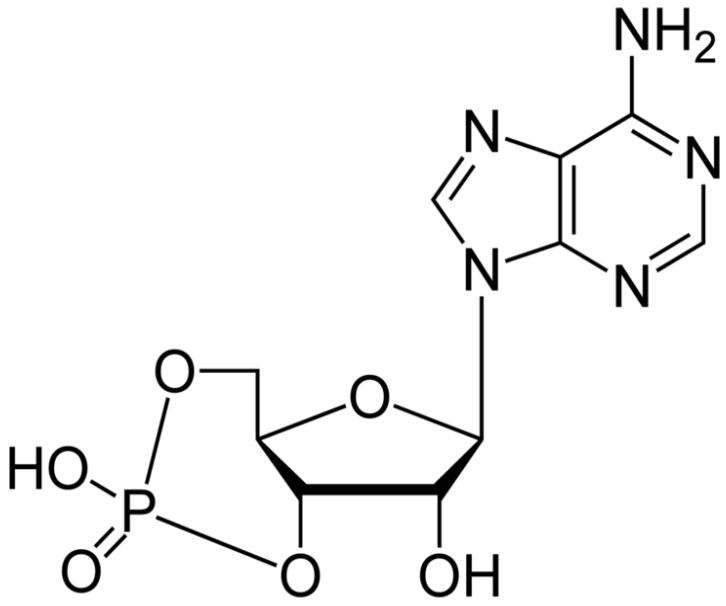

Figure 2.2: cAMP structure.

be monitored by the techniques based on CNGCs sensor sensor [121-123] and and Epac-based [124-126].

Adenylyl cyclase is a key enzyme localized at the plasma membrane that converts adenosine triphosphate (ATP) to cAMP [127]. Adenylyl cyclase releases cAMP into the cytoplasm where cAMP binds to enzymes or ion channels and stimulates downstream signaling pathways within the cell. Adenylyl cyclase can produce many molecules of cAMP, thus amplifying the signal initiated by binding of ligand to extracellular binding sites. Figure 2.3 shows the process by which cAMP is cyclized from ATP.

I.C. cAMP mediated signal transduction by LH receptor

The LH receptor binds hormone on its extracellular domain with high affinity. Activation of the LH receptor, like other GPCRs, is initiated by ligand binding which results in a change in conformation in the ligand binding domain and rotation in the transmembrane domain. The LH receptor mainly signals through the cyclic adenosine monophosphate (cAMP)/protein kinase A (PKA) pathway [103]. LH receptors transduce extracellular signals through the receptor C terminal to activate G-proteins which are heterotrimeric proteins consisting of α, γ and β subunits [128]. LH receptors are inactive when there is no hormone bound. In the inactive state, α subunit is bound to GDP on G proteins. Activated α subunit binds guanosine triphosphate (GTP) which leads to the dissociation of both the membrane-anchored βγ subunits and α subunit from the receptor. The α-subunit then activates adenylyl cyclase, which converts ATP to cAMP, thus increasing intracellular cAMP. The increase in cAMP is translated to cellular responses by the cAMP effector protein kinase A (PKA). Reversely, hydrolysis of GTP to GDP terminates the activity of G_{α} which is followed by its reassociation with $G_{\beta\gamma}$. There are

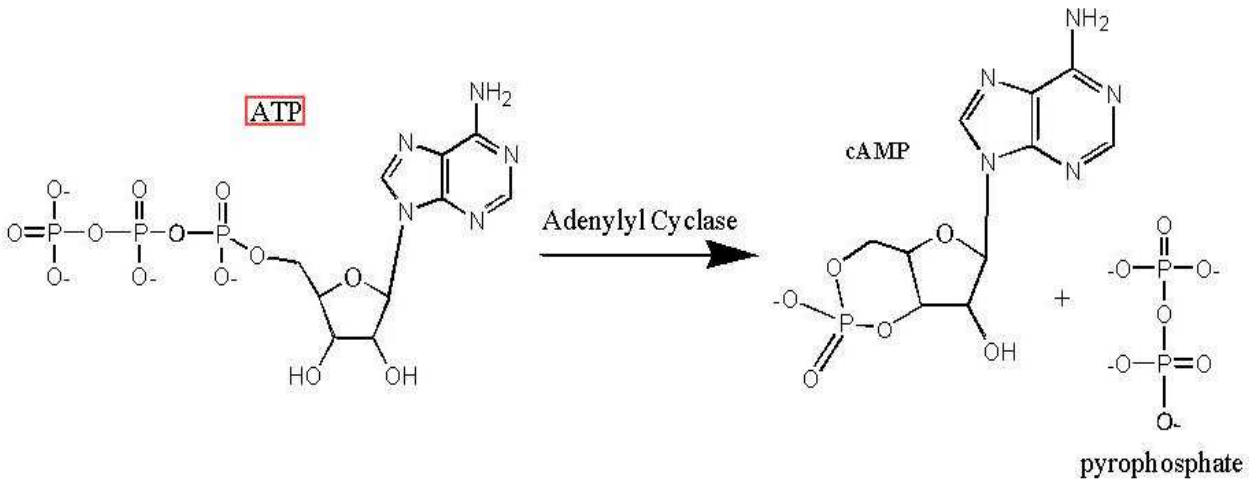

Figure 2.3: The reaction catalyzed by adenylyl cyclase that results in formation of cAMP from ATP.

both inhibitory and stimulatory G proteins which means, in practice, that activation of G proteins can either increase or decrease production of cAMP [103]. Figure 2.4 shows signal transduction through cAMP/PKA pathway by LH receptor which uses a stimulatory G protein.

At higher concentrations, LH or hCG can also activate phospholipase C via cAMP. The LH receptor was one of the first GPCRs shown to independently activate two G protein-dependent signaling pathways [129]. In addition, Salvador et al. demonstrated that in granulosa cells derived from pre-ovulatory follicles, the activation of LH receptor by hCG induced a cellular response that was predominantly mediated by protein kinase A and independent of PKC [130]. By means of these and other signal pathways, binding of the hormone to LH receptors produce necessary physiological responses [131].

I.D. Oligomerization of GPCRs

GPCRs were initially considered to be monomeric entities activating G proteins with 1:1 stoichiometry [132, 133]. However, there is evidence that many GPCRs may exist as dimers or higher-ordered oligomers [134-136]. Agnati and coworker first hypothesized the functional significance of receptor clusters by receptor-receptor interactions in 1982 that the clusters of receptors were capable of interacting [137]. A wide range of GPCRs were then shown to function not only as monomers but also as heteromers [138-141].

The oligomerization of GPCRs may be important for receptor expression and function although the functional significance of oligomerization process is still not completely understood. [142, 143] In addition, it is unclear whether GPCRs form higher-ordered clusters after ligand binding. For example, LH receptors become self-associated when activated by hCG binding [144] but the distribution of monomers, dimers and higher oligomers and the relationship of

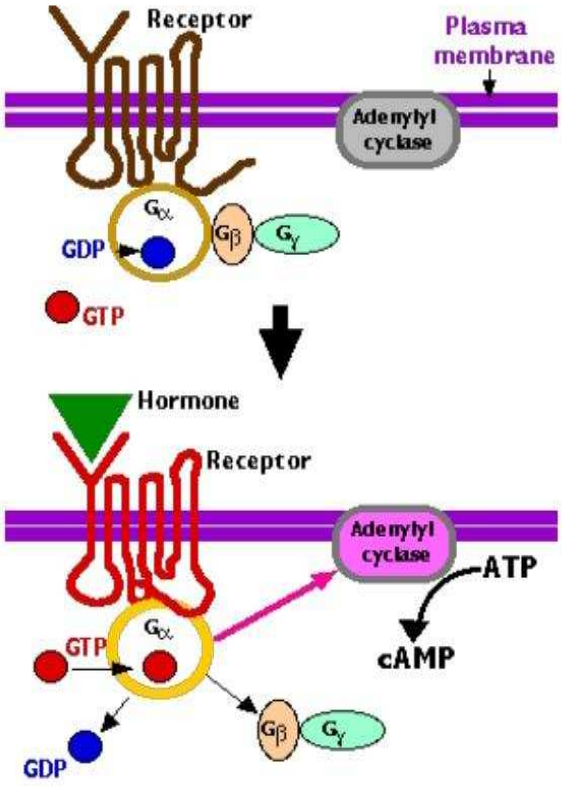

Figure 2.4: The cAMP/PKA pathway used by LH receptor. Gα has GDP in its binding site. LH receptor tertiary structure changes when a hormone binds to the ligand binding site in the extracellular domain. This conformational change triggers an allosteric change in Gα causing GDP to leave and be replaced by GTP. GTP activates Gα which results in Gα dissociation from $G_{\beta\gamma}$. Activated Gα then activates adenylyl cyclase which catalyzes the conversion of ATP to cAMP. Activated Gα is a GTPase which converts GTP to GDP which restores the LH receptor to its inactive state.

these species to productive signaling are still unknown. The significance of GPCRs oligomerization for GPCR signal transduction mechanisms requires a reevaluation of how ligands, hormones, neurotransmitters and other pharmacological ligands act on GPCRs during ligand-mediated activation [145].

Techniques based on resonance energy transfer (RET) have been used to monitor the kinetic and dynamic properties of GPCR complexes [146]. Hetero-transfer fluorescence resonance energy transfer (FRET) and bioluminescence resonance energy transfer (BRET) have been used to study GPCR oligomerization in live cell membranes [147]. However, these techniques provide limited information on GPCRs because there is no control for the relative expression levels of the GPCR [148, 149] and receptors must be conjugated using two different probes. Homo-FRET takes place between two identical fluorophores and has proved to be very sensitive to protein aggregation. Thus homo-FRET measurements provide a way to evaluate higher oligomers [150-153] while hetero-FRET and BRET measurements cannot distinguish dimers from higher-order oligomers of membrane proteins. We will discuss FRET methods in more detail in the next section.

I.E. Macromolecular Crowding

Macromolecular crowding plays an important role in cell biology and physiology [154, 155]. Almost all biological macromolecules in *vivo* exist as functional complexes and while [156] most studies have focused on the formation of protein complexes or protein-protein interactions, molecular crowding is often overlooked. High protein concentrations in membranes tends to result in formation of nonspecific aggregates. Macromolecular crowding is very important because it can affect protein structure, folding, shape, conformational stability, binding

of small molecules, enzymatic activity, protein-protein interactions and protein-nucleic acid interactions [157]. In addition, any reaction that depends on available volume will be affected by macromolecular crowding [154, 158]. Entropy maximization of a system leads to a tendency for excluded volume minimization in crowded environments. Macromolecular crowding nonspecifically enhances reactions reducing excluded volume or surface area [159]. These reactions include the formation of protein clusters, binding of proteins to surface sites, formation of aggregates, and compaction or folding of proteins. Crowding effects strongly depend upon the relative sizes and shapes of crowding species and dilute macromolecular reactants and products [160]. The hydrodynamic volume of a protein or changes in its oligomerization/association state can minimize the excluded volume.

The function of proteins can change in different way because of crowding effects. For some membrane proteins, the formation of high order oligomers and aggregates will occur more readily in the crowded environments [161]. The system will minimize the overall crowding by enhancing association of molecules, therefore reducing the excluded volume [161]. Many protein functions depend on their oligomeric state and will be affected by enhanced oligomerization in crowded environments. Therefore, it is essential to consider the possible influences of crowding when evaluating the organization of proteins like LH receptors that undergo oligomerization and aggregation.

I.F. Fluorescence Resonance Energy Transfer (FRET)

FRET has become a popular tool to measure the aggregation state and dynamics of biological molecules within biological environments [99, 162-170]. FRET methods can be also used for studies of protein-protein interactions as well as of intramolecular conformational

changes. Fluorescence resonance energy transfer was described by Jean Perrin in 1926 [171] and developed by Theodor Förster who in 1948 proposed a theory for better understanding FRET [172]. FRET is a physical process by which an excited donor transfers energy to a nearby acceptor through a non-radiative process. This process requires a significant overlap of the donor emission spectrum and the acceptor absorption spectrum and is distance-dependent. The transfer process is effective only when the distance separating the donor-acceptor pair is less than 10 nanometers (Figure 2.5).

FRET is based on dipole–dipole interactions between the transition dipoles of the donor (Figure 2.6). Donor and acceptor transition dipole orientations must be approximately parallel. Energy transfer efficiency depends on the relative orientation and separation between the two transition dipoles as well as on the overlap between donor emission and acceptor absorption spectra. The transfer efficiency (E) varies inversely as the sixth power of the distance between the donor and acceptor as

$$E = \frac{1}{[1+(r/r_0)^6]} \tag{2.1}$$

where r_0 is the distance where FRET efficiency is 50%

I.F.1. Hetero-FRET

Hetero-FRET refers to FRET between two different fluorescent proteins such as cyan fluorescent protein (CFP) and yellow fluorescent protein (YFP), color variants of green fluorescent protein found in the jellyfish *Aequoria Victoria* [173]. To evaluate protein interactions, CFP and YFP are a good pair since excitation of CFP at 430 nm does not directly

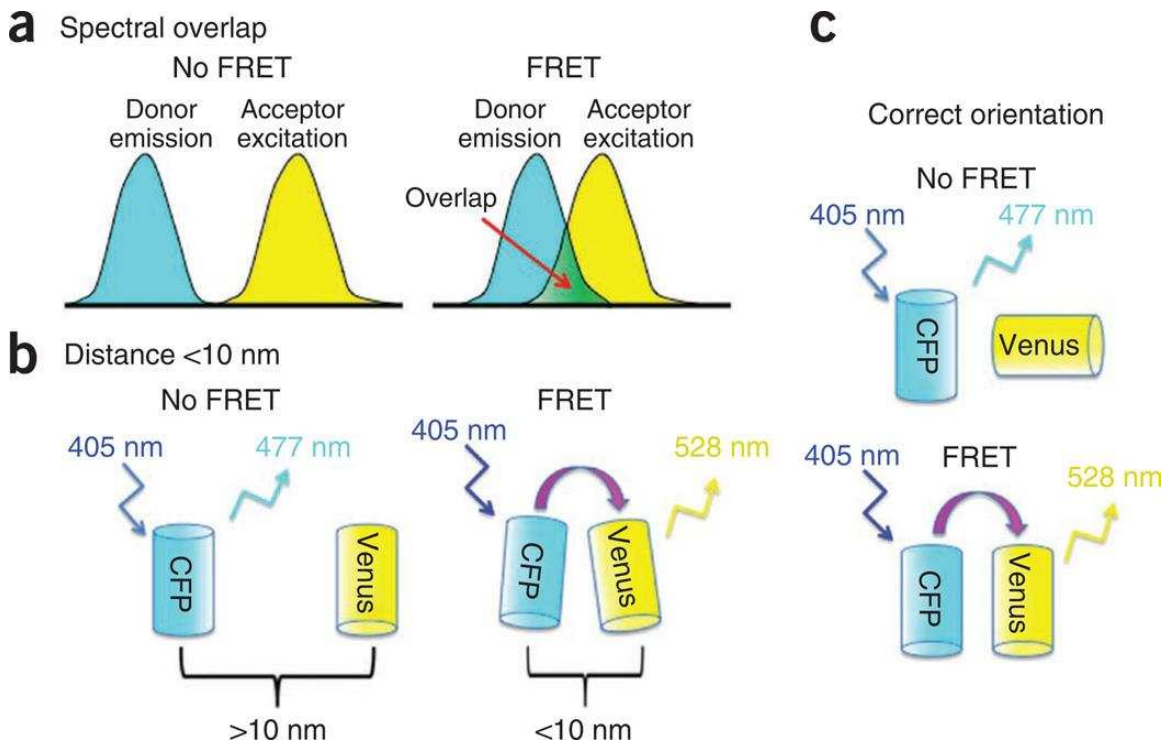

Figure 2.5: Diagrams indicating the three conditions that must be met for FRET. (a). The emission spectrum of the donor fluorophore must overlap with the excitation spectrum of the acceptor fluorophore. (b). The donor and acceptor must be within ~10 nm of one another for energy transfer can from the donor to the acceptor to occur. (c). The dipoles must be parallel to each other for FRET to occur. Adapted from Broussard [174].

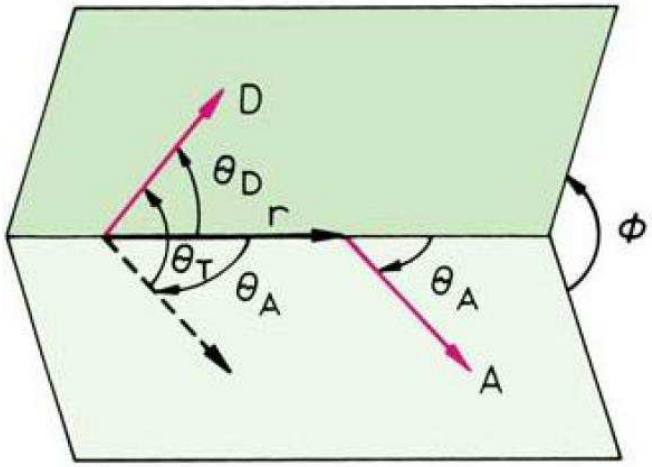

Figure 2.6: Orientation of emission dipole of the donor with respect to the absorption dipole of the acceptor. θ_T is the angle between donor and acceptor transition dipole moments and θ_A and θ_D are the angles between the separation vector, r and the acceptor and donor transition dipoles, respectively. Adapted from Lakowicz [175].

excite YFP [176-178]. This method has also be used extensively to study GPCR activation, second messenger propagation and ligand binding in vivo [179].

I.F.2. Homo-FRET

Homo-FRET occurs when energy is transferred between two members of the same fluorophore as, for example, between two YFP fluorophores [180]. Gregorio Weber examined FRET effects on polarization fluorescence, work which led to the technique now termed homo-transfer FRET [181]. Two of the same fluorophores which emit light with the same wavelengths can serve as both the donor and the acceptor. FRET between these two molecules is studied using methods based on fluorescence anisotropy because there are no spectral differences between donor and acceptor fluorophores [182]. Anisotropy is the difference in polarization between the excitation and emission of the fluorophore. Fluorescence emission anisotropy is measured by exciting fluorophores by plane-polarized light and recording from emitted fluorescence intensities $I_{\parallel}$ and $I_{\perp}$ polarized parallel and perpendicular with respect to exciting light polarization determined by the polarizer in the excitation light path [35]. Fluorescence emission anisotropy, r, is defined as

$$r = \frac{I_{||} - I_{\perp}}{I_{||} + 2I_{\perp}} \tag{2.2}$$

Different detection efficiencies are introduced into the measurements where collecting $I_{\parallel}$ and $I_{\perp}$ in different channels. A correction factor called the g-factor (g) is used in anisotropy calculations [36] and is defined as

$$g = \frac{I_{VV}}{I_{VH}} \tag{2.3}$$

where I_{VV} and I_{VH} are the fluorescence intensities observed for excitation and emission polarizers both oriented vertically and horizontally with respect to the laboratory axis, respectively. Then, r becomes

$$r = \frac{I_{||} - gI_{\perp}}{I_{||} + 2gI_{\perp}} \tag{2.4}$$

In the absence of energy transfer, the excited molecule emits with a polarization reflecting orientation of the donor molecule. If energy transfer occurs between molecules, the acceptor emits polarized fluorescence because of energy transfer from the donor. Thus homo-transfer FRET leads to a decrease in fluorescence anisotropy because the emission dipoles are more extensively randomized with respect to the polarization of exciting light. The acceptor molecule is thereby orientated freely in the presence of FRET [180]. Fluorescence polarization is shown in Figure 2.7.

Homo-FRET studies have been used to study the oligomerization states of membrane receptors. Such studies elucidate the complex association states of molecules and how they relate to biological functions [183]. Anisotropy values are directly responding to the state of receptor aggregation. If the anisotropy increases, the self-association decreases suggesting that a monomeric receptor exists. If anisotropy decreases then the receptor self-association has increased which suggests that the observed receptors exist as dimeric or oligomeric structures [108].

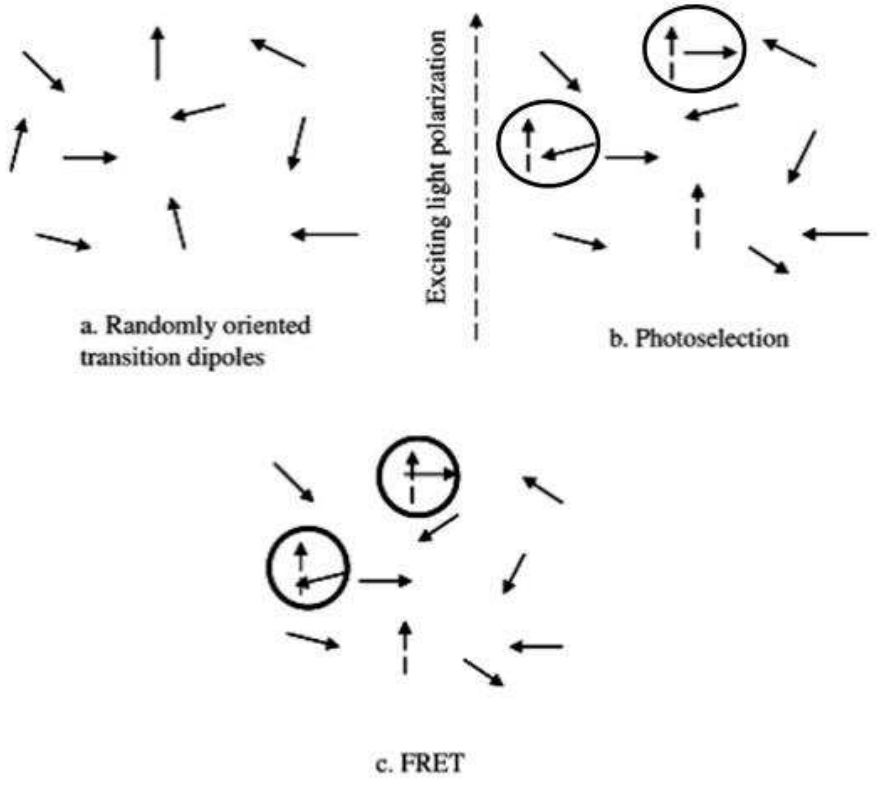

Figure 2.7: Polarization of fluorescence. a. Fluorophores with randomly-oriented transition dipoles. b. When shining polarized light on fluorophores, a subset of the fluorophores oriented parallel to the polarization of the exciting light are excited via photoselection. c. These excited donor fluorophores transfer energy to nearby acceptor fluorophores which subsequently emit partially depolarized fluorescence.

I.G. Techniques for FRET measurements

I.G.1. Acceptor photobleaching.

There a number of instrumental methods that can be used to study FRET in microscope-based systems [145]. Acceptor photobleaching is a method that can be used to image FRET between donor and acceptor. The donor and acceptor are imaged individually before photobleaching of the acceptor. After photobleaching, donor and acceptor are imaged again and donor fluorescence intensity D before and after photobleaching is compared. If FRET is occurring, donor fluorescence will increase with photobleaching of the acceptor [184]. Acceptor photobleaching also needs to be conducted using a negative FRET control sample as a control to ensure that no increase in donor fluorescence is observed. Energy transfer efficiency (%E) can be quantified as

$$\%E = [(D_{after} - D_{before}) / D_{after}] \times 100 \quad (2.5)$$

I.G.2. Emission ratio imaging.

Emission ratio imaging is a technique based on measuring FRET from a sample and from negative controls. Images of the donor and the FRET signal are taken and corrected for background intensity. The results are then presented as an emission ratio of donor emission/FRET. As the donor/FRET increases, the FRET emission signal decreases. Emission ratio imaging method is most commonly used for live cell microscope because the image collection is fast. Two fluorescence cubes are used in the wide-field microscope with a cube wheel. The donor cube contains a donor excitation filter, a dichroic mirror for donor excitation and a donor emission filter. The FRET cube contains a donor excitation filter, a dichroic mirror for donor excitation and an acceptor emission filter.

I.G.3. Spectral imaging.

Spectral imaging is a combination of spectroscopy and imaging methodologies. Imaging provides the intensity at every pixel of the image, and a typical spectrometer provides a single spectrum. Spectral imaging method collects images of donor and FRET during the entire fluorescence emission spectrum compromising on the number of points in the spectrum instead of collecting separate donor and FRET images using band-pass filters [185].

I.G.4. Fluorescence anisotropy–based FRET.

The fluorescence anisotropy–based FRET is similar to the method used to evaluate fluorescence anisotropy in homo-transfer FRET measurements. If the donor is excited and emits fluorescence directly, the polarity does not change. If the donor transfer its energy to an acceptor there is a change in polarity and a decrease in anisotropy [186]. The anisotropy equation is used for hetero-transfer FRET in the same as the equation 2.4 for homo-transfer FRET

$$r = \frac{I_{||} - gI_{\perp}}{I_{||} + 2gI_{\perp}} \tag{2.4}$$

$I_{||}$ is the donor emission light parallel to the excitation light, and $I_{\perp}$ is the donor emission light perpendicular to the incident polarized light. Lower anisotropy indicates more FRET.

I.G.5. Fluorescence lifetime imaging microscopy (FLIM).

FLIM is an imaging technique which collects an image based on the fluorophore lifetime spatially distributed in different locations across the sample [187]. The fluorescence lifetime is the average time which a molecule spends in the excited state before giving off a fluorescence photon and returning to the ground state. This lifetime is very sensitive to refractive index of the

medium [188], pH [189] and the presence of a fluorescent acceptor. FLIM only measures the lifetime of the donor fluorophore. Time-correlated single-photon counting (TCSPC) is generally used to measure fluorescence lifetimes. Details about TCSPC have been included in Chapter I. Percent energy transfer efficiency (E) is calculated using

$$E = [1 - (\frac{\tau_{AD}}{\tau_D})] \times 100 \quad (2.6)$$

where τ_D is the fluorescence lifetime of the donor in the absence of the acceptor. τ_{AD} is the florescence lifetime of the donor in the presence of the acceptor. The advantage of FLIM is that it is relatively independent of fluorescence intensity, the concentration of acceptor and donor, and is less sensitive to fluorophore bleaching. Both hetero-FRET and homo-FRET can be detected using lifetime measurements.

I.H. Biophysical techniques for detection of cAMP

As an important second messenger, cAMP regulates a number of cell functions. A variety of biophysical techniques and biosensors have been developed in last few decades to examine cAMP levels in viable cells.

I.H.1. Biochemical methods

Radioimmunoassays (RIAs) use immobilized anti-cAMP antibodies and ^{125}I-labeled cAMP as a tracer molecule to measure quantitatively cAMP concentration in cells and tissues [190] . The ^{125}I-labeled cAMP binds to anti-cAMP antibodies, and a radioactive signal from ^{125}I-labeled cAMP can be detected. Increased cAMP results in competitive binding to anti-cAMP

antibodies. Enzyme-linked immunoassays are one of non-radioactive approaches to measure cAMP in vitro.

I.H.2. FRET based sensors

These FRET-based sensors include protein kinase A (PKA)-based cAMP sensors and Epac-based cAMP sensors. Adams and coworkers developed the first approach to measure intracellular cAMP signals by a FRET technique. They labeled or regulatory (R) or catalytic (C) subunits of PKA with a FRET probe i.e. a fluorescein-labeled PKA catalytic subunit, and a rhodamine-labeled regulatory subunit (FICRhR), to allow energy transfer between these fluorophores in the PKA holoenzyme complex R2C2 [191]. This probe has been used to study cAMP dynamics in neurons or lobster ganglions and to analyze the interactions of cAMP and Ca^{2+} oscillations in embryonic spinal neurons [192, 193]. Zaccolo et al. fused the blue fluorescent proteins BFP and GFP to the PKA RII and C subunits, respectively to develop a genetically-encoded cAMP FRET probe. This probe was able to measure real-time cAMP dynamics in various cell types after co-transfection of cells with the two plasmids encoding for the labeled subunits [194].

In addition to measuring cAMP levels directly by FRET-based cAMP biosensors, the dynamics of signaling can be further investigated by looking at the catalytic activity of the PKA. Epac is an exchange protein directly activated by cAMP. The multi-domain structure of Epac1 and Epac 2 is shown in Figure 2.8. Epac1-cAMP and Epac2-cAMP sensors were developed by Nikolaev and coworkers. In an Epac1-cAMP sensor, the cAMP binding domain of the Epac1 protein (Epac1157−316) was flanked by an N-terminal CFP and a C-terminal YFP. Epac2-cAMP sensors used the cAMP binding domain B from Epac2 (Epac2B 284−443) instead. cAMP

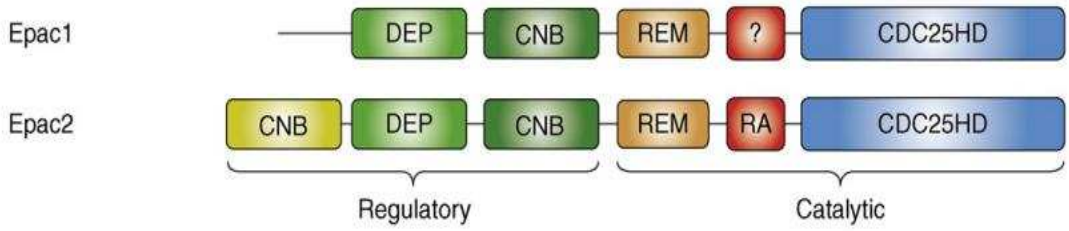

Figure 2.8: The multi domain structure of Epac. The domain structure of Epac1 and Epac2 show the regulatory region with the cyclic nucleotide-binding domain(s) (CNB) and the catalytic region with the CDC25-homology domain (CDC25HD) responsible for the guanine-nucleotide-exchange activity. The Desheveled-Egl-10-Pleckstrin (DEP) domain is involved in membrane localization, the Ras exchange motif (REM) stabilizes the catalytic helix of CDC25HD and the Ras-association (RA) domain is a protein interaction motif. The question mark in Epac1 is a region with homology to the RA domain in Epac2 with unknown function. Adapted from Johannes, 2006 [195].

binding to Epac induced a conformational change within the sensor and both biosensors generated an increase in the cyan to yellow emission ratio upon binding cAMP, indicating a decrease in FRET [103]. Compared to the tetrameric PKA sensor, Epac2-cAMP sensors showed faster kinetics and larger FRET ratio changes which is why Epac2-cAMP has been used in many other studies. Ponsioen *et al.* created a cAMP FRET probe using the full or partial length Epac1 fused to CFP and YFP [123]. The CFP-Epac-YFP had an extended dynamic range improved signal-to-noise compared to the PKA probes [101].

J. Zhang and coworkers have developed several Epac-based reporters called ICUE probes by using either the full length Epac1 or truncated Epac2 sandwiched between ECFP and a citrine YFP variant [125]. ICUE1 contained full-length Epac1. Like Epac1 and Epac2-cAMP probes, ICUE also responded to increased cAMP with an increase in the cyan to yellow emission ratio. Violin et al. developed an improved version of the ICUE1 cAMP biosensor which contained a truncated Epac1 protein, ICUE2, and showed larger FRET signals with minimal effects on cellular functions [196]. This biosensor had improved localization over ICUE1 due to removal of a membrane and mitochondrial targeting sequence located at the N-terminus. More recently, Zhang and coworkers have developed ICUE3 (Figure 2.9) by replacing citrine with a circularly permuted YFP, cpVenus L194, to form a cAMP reporter [197]. Circular permutation introduces new N and C termini to a protein and can improve the dynamic range of FRET-based reporters by altering the relative orientation of fluorescent proteins [198]. Upon stimulation with cAMP elevating agents such as forskolin, the FRET signal from the sensor decreased due to conformational changes (Figure 2.10).

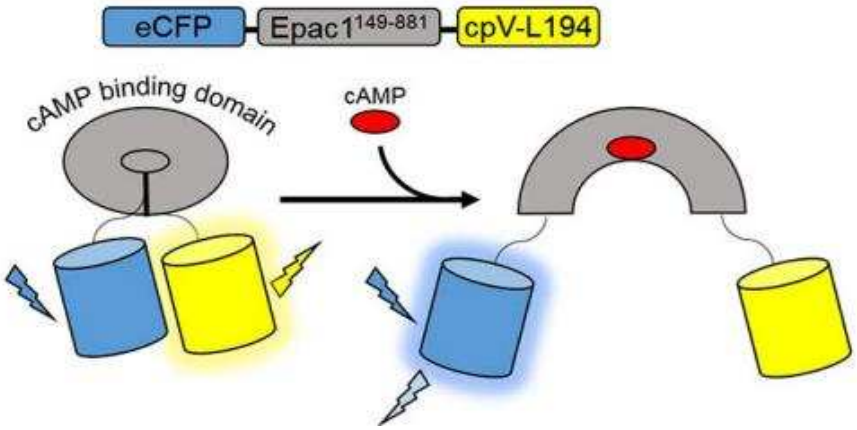

Figure 2.9: ICUE3 consists of an Epac1 149−881 sensing unit flanked by an ECFP donor and a cpV-L194 acceptor reporting unit. Upon binding cAMP, the sensor switches from a high FRET to a low FRET conformation. Adaped from Gorshkov et al., 2014 [199].

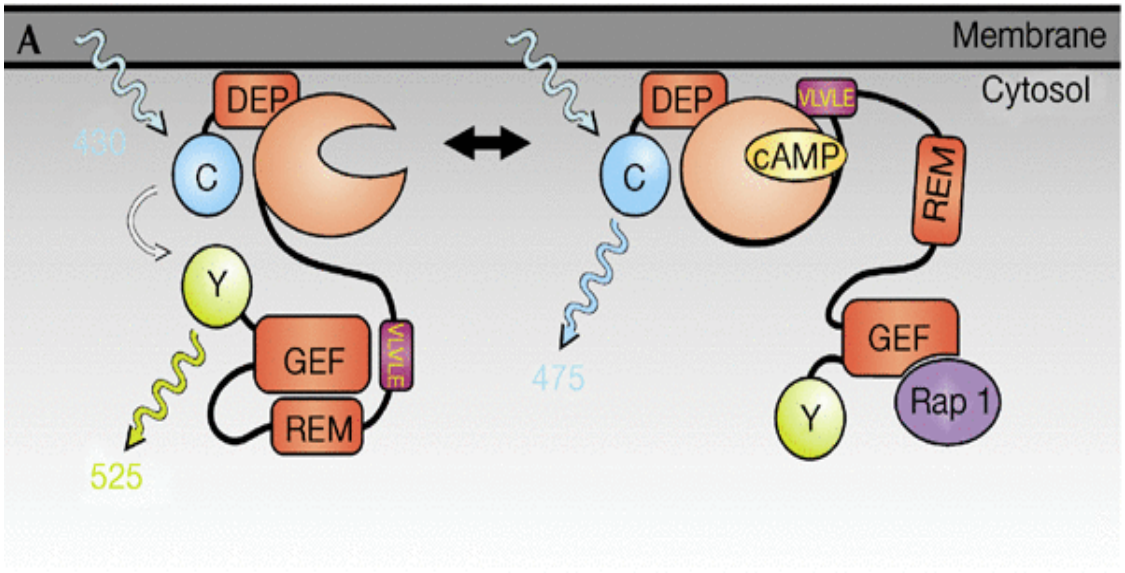

Figure 2.10: Model for the conformational change following binding of cAMP to the regulatory domain of Epac. Following cAMP binding, the VLVLE sequence can interact with the regulatory domain, releasing the inhibition of the GEF domain by the REM domain. FRET between the CFP and YFP tags allows detection of this conformational change. Adapted from Bos, 2003 [200].

I.H.3. Bioluminescence resonance energy transfer (BRET)-based sensors

BRET is non-radiative energy transfer between a bioluminescent enzyme donor and a fluorophore acceptor. The donor enzyme usually is a variant of the Renilla reniformis luciferase (Rluc). Coelenterazine is used as a substrate and GFP variants are usually used as acceptor fluorophores [201]. Like FRET methods donor and acceptor molecules need to be in close proximity, less than 10 nm [202], to enable energy transfer and the detection of the fluorescent signal. The BRET signal is calculated from the ratio of the donor and the acceptor emissions.

Prinz and coworkers created the first BRET cAMP biosensor based on PKA [203]. They fused Rluc to the regulatory RI and RII subunit, creating two different donor proteins for the BRET system. BRET signal decreases with increasing intracellular cAMP concentrations because PKA regulatory and catalytic subunits dissociate upon cAMP binding. In addition, Jiang and coworkers created the first BRET sensors based on the Epac protein. They used a cytosolic mutant form of the human Epac1 protein and fused it to Rluc and the YFP variant Citrine (YFP-Epac-RLuc). The sensor had a strong BRET signal under basal conditions and was improved by using a circularly permuted version of citrine in the sensor [204]. Barak et al. created the second Epac-based BRET sensor for cAMP detection by fusing Rluc and citrine to the cAMP binding domain from Epac. They evaluated the activity of trace amine-associated receptor 1 (TAAR1) ligands by expressing the sensor in HEK 293 cells [205].

II. RESEARCH GOALS

As an important second messenger, cAMP regulates cellular functions with high specificity and efficiency. Levels of cAMP during LH signaling are used to assess the function

of this G protein-coupled receptor. cAMP levels have been studied using techniques including biochemical methods, FRET-based sensors and BRET-based sensors. One goal of this project was to evaluate hLH receptor function by measuring cAMP levels in CHO cells expressing either wild type or transient transfected hLHR-mCherry using the FRET-based cAMP reporter ICUE3. ICUE3 undergoes a conformational change upon binding cAMP that reduces FRET between the fluorescent donor and acceptor. In initial studies FRET was performed using a dual emission ratio (CFP/YFP) imaging method to measure cAMP levels in viable cells.

A second goal was to examine whether expression levels of LH receptors affected cell signaling using flow cytometry together with a cAMP reporter (ICUE3). We have demonstrated that LH receptors become aggregated upon binding hCG when receptors are expressed at physiological numbers [163]. Nonetheless, there are reports that LH receptors are aggregated [206, 207] in the absence of ligand, a result that appears to result from high molecular density which favors LH receptors aggregation regardless of experimental conditions [208]. In addition, there is some evidence that aggregation of LH receptors results in constitutive receptor activation in the absence of hormone. Flow cytometric energy transfer measurements offer superior statistics in comparison with the microscopy-based discussed in this chapter. These studies evaluated expression levels of hLHR-mCherry and related receptor number to basal levels of cAMP and cAMP levels following hormone treatment.

III. MATERIALS AND METHODS

III.A. Materials

Chinese Hamster Ovary (CHO) cells were purchased from American Type Culture Collection (Manassas, VA). Dulbecco's Modified Eagle medium (DMEM) was purchased from Corning Cellgro (Visalia, CA). Penicilin/streptomycin and L-glutamine solution were purchased from Gemini Bio-Produucts (West Sacramento, CA). FBS was purchased from Atlas Biologicals (Fort Collins, CO). 100 x MEM non-essential amino acid solution, bovine albumin and ethylenediamine tetraacetic acid (EDTA) were purchased from Sigma-Aldrich (St. Louis, MO). Cyclic adenosine monophosphate (cAMP) and saponin were also purchased from Sigma-Aldrich (Milwaukee, WI). Human chorionic gonadotropin (hCG) was purchased from Fitzgerald Industries (Acton, MA). Forskolin (Fsk) was purchased from Enzo Life Sciences (New York, NY). Lipofectamine 3000 regent and OPTI-MEM reduced serum medium were purchased from Life Technologies (Carlsbad, CA). Quantum R-PE and FITC MESF (molecules of equivalent soluble fluorophore) beads were purchased from Bangs Laboratories (Fishers, IN). Glass bottom cell culture dishes with 35mm diameter and 14mm diameter glass bottoms were purchased from In Vitro Scientific (Sunnyvale, CA).

III.B. Cell culture and transfection

Chinese Hamster Ovary (CHO) cells were grown in a 25cm^2 culture flask in DMEM medium supplemented with 10% FBS, 2mM L-glutamine, 1% penicillin/streptomycin and 1% 1x MEM non-essential amino acid solution. All cells were maintained in 5% CO_2 at 37°C in a humidified environment. Before transfection, cells were incubated with 5mM EDTA for 5 min

and 1.5mL cells were plated in a 35mm glass bottom petri dish. Cells grew to approximately 80%-90% confluence in about two days.

III.C. ICUE3 and hLH receptor transfection

CHO cells were transiently transfected with 0.4 μg of cAMP level reporter ICUE3 plasmid kindly provided by Dr. Jin Zhang (Johns Hopkins University, Baltimore, USA) using Lipofectamine 3000 in accordance with the manufacturer's instructions. Two sterilized microcentrifuge tubes were needed, each containing 125μL of OPTI-MEM medium. Tube 1 contained 0.4 μg of ICUE3 and 5μL LP3000. Tube 2 contained 7.5μL of Lipofectamine 3000. Tube 1 was added drop wise to tube 2. The mixture was incubated at room temperature for 5 minutes and then was added to the cells in 35 mm petri dish containing 1mL OPTI-MEM reduced serum medium. Transfection proceeded for at least 12 hours. All cells were maintained in a humidified incubator in 5% CO_2 at 37ºC. Representative images demonstrating expression of ICUE3 are shown in Figure 2.11.

CHO cells were transiently co-transfected with 0.4 μg ICUE3 and 1.9 μg hLHR-mCherry kindly prepared by Dr. Xiaorong Li (Southwest University, Chongqing, China). Co-transfection procedures were similar to those used to transfect CHO cells with ICUE3 above. An image showing co-localization of ICUE3 and LHR-mCherry in CHO cell plasma membranes is presented in Figure 2.12.

III.D. Dual emission wavelength ratio imaging

After cells were transiently transfected with ICUE3 or ICUE3 and LHR-mCherry, medium was aspirated from the petri dish, cells were washed twice gently and maintained in 1x

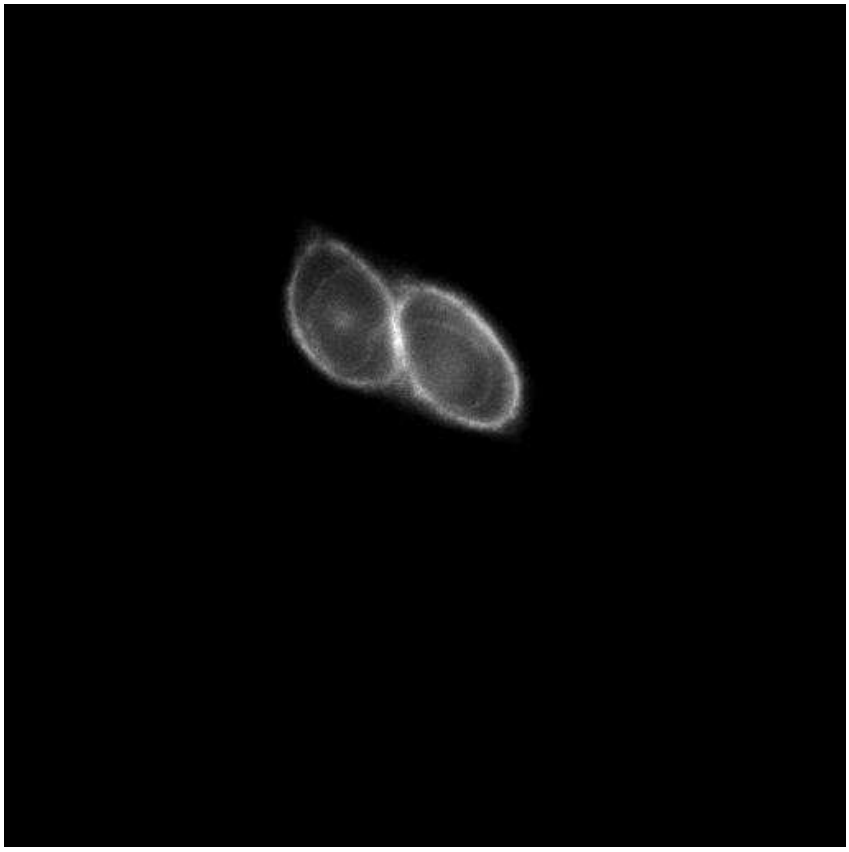

Figure 2.11: CFP Image of ICUE3 transfected CHO cells. CFP and YFP images were taken by using a 1.2 N.A. 63x water objective in a Zeiss Axiovert 200M inverted microscope with an EMCCD camera controlled by METAFLUOR software. A 436DF20 excitation filter, a 455 DRLP dichroic mirror, and two emission filters were used 480DF40 for CFP, 535DF30 for YFP.

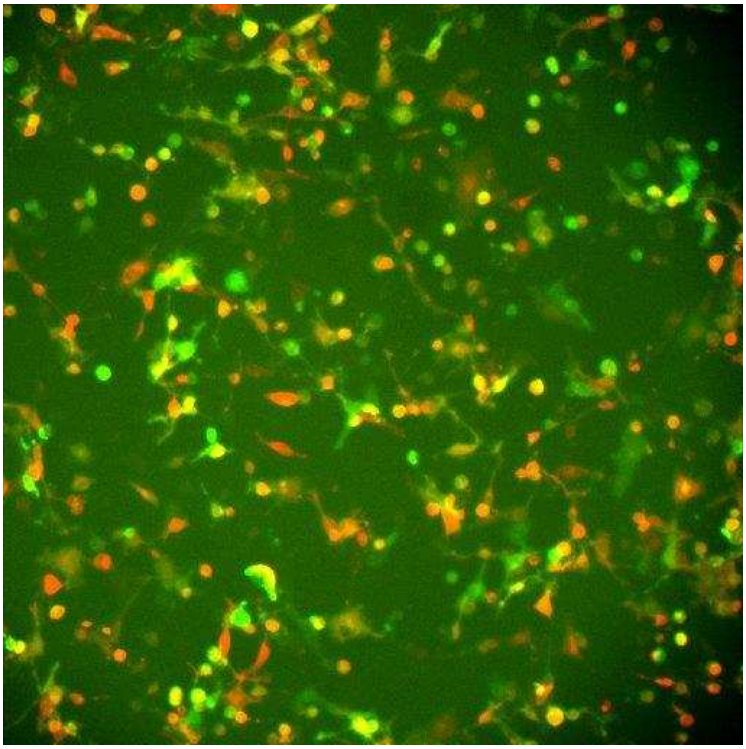

Figure 2.12: Co-localization RGB image of ICUE3 and LHR-mCherry in CHO cell plasma membrane. The green cells only have ICUE3. The red cells only have hLHR-mCherry. The orange cells have both ICUE3 and hLHR-mCherry.

phosphate buffered saline (PBS) pH 7.4 containing 0.1% BSA. Cells were then immediately imaged using procedures described below.

Imaging data were collected using a 1.2 N.A. 63x water objective in a Zeiss Axiovert 200M inverted microscope with an EMCCD camera controlled by MetaFluor software. The excitation and emission filters within the microscope filter wheels were rotated into place as needed. A neutral density filter was used to reduce the intensity of the arc lamp and reduce fluorophore photobleaching. Emission ratios were obtained using a 436DF20 excitation filter, a 455 DRLP dichroic mirror, and two emission filters, 480DF40 for CFP and 535DF30 for YFP. All filters were from Chroma Technology. The petri dish was secured to the stage of the microscope to minimize any movement of the dish while imaging. Images were taken with 60s time lapse during acquisition. In each experiment, a sequence of images were obtained. During experiments, data were collected from untreated cells for several minutes before the PBS solution was removed and replaced with 50μM forskolin or 10nM hCG in PBS.

All data were analyzed by Image J software. Emission ratios (CFP/YFP) were calculated according to CFP emission intensity and FRET intensity after background corrections of fluorescent images were performed by subtracting the intensity of the background from the emission intensities of fluorescent cells expressing ICUE3.

The CFP/YFP ratio of CHO cells expressing ICUE3 were also measured by treating CHO cells with different concentrations of cAMP together with 0.02% saponin in pH 7.4 PBS solution. Saponin was used to permeabilize cells because cAMP itself is not membrane permeable. A cAMP stock concentrated solution 10,000 μM was serially diluted to 1000 μM, 100 μM, 10 μM, 1.0 μM and 0.1 μM 300 μL solution and added to the 35mm glass bottom petri dish. The effect

of saponin is reversible, so saponin remained in solutions containing cAMP during the entire imaging process.

III.E. Flow cytometric emission ratio imaging

After cells were transiently transfected with ICUE3 or ICUE3 and hLHR-mCherry, medium was aspirated from 35mm petri dish. Cells were washed using 1x phosphate buffered saline (PBS), pH 7.4 after incubating with 5mM EDTA for 5 min. Cells (10^6cells/ml) were put into 5ml VWR polypropylene tubes for analysis using a Moflo Astrios EQ flow cytometer. Cells expressing ICUE3 alone were prepared for experiments using forskolin. Cells expressing ICUE3 and hLHR-mCherry were prepared for experiments using Fsk or hCG. In some studies, CHO cells expressing ICUE3 were also treated with different levels of cAMP in 0.02% saponin PBS, pH 7.4 solution.

Flow cytometry can be used to evaluate fluorescence from individual cells as they flow in a fluid stream through laser source. From cells expressing ICUE3 and hLHR-mCherry, the fluorescence intensity of CFP emission, YFP emission, YFP emission due to FRET and mCherry emission were collected. Flow cytometry experiments used a Moflo Astrios EQ flow cytometer located in Health Sciences Center at the University of Colorado. The laser and band path filters were used for fluorophores and beads are shown in Table 2.1. The optical-to-electric coupling system of the cytometer records how the cell scatters incident laser light and emits fluorescence. Light scattering occurs when a cell deflects incident laser light. Forward-scattered light (FSC) is a measurement of light off the incident laser beam in the forward direction. Side-scattered light (SSC) is a measurement of light that occurs at interface within the cell. FSC is proportional to cell size and SSC is proportional to internal complexity of the cell. Fluorescence emission

Table 2.1: Lasers and filters used in flow cytometry experiments.

Fluorophore/Bead	**Laser (nm)**	**Emission Band pass filter (nm)**
CFP	405	448/50
YFP /FITC	488	525/40
mCherry/R-PE	561	579/16

travels via a system of mirrors and optical filters direct the light to a PMT where the fluorescence is collected.

From software for the Moflo Astrios EQ flow cytometer, fluorescence signal intensities from individual cells or Quantum MESF beads were attained from a CSV spread sheet. To determine the numbers of ICUE3 molecules and hLHR receptors, Quantum MESF (molecules of equivalent soluble fluorophore) kits were used in data analysis. In a Quantum MESF kit, each bead population corresponds to the number of fluorophores molecules in solution which give a same signal as the beads. There are no bead standards for YFP or mCherry fluorophores so FITC or R-PE Quantum MESF beads were used, respectively. FITC and R-PE fluorescence signal intensities measured in cytometer were related to the signals measured for YFP (ICUE3) and hLHR-mCherry on cell surface.

The relative fluorescence signal R_B for one bead dye molecule measured in cytometer is obtained using the equation:

$$\mathrm{R_B} = \varepsilon(\lambda_{\max})\Phi \frac{a(\lambda_e)\int_{\lambda_d - w/2}^{\lambda_d + w/2} f_B d_B d\lambda}{a(\lambda_{\max})\int_0^{\infty} f_B d\lambda} \qquad (2.7)$$

where ε (λ_{max}) is the extinction coefficient for the given bead dye molecule, ϕ is fluorescence quantum yield, a(λ_e) is the absorbance for a given bead dye molecule at the excitation wavelength λ of laser, a(λ_{max}) is the maximum absorbance value, $\int_{\lambda_d - w/2}^{\lambda_d + w/2} f_B d_B d\lambda$ is the integral of multiplication of emission intensities and quantum yield between wavelength λ_d-$w_{/2}$ and λ_d+w/2 (band width of filter), and $\int_0^{\infty} f_B d\lambda$ is the total integral of emission intensities.

The equation (2.8) for the relative signal from one fluorophore R_p is similar to equation (2.7), with a change in the information relating bead dye molecules to fluorophores used in our experiment.

$$R_B = \varepsilon(\lambda_{max})\Phi \frac{a(\lambda_e)\int_{\lambda_d - w/2}^{\lambda_d + w/2} f_p d_p d\lambda}{a(\lambda_{max})\int_0^{\infty} f_p d\lambda} \tag{2.8}$$

The number of bead molecules (FITC or R-PE) N_B can be obtained from a calibration curve of intensities measured in the cytometer versus number of FITC (or R-PE) molecules and was created using Excel 2010. Figure 2.13 is the calibration curve for the Quantum FITC bead standard. Figure 2.14 is the calibration curve for the Quantum R-PE beads standard. The number of molecules on the surface of each cell is given by

$$N_p = N_B * R_B/R_p * S_P/S_B \tag{2.9}$$

where S_B is fluorescence signal for beads containing N_B dye molecules and S_P is the fluorescence of a particular cell.

IV. RESULTS AND DISCUSSION

To assess the function of LH receptors, cAMP levels in CHO cells were initially studied using a FRET-based cAMP reporter ICUE3 and a microscope-based method. CHO cells were transiently transfected with ICUE3 or ICUE3 and LHR-mCherry. The CFP image shown in Figure 2.11 demonstrates that ICUE3 is associated with the plasma membrane. Figure 2.12 shows fluorescence emission from ICUE3 and mCherry. Cells expressing only ICUE3 are green.

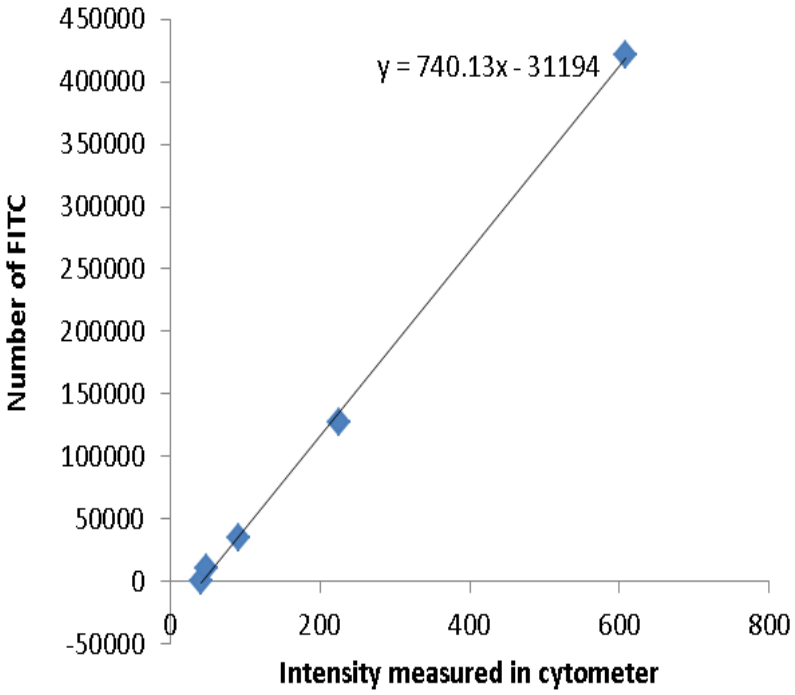

Figure 2.13: Calibration curve for Quantum FITC bead standards.

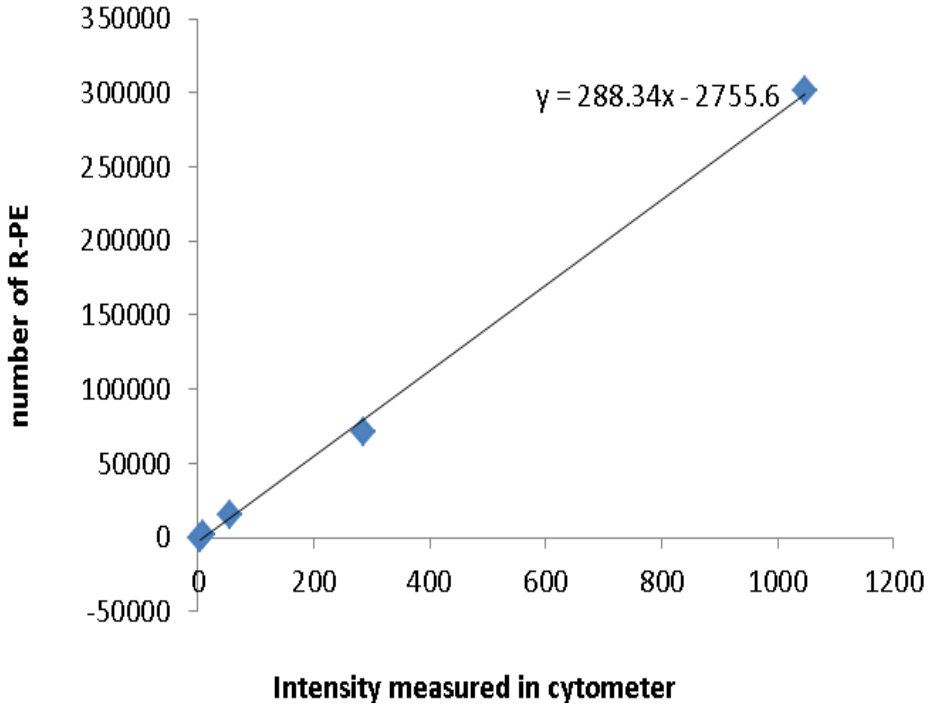

Figure 2.14 Calibration curve for Quantum R-PE bead standards.

Cells with only red fluorescence are expressing hLHR-mCherry. Orange cells have both ICUE3 and hLHR-mCherry which are co-localized in CHO cell plasma membranes.

CHO cells expressing ICUE3 were treated by varying concentration cAMP together with 0.02% saponin solution. The plot of the CFP/YFP ratio relative to the cell cAMP level is shown in Figure 2.15. There was a small increase in the ratio of CFP/YFP emission with addition of 0.1 μM, 1.0 μM and 10 μM cAMP to cells. A larger increase in the emission ratio was observed with cAMP levels from 10 μM to 100 μM. Relative to basal levels of cAMP, an 80% increase in the CFP/YFP ratio was observed when cell were incubated with 1000 μM. Thus, CHO cells expressing ICUE3 treated with different concentrations of cAMP demonstrate that CFP/YFP ratios depend on cAMP concentration, an effect which can be used to construct a standard curve relating CFP/YFP ratios to intracellular levels of cAMP.

Forskolin (Fsk) is an adenylyl cyclase activator which is produced by the Indian Coleus plant. Changes in the CFP/YFP ratio over time were monitored for CHO cells expressing ICUE3 and treated with 50μM Fsk. A representative experiment showing the time-dependent change in the CFP/YFP ratio upon treatment with 50μM Fsk is shown in Figure 2.16. Upon addition of 50μM Fsk, there was a large, comparatively rapid increase in intracellular cAMP. This suggests that Fsk activates adenylyl cyclase in these cells and causes an increase in intracellular cAMP. The maximum change in the emission ratio was observed after about 400 sec. Images were taken in 30 sec time lapse during acquisitions. The results are consistent with those for β_2-adrenergic receptor studied using an ICUE sensor [196, 197].

Changes in the CFP/YFP ratio with time were then obtained from a CHO cell expressing both hLHR-mCherry and ICUE3 and treated with 100nM hCG. The change in the CFP/YFP ratio upon addition of 100nM hCG is shown in Figure 2.17. The average CFP/YFP ratio in

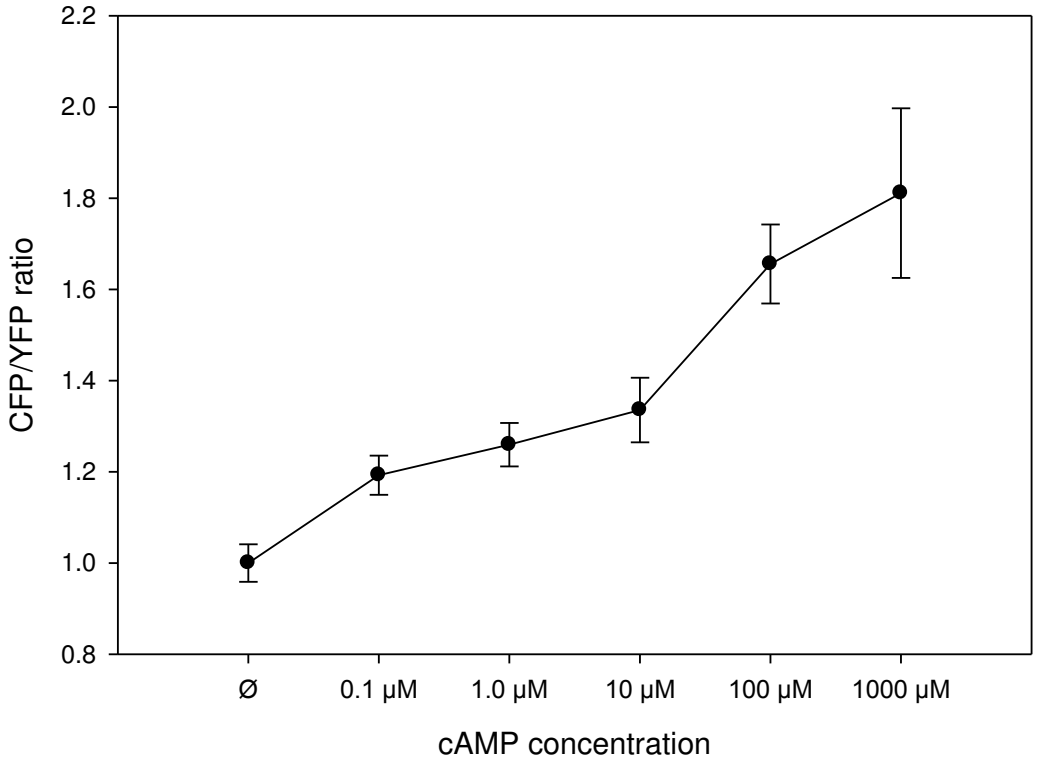

Figure 2.15: CFP/YFP ratio of CHO cells expressing ICUE3 treated by 0.1µM, 1.0µM, 10µM, 100µM and 1000 µM cAMP. Data shown are the mean ± SD (n=4).

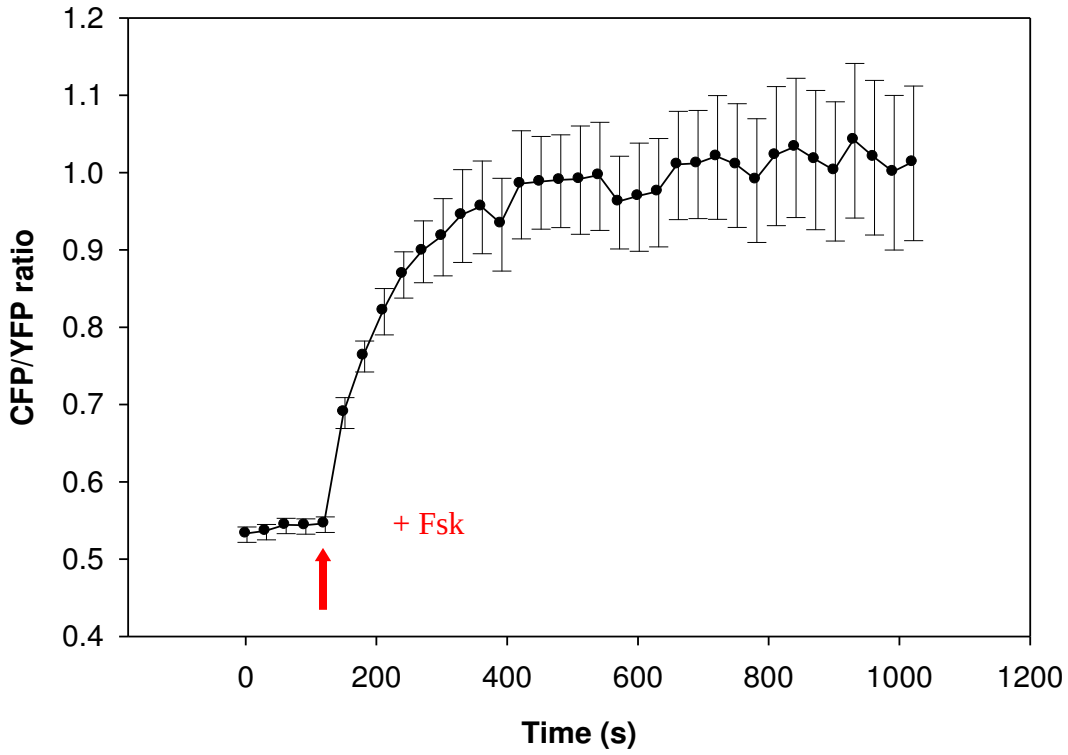

Figure 2.16: Effect of Fsk on CFP/YFP emission ratio in cells expressing ICUE3 alone. Images were taken with a 30 s time lapse during acquisitions. Data shown are the mean ± SD (n=6)

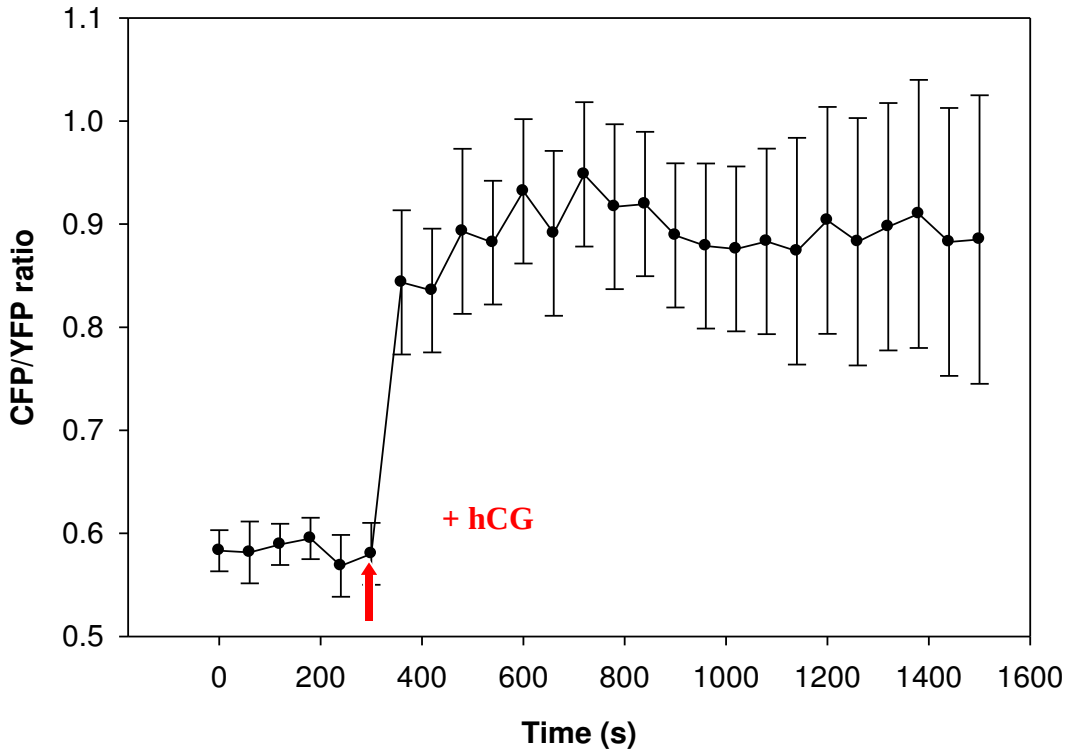

Figure 2.17: Effect of 100 nM hCG on CHO cells co-expressing ICUE3 and hLHR. CHO cells expressing both ICUE3 and hLHR-mCherry were treated with 100nM hCG at the time indicated by the arrow. hCG treatment produced a rapid increase in intracellular cAMP as indicated by increase in the ratio of CFP/YFP emission. Images were taken in 50 s time lapse during acquisitions. Data shown are the mean ± SD (n=5)

untreated cells co-expressing both hLHR-mCherry and ICUE3 is about 0.6. When CHO cells were treated with 100nM hCG, there was an increase in CFP/YFP emission ratio with a maximum change of about 50% observed within about 500 seconds after addition of hCG. This result was consistent with hCG effects on LH receptor-mediated activation of adenylate cyclase and increased intracellular levels of cAMP [209].

FRET microscopy is technically challenging and does not permit us to evaluate in large number of cells [210]. Flow cytometry-based FRET, can overcome these limitations and permit to investigate large numbers of cells expressing both cAMP reporter and LHR-mCherry. The contributions of signals from cell debris can be avoided by gating the data collection on the light scatter signal. Most important, the determination of CFP/YFP emission ratio can be carried out on a cell-by-cell basis offering data on the relationships between ICUE3 signal and other cell parameters.

Flow cytometry experiments measure fluorescence emission from cells which are expressing a fluorescent probe or receptor. All the cells are constrained in the center of a 1X PBS suspension stream and one cell at a time passes through series of laser beams to excite specific fluorophores. We showed that it was possible to plot from .csv files intensity information from individual cells, a procedure that is not typically done in flow cytometry measurements. Figure 2.18 shows a plot of forward vs. side scatter of the cell sample. The circle shape in the plots can be moved or adjusted to specific target areas for further analysis. This also permits the elimination of cell debris from subsequent data analysis.

Flow cytometry yields histograms of numbers of cells versus the logarithm of fluorescence intensity. The intensity area of transfected cells was easily seen in histogram intensities that had been gated using control cells histograms. From YFP histograms of CHO

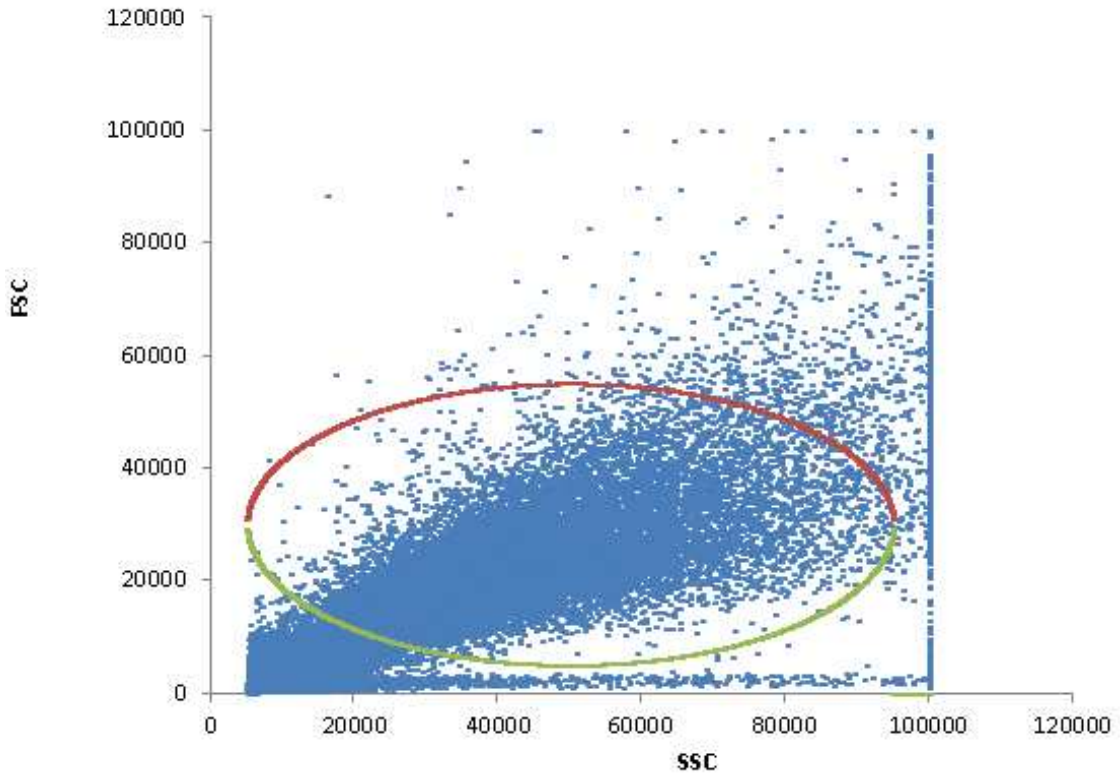

Figure 2.18: FSC vs. SSC plot of individual cells. To analyze individual cells, data files were unpacked to obtain intensity information from individual cells identified from plots of forward vs side scatter. This also permitted us to eliminate cell debris from subsequent data analysis.

expressing ICUE3 (Figure 2.19), we can see the gating area R10 obtained from control cells and that all the YFP signal from ICUE3 in transfected cells is in the gating area, R11. Figure 2.20 shows mCherry histograms of CHO cells coexpressing ICUE3 and hLHR-mCherry in the R7 area. Transiently transfected cells co-expressing LHR-mCherry and ICUE3 exhibit a broad range of LH receptor expression levels.

Calibration curves relating intensity measured via cytometer versus numbers of FITC or R-PE per bead were obtained using Quantum MESF FITC or R-PE bead standards. Using equation (2.1), (2.2) and (2.3), the number of FITC molecules can be used to evaluate YFP signals from a calibration curve (Figure 2.13) and R-PE number can be used to evaluate expression of mCherry (Figure 2.14). Although transiently transfected cells exhibit a broad range of expression levels in cells expressing ICUE3 alone or in cells co-transfected with ICUE3 and hLHR-mCherry vectors, increasing numbers of ICUE3 per cell does not alter the ratio of CFP fluorescence to YFP sensitized emission under conditions where cAMP remains constant. This relationship between ICUE3 number, i.e., YFP emission with 488 nm excitation, and CFP/YFP fluorescence upon 405nm excitation occurs both in the presence of 50 μM Fsk and following 100 nM hCG binding to co-expressed hLHR-mCherry. As shown in Figure 2.21, this relationship makes ICUE3 a reliable biosensor to measure the different levels of cAMP.

CHO cells expressing ICUE3 were treated by various concentrations of cAMP together with 0.02% saponin solution. As shown in Figure 2.22, there is almost no change in CFP/YFP upon 405nm excitation in cells treated with 0 μM, 0.1 μM and 1.0 μM cAMP. A large change was observed from 10 μM to 100 μM treatment as indicated by reduced FRET and an increase in the ratio of CFP/YFP emission. A maximum change in the CFP/YFP ratio of 30% was observed when cells were exposed to 1000 μM cAMP. CHO cells expressing ICUE3 and treated with

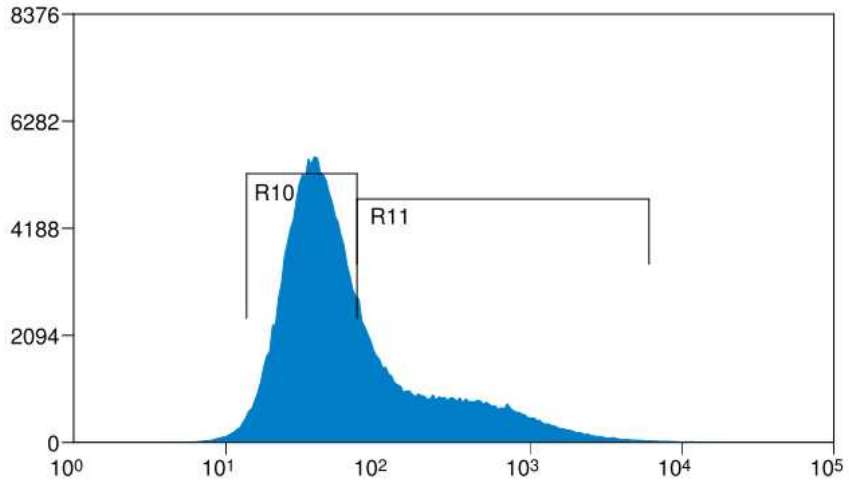

Figure 2.19: Flow cytometry YFP histogram of CHO cells expressing ICUE3 (YFP channel filter 525/40). R10 is the gating area for the control cells. R11 is the gating area for cells with signal from YFP.

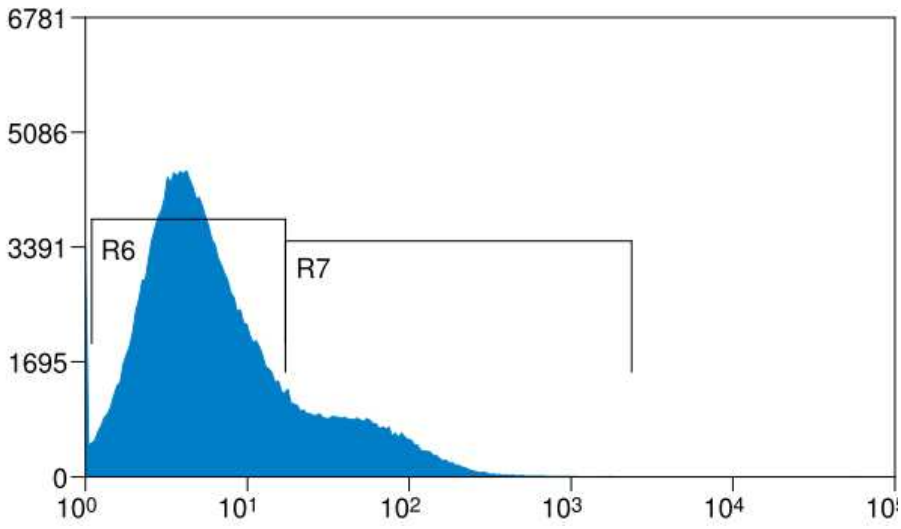

Figure 2.20: Flow cytometry histogram for CHO coexpressing ICUE3 and mCherry (mcherry channel filter 579/16). R6 is the gating area for the control cells. R7 is the gating area for the cells having signal from mCherry.

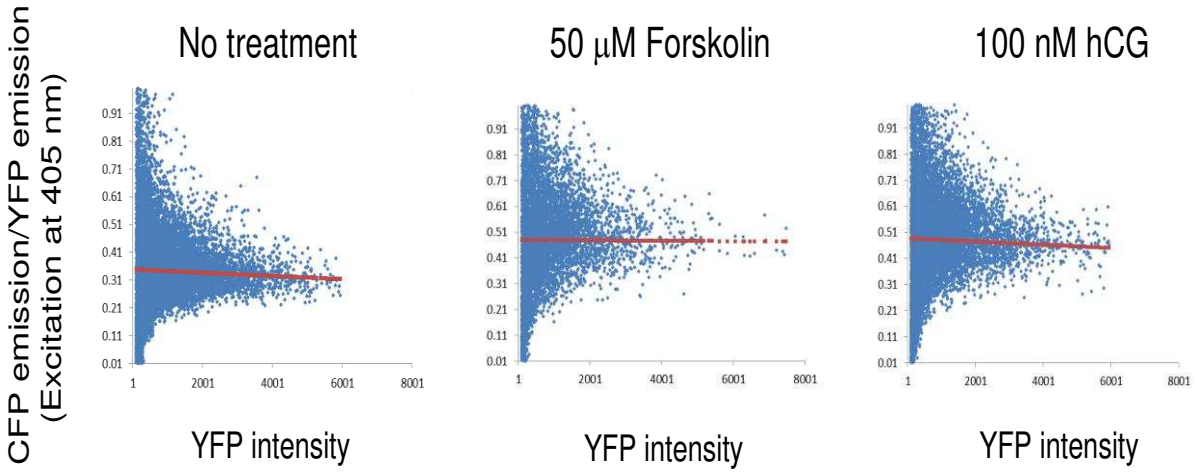

Figure 2.21: Expression of increasing numbers of ICUE3 per cell does not alter the ratio of CFP fluorescence to YFP sensitized emission under conditions where cAMP remains constant. This relationship between ICUE3 number (YFP emission with 488 nm excitation) and CFP/YFP fluorescence upon 405nm excitation occurs both in the presence of forskolin and following hCG binding to co-expressed LHR-mCherry.

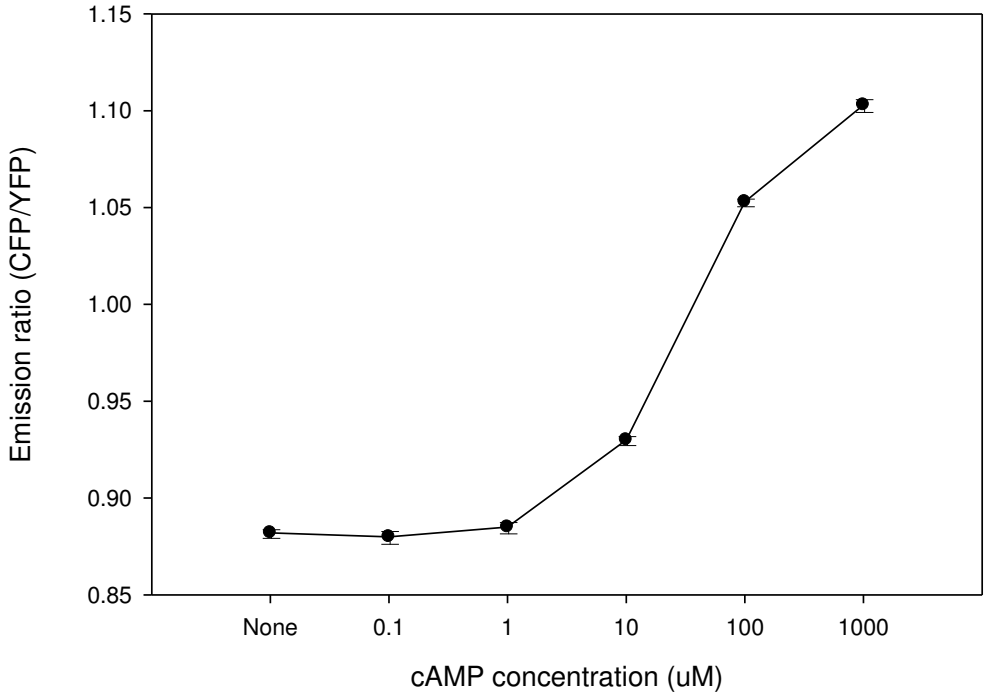

Figure 2.22: Standard curve showing the relationship between the CFP/YFP emission ratio and intracellular cAMP levels. There is a small change in CFP/YFP for 0.1μM, 1.0 μM and 10μM treatment. A large increase is seen for cells treated with 10μM and 100 μM came as indicated by an increase in the ratio of CFP emission/YFP emission. Data shown are the mean ± SD (n > 1000).

different concentrations of cAMP provided a dose response relationship between FRET and intracellular cAMP concentrations. The EC_{50} value of cAMP was in the range 10μM to 100μM which agrees with a previous study using ICUE2 [196].

CHO cells expressing ICUE3 alone are responsive to 50μM Fsk (Figure 2.23). After addition of 50 μM Fsk, cells have increased levels of intracellular cAMP. CHO cells expressing physiologically relevant numbers of hLHR-mCherry per cell and ICUE3 were treated with 50 μM Fsk or 100nM hCG. Figure 2.24 shows that the relationship between LHR numbers and FRET signal for untreated cells and cells treated with 50μM Fsk or 100nM hCG. The results agree with those obtained using the dual emission wavelength ratio imaging method.

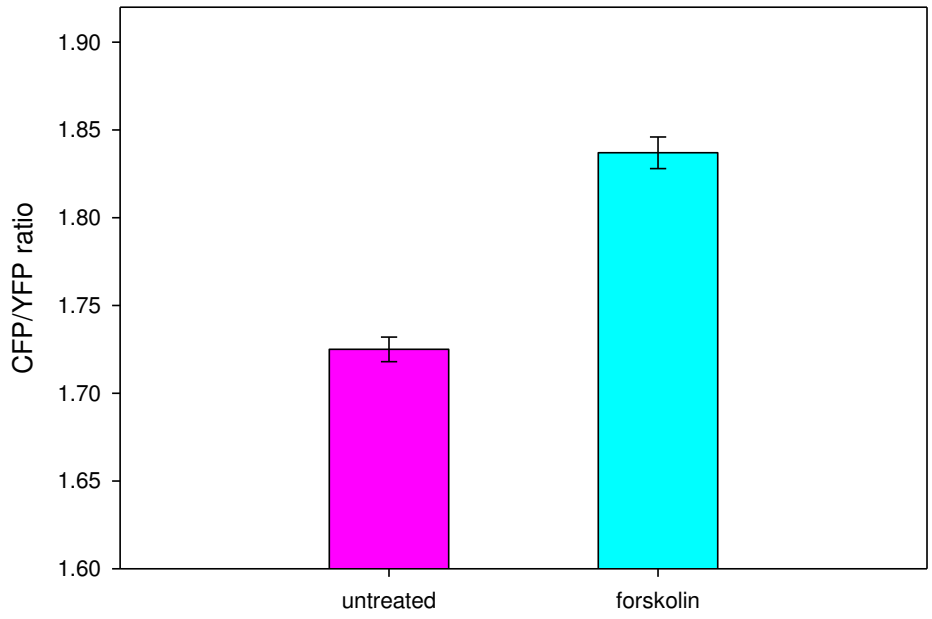

Figure 2.23: CFP/YFP emission ratio changes for CHO cells expressing ICUE3 alone and treated by 50 μM forskolin. The mean values ± S.E.M for ratio measurements are shown.

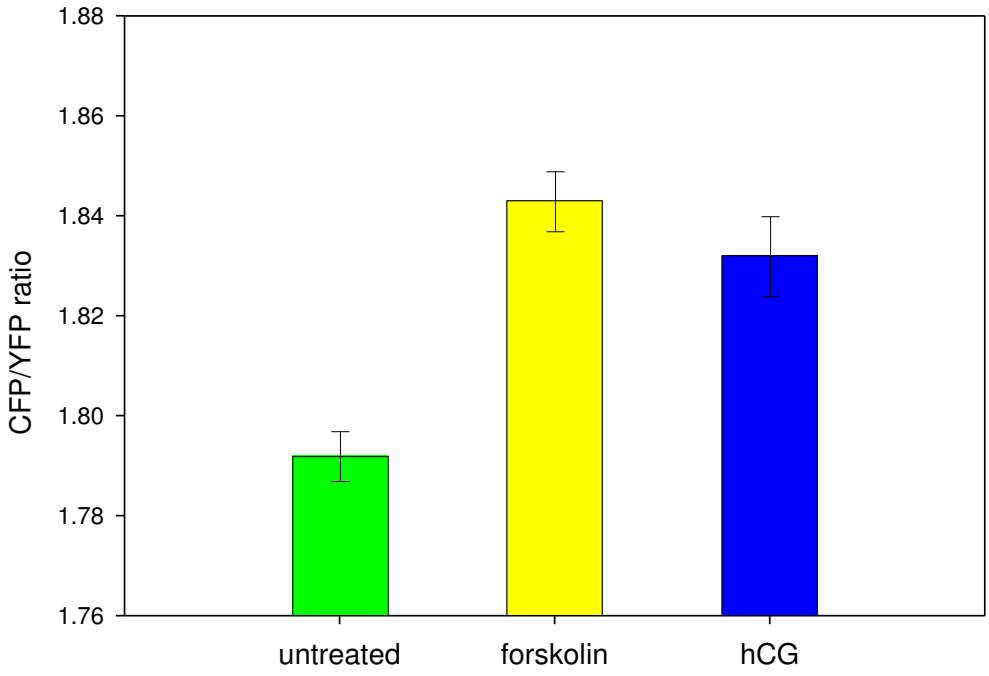

Figure 2.24: CFP/YFP emission ratios for CHO cells co-expressing ICUE3 and 20-60k per cell hLHR-mCherry and treated with 50 μM forskolin or 100 nM hCG. The mean values ± S.E.M. for ratio measurements are shown.

V. CONCLUSION AND FUTURE DIRECTION

Functional LH receptors are critical to fertility and normal reproductive function in both females and males. Hence we have investigated hLHR signal transduction using the cyclic AMP reporter probe, ICUE3. A dual wavelength emission ratio (CFP/YFP) imaging method was used to detect a conformational change in ICUE3 upon binding cAMP. This technique is useful in understanding the sequence of intercellular events following hormone binding to receptor and in particular, the time course involved in signal transduction in a single cell.

Our data suggested that CHO cells expressing ICUE3 and directly treated with different concentrations of cAMP with saponin can provide a dose-dependent relationship for changes in intracellular cAMP levels. 50μM Fsk causes maximal enhancement of the intracellular cAMP and an increase in the CFP/YFP emission ratio. In CHO cells expressing both ICUE3 and hLHR-mCherry, CFP/YFP ratio increased in cells treated with Fsk and also increased measurably in hCG-treated cells. In flow cytometry studies, similar results were obtained when receptor numbers were < 60k LHR-mCherry per cell.

Because ICUE3 can provide real time information on intracellular cAMP levels, this approach can be used to examine various aspects of LH receptor-mediated signaling. For example, membrane rafts are membrane microdomains in the outer leaflet of the lipid bilayer enriched with cholesterol, dynamic clusters of sphingolipids and GPI-anchored proteins, as well as a variety of transmembrane proteins [211]. Lipid rafts are signaling platforms that range in size from 10-200 nm [144, 212, 213]. The integrity of lipid rafts can be disrupted by extracting cholesterol from membranes using MβCD and causing an increase in lipid disorder. It would be of interest to relate LHR affinity for lipid rafts with subsequent signaling. Time-dependent

evaluation of raft association and changes in intracellular cAMP levels following hCG treatment would provide such information.

Flow cytometry together with the FRET-based ICUE3 biosensor is an innovative method to monitor cAMP level changes in cells with quantifiable receptor numbers. Increased intracellular cAMP results in a FRET decrease which is indicated by an increase in the CFP/YFP emission ratio. It is possible for this method to measure intracellular cAMP in individual cells. Different expression levels of ICUE3 do not alter the FRET signal obtained from the ratio of CFP/YFP which makes ICUE3 a reliable sensor of cAMP levels in cells

The next step in this project will be to use ICUE3 together with homo-transfer FRET polarization measurements of mCherry emission and flow cytometry to evaluate whether, on individual cells, there are increases in intracellular cAMP when LHR-mCherry is expressed at high densities and/or aggregated. To adapt homo-transfer FRET methods to flow cytometry we will use two polarizers in front of the two mCherry channels. Fluorescence emission anisotropy will calculated by measuring $I_{\parallel}$ and $I_{\perp}$, fluorescence intensities polarized parallel and perpendicular with respect to exciting light polarization, individually. If FRET occurs, acceptor emission will be oriented differently from donor polarization and anisotropy r will increase. To further analyze these data, we will use a formula describing the dependence of anisotropy of monomers as described by Szabo and coworkers [214]. Cluster size and the percentage of receptor monomers will be determined. From these analyzes, we obtain information on receptor aggregation relative to different receptor expression levels on a cell-by-cell basis, and also determine whether cell signaling is affected from cAMP changes indicated by CFP/YFP emission ratio.

REFERENCES

1. Cole, L. A., Biological functions of hCG and hCG-related molecules, *Reproductive Biology and Endocrinology* **8** (2010).
2. Nakabayashi, K., Matsumi, H., Bhalla, A., Bae, J., Mosselman, S., Hsu, S. Y., and Hsueh, A. J. W., Thyrostimulin, a heterodimer of two new human glycoprotein hormone subunits, activates the thyroid-stimulating hormone receptor, *Journal of Clinical Investigation* **109**, 1445-1452 (2002).
3. Themmen, A. P. N., and Huhtaniemi, I. T., Mutations of gonadotropins and gonadotropin receptors: Elucidating the physiology and pathophysiology of pituitary-gonadal function, *Endocrine Reviews* **21**, 551-583 (2000).
4. Lapthorn, A. J., Harris, D. C., Littlejohn, A., Lustbader, J. W., Canfield, R. E., Machin, K. J., Morgan, F. J., and Isaacs, N. W., Crystal structure of human chorionic gonadotropin, *Nature* **369**, 455-461 (1994).
5. Thotakura, N. R., Weintraub, B. D., and Bahl, O. P., The role of carbohydrate in human chorigonadotropin (hCG) action, *Molecular and Cellular Endocrinology* **70**, 263-272 (1990).
6. Manjunath, P., and Sairam, M., Biochemical, biological, and immunological properties of chemically deglycosylated human choriogonadotropin, *Journal of Biological Chemistry* **257**, 7109-7115 (1982).
7. Sairam, M., and Bhargavi, G., A role for glycosylation of the α subunit in transduction of biological signal in glycoprotein hormones, *Science* **229**, 65-67 (1985).

8. Roess, D. A., Brady, C. J., and Barisas, B. G., Biological function of the LH receptor is associated with slow receptor rotational diffusion, *Biochim Biophys Acta* **1464**, 242-250. (2000).

9. Rao, C. V., An overview of the past, present, and future of nongonadal LH/hCG actions in reproductive biology and medicine, *Seminars in Reproductive Medicine* **19**, 7-17 (2001).

10. Ascoli, M., Fanelli, F., and Segaloff, D., The lutropin/choriogonadotropin receptor, a 2002 perspective, *Endocrine Reviews* **23**, 141-174 (2002).

11. Lennarz, W. J., Lane, M. D., and ebrary Inc. Encyclopedia of biological chemistry, 2nd ed. London, Elsevier, (2013).

12. Dufau, M. L., The luteinizing hormone receptor, *Annual Review of Physiology* **60**, 461-496 (1998).

13. Fredriksson, R., and Schioth, H. B., The repertoire of G-protein-coupled receptors in fully sequenced genomes, *Molecular Pharmacology* **67**, 1414-1425 (2005).

14. McGrath, N. A., Brichacek, M., and Njardarson, J. T., A Graphical Journey of Innovative Organic Architectures That Have Improved Our Lives, *Journal of Chemical Education* **87**, 1348-1349 (2010).

15. McFarland, K., Sprengel, R., Phillips, H., Kohler, M., Rosemblit, N., Nikolics, K., Segaloff, D., and Seeburg, P., Lutropin-choriogonadotropin receptor: An unusual member of the G protein-coupled receptor family, *Science* **245**, 494-499 (1989).

16. Jia, X.-C., Oikawa, M., Bo, M., Tanaka, T., Ny, T., Boime, I., and Hsueh, A. J. W., Expression of human luteinizing hormone (LH) receptor: Interaction with LH and

chorionic gonadotropin from human but not equine, rat, and ovine species, *Molecular Endocrinology* **5**, 759-768 (1991).

17. Segaloff, D. L., and Ascoli, M., The lutropin/choriogonadotropin receptor...4 years later, *Endocrine Reviews* **14**, 324-347 (1993).

18. Sanchez-Yague, J., Rodriquez, M. C., Segaloff, D. L., and Ascoli, M., Truncation of the cytoplasmic tail of the lutropin/choriogonadotropin receptor prevents agonist-induced uncoupling, *Journal of Biological Chemistry* **267**, 7217-7220 (1992).

19. Themmen, A. P. N., An update of the pathophysiology of human gonadotrophin subunit and receptor gene mutations and polymorphisms, *Reproduction* **130**, 263-274 (2005).

20. Wu, S. M., Leschek, E. W., Rennert, O. M., and Chan, W. Y., Luteinizing hormone receptor mutations in disorders of sexual development and cancer, *Frontiers in Bioscience* **5**, D343-D352 (2000).

21. Noci, I., Pillozzi, S., Lastraioli, E., Dabizzi, S., Giachi, M., Borrani, E., Wimalasena, J., Taddei, G. L., Scarselli, G., and Areangeli, A., hLH/hCG-receptor expression correlates with in vitro invasiveness in human primary endometrial cancer, *Gynecologic Oncology* **111**, 496-501 (2008).

22. Gao, X., and Zhang, J., FRET-Based Activity Biosensors to Probe Compartmentalized Signaling, *Chembiochem* **11**, 147-151 (2010).

23. Morozov, A., Muzzio, I. A., Bourtchouladze, R., Van-Strien, N., Lapidus, K., Yin, D. Q., Winder, D. G., Adams, J. P., Sweatt, J. D., and Kandel, E. R., Rap1 couples cAMP signaling to a distinct pool of p42/44MAPK regulating excitability, synaptic plasticity, learning, and memory, *Neuron* **39**, 309-325 (2003).

24. Torgersen, K. M., Vang, T., Abrahamsen, H., Yaqub, S., and Tasken, K., Molecular mechanisms for protein kinase A-mediated modulation of immune function, *Cellular Signalling* **14**, 1-9 (2002).

25. Finn, J. T., Grunwald, M. E., and Yau, K. W., Cyclic nucleotide-gated ion channels: An extended family with diverse functions, *Annual Review of Physiology* **58**, 395-426 (1996).

26. Zagotta, W. N., and Siegelbaum, S. A., Structure and function of cyclic nucleotide-gated channels, *Annual Review of Neuroscience* **19**, 235-263 (1996).

27. Tasken, K., and Aandahl, E. M., Localized effects of cAMP mediated by distinct routes of protein kinase A, *Physiological Reviews* **84**, 137-167 (2004).

28. Taylor, S. S., Buechler, J. A., and Yonemoto, W., CAMP-dependent protein-kinase-framework for a diverse family of regulatory enzymes, *Annual Review of Biochemistry* **59**, 971-1005 (1990).

29. Bos, J. L., Epac: a new cAMP target and new avenues in cAMP research, *Nature Reviews Molecular Cell Biology* **4**, 733-738 (2003).

30. Rich, T. C., Tsf, T. E., Rohan, J. G., Schaack, J., and Karpen, J. W., In vivo assessment of local phosphodiesterase activity using tailored cyclic nucleotide-gated channels as cAMP sensors, *Journal of General Physiology* **118**, 63-77 (2001).

31. Adams, S. R., Harootunian, a. T., Buechler, Y. J., Taylor, S. S., and Tsien, R. Y., Fluorescence ratio imaging of cyclic AMP in single cells, *Nature* **349**, 694-695 (1991).

32. Ponsioen, B., Zhao, J., Riedl, J., Zwartkruis, F., van der Krogt, G., Zaccolo, M., Moolenaar, W. H., Bos, J. L., and Jalink, K., Detecting cAMP-induced Epac activation by fluorescence resonance energy transfer: Epac as a novel cAMP indicator, *Embo Reports* **5**, 1176-1180 (2004).

33. DiPilato, L. M., and Zhang, J., The role of membrane microdomains in shaping beta(2)-adrenergic receptor-mediated cAMP dynamics, *Molecular Biosystems* **5**, 832-837 (2009).

34. DiPilato, L., Cheng, X., and Zhang, J., Fluorescent indicators of cAMP and Epac activation reveal differential dynamics of cAMP signaling within discrete subcellular compartments, *PNAS* **101**, 16513-16518 (2004).

35. Aye-Han, N.-N., Allen, M. D., Ni, Q., and Zhang, J., Parallel tracking of cAMP and PKA signaling dynamics in living cells with FRET-based fluorescent biosensors, *Molecular Biosystems* **8**, 1435-1440 (2012).

36. Hunzicker-Dunn, M., Barisas, G., Song, J., and Roess, D. A., Membrane organization of luteinizing hormone receptors differs between actively signaling and desensitized receptors, *J Biol Chem* **278**, 42744-42749 (2003).

37. Pierce, K. L., Premont, R. T., and Lefkowitz, R. J., Seven-transmembrane receptors, *Nature Reviews Molecular Cell Biology* **3**, 639-650 (2002).

38. Gudermann, T., Birnbaumer, M., and Birnbaumer, L., Evidence for dual coupling of the murine luteinizing hormone receptor to adenylyl cyclase and phophoinositide breakdown and Ca^{2+} mobilization, *Journal of Biological Chemistry* **267**, 4479-4488 (1992).

39. Salvador, L. M., Maizels, E., Hales, D. B., Miyamoto, E., Yamamoto, H., and Hunzicker-Dunn, M., Acute signaling by the LH receptor is independent of protein kinase C activation, *Endocrinology* **143**, 2986-2994 (2002).

40. MacDonald, J. M., Beach, M. G., Porpiglia, E., Sheehan, A. E., Watts, R. J., and Freeman, M. R., The Drosophila cell corpse engulfment receptor draper mediates glial clearance of severed axons, *Neuron* **50**, 869-881 (2006).

41. Leitz, A. J., Bayburt, T. H., Barnakov, A. N., Springer, B. A., and Sligar, S. G., Functional reconstitution of beta(2)-adrenergic receptors utilizing self-assembling Nanodisc technology, *Biotechniques* **40**, 601-602, 604, 606, (2006).

42. Whorton, M., Bokoch, M., Rasmussen, S., Huang, B., Zare, R., Kobilka, B., and Sunahara, R., A monomeric G protein-coupled receptor isolated in a high-density lipoprotein particle efficiently activates its G protein, *Proc Natl Acad Sci USA* **104**, 7682 - 7687 (2007).

43. Milligan, G., G protein-coupled receptor hetero-dimerization: contribution to pharmacology and function, *British Journal of Pharmacology* **158**, 5-14 (2009).

44. Ferre, S., Casado, V., Devi, A., Filizola, M., Jockers, R., Lohse, M. J., Milligan, G., Pin, J.-P., and Guitart, X., G protein-coupled receptor oligomerization revisited: functional and Pharmacological perspectives, *Pharmacological Reviews* **66**, 413-434 (2014).

45. Fuxe, K., Marcellino, D., Borroto-Escuela, D. O., Frankowska, M., Ferraro, L., Guidolin, D., Ciruela, F., and Agnati, L. F., The changing world of G protein-coupled receptors: from monomers to dimers and receptor mosaics with allosteric receptor-receptor interactions, *Journal of Receptors and Signal Transduction* **30**, 272-283 (2010).

46. Agnati, L. F., Fuxe, K., Zoli, M., Rondanini, C., and Ogren, S. O., New vistas on synaptic plasticity: the receptor mosaic hypothesis of the engram, *Medical Biology* **60**, 183-190 (1982).

47. Fuxe, K., Borroto-Escuela, D. O., Romero-Fernandez, W., Palkovits, M., Tarakanov, A. O., Ciruela, F., and Agnati, L. F., Moonlighting Proteins and Protein-Protein Interactions as Neurotherapeutic Targets in the G Protein-Coupled Receptor Field, *Neuropsychopharmacology* **39**, 131-155 (2014).

48. Borroto-Escuela, D. O., Romero-Fernandez, W., Garriga, P., Ciruela, F., Narvaez, M., Tarakanov, A. O., Palkovits, M., Agnati, L. F., and Fuxe, K. G Protein-Coupled Receptor Heterodimerization in the Brain, In *G Protein Coupled Receptors: Trafficking and Oligomerization* (Conn, P. M., Ed.), pp 281-294 (2013).

49. Borroto-Escuela, D. O., Romero-Fernandez, W., Rivera, A., Van Craenenbroeck, K., Tarakanov, A. O., Agnati, L. F., and Fuxe, K., On the G-Protein-Coupled Receptor Heteromers and Their Allosteric Receptor-Receptor Interactions in the Central Nervous System: Focus on Their Role in Pain Modulation, *Evidence-Based Complementary and Alternative Medicine* (2013).

50. Skieterska, K., Duchou, J., Lintermans, B., and Van Craenenbroeck, K. Detection of G Protein-Coupled Receptor (GPCR) Dimerization by Coimmunoprecipitation, In *Receptor-Receptor Interactions* (Conn, P. M., Ed.), pp 323-340 (2013).

51. Chabre, M., and le Maire, M., Monomeric G-protein-coupled receptor as a functional unit, *Biochemistry* **44**, 9395-9403 (2005).

52. James, J. R., Oliveira, M. I., Carmo, A. M., Iaboni, A., and Davis, S. J., A rigorous experimental framework for detecting protein oligomerization using bioluminescence resonance energy transfer, **3**, 1001-1006 (2006).

53. Roess, D. A., and Smith, S. M. L., Self-association and raft localization of functional luteinizing hormone receptors, *Biology of Reproduction* **69**, 1765-1770 (2003).

54. Szidonya, L., Cserzo, M., and Hunyada, L., Dimerization and oligomerization of G-protein-coupled receptors: debated structures with established and emerging functions, *Journal of Endocrinology* **196**, 435-453 (2008).

55. Pfleger, K. D. G., and Eidne, K. A., Monitoring the formation of dynamic G-protein-coupled receptor-protein complexes in living cells, *Biochemical Journal* **385**, 625-637 (2005).

56. Lohse, M. J., Dimerization in GPCR mobility and signaling, *Current Opinion in Pharmacology* **10**, 53-58 (2010).

57. James, J. R., Oliveira, M. I., Carmo, A. M., Iaboni, A., and Davis, S. J., A rigorous experimental framework for detecting protein oligomerization using bioluminescence resonance energy transfer, *Nat Methods* **3**, 1001-1006 (2006).

58. Meyer, B. H., Segura, J. M., Martinez, K. L., Hovius, R., George, N., Johnsson, K., and Vogel, H., FRET imaging reveals that functional neurokinin-1 receptors are monomeric and reside in membrane microdomains of live cells, *Proceedings of the National Academy of Sciences of the United States of America* **103**, 2138-2143 (2006).

59. Runnels, L. W., and Scarlata, S. F., Theory and application of fluorescence homotransfer to melittin oligomerization, *Biophysical Journal* **69**, 1569-1583 (1995).

60. Yeow, E. K. L., and Clayton, A. H. A., Enumeration of Oligomerization States of Membrane Proteins in Living Cells by Homo-FRET Spectroscopy and Microscopy: Theory and Application, *Biophysical Journal* **92**, 3098-3104 (2007).

61. Ganguly, S., Clayton, A. H. A., and Chattopadhyay, A., Organization of Higher-Order Oligomers of the Serotonin1A Receptor Explored Utilizing Homo-FRET in Live Cells, *Biophysical Journal* **100**, 361-368 (2011).

62. Melo, A. M., Fedorov, A., Prieto, M., and Coutinho, A., Exploring homo-FRET to quantify the oligomer stoichiometry of membrane-bound proteins involved in a

cooperative partition equilibrium, *Physical Chemistry Chemical Physics* **16**, 18105-18117 (2014).

63. Zimmerman, S. B., and Minton, A. P., Macromolecular crowding: Biochemical, biophysical, and physiological consequences, *Annual Reviews of Biophysical Biomolecular Structure* **22**, 27-65 (1993).

64. Van Den Berg, E., Van Oven, M. W., De Jong, B., Dam, A., Wiersema, J., Dijkhuizen, T., Hoekstra, H. J., and Molenaar, W. M., Comprison of cytogenetic abnormalities and deoxyribonucleic acid ploidy of benign, borderline malignant, and different grades of malignant soft tissue tumors, *Laboratory Investigation* **70, no. 3**, 307-313 (1994).

65. Alberts, B., The cell as a collection of protein machines: Preparing the next generation of molecular biologists, *Cell* **92**, 291-294 (1998).

66. Kuznetsova, I. M., Turoverov, K. K., and Uversky, V. N., What Macromolecular Crowding Can Do to a Protein, *International Journal of Molecular Sciences* **15**, 23090-23140 (2014).

67. Minton, A. P., Models for excluded volume interaction between an unfolded protein and rigid macromolecular cosolutes: Macromolecular crowding and protein stability revisited, *Biophysical Journal* **88**, 971-985 (2005).

68. Ellis, R. J., Macromolecular crowding: obvious but underappreciated, *Trends in Biochemical Sciences* **26**, 597-604 (2001).

69. Zhou, H.-X., Rivas, G., and Minton, A. P. Macromolecular crowding and confinement: Biochemical, biophysical, and potential physiological consequences, In *Annual Review of Biophysics*, pp 375-397 (2008).

70. Ralston, G. B., Effects of "crowding" in protein solutions, *Journal of Chemical Education* **67**, 857-860 (1990).

71. Roess, D. A., Jewell, M. A., Philpott, C. J., and Barisas, B. G., The rotational diffusion of LH receptors differs when receptors are occupied by hCG versus LH and is increased by Cytochalasin D, *Biochimica et Biophysica Acta* **1357**, 98-106 (1997).

72. Lei, Y., Hagen, G., Smith, S., Liu, J., Barisas, B. G., and Roess, D., Constitutively-active human LH receptors are self-associated and localized in rafts, *Molecular and Cellular Endocrinology* **260-262**, 65-72 (2007).

73. Smith, S. M., Lei, Y., Liu, J., Cahill, M. E., Hagen, G. M., Barisas, B. G., and Roess, D. A., Luteinizing hormone receptors translocate to plasma membrane microdomains after binding of human chorionic gonadotropin, *Endocrinology* **147**, 1789-1795. Epub 2006 Jan 1712. (2006).

74. Horvat, R. D., Roess, D. A., Nelson, S. E., Barisas, B. G., and Clay, C. M., Binding of agonist but not antagonist leads to fluorescence energy transfer between intrinsically-fluorescent gonadotropin releasing hormone receptors, *Mol Endo* **15**, 695-703 (2001).

75. Tao, Y.-X., Johnson, N. B., and Segaloff, D. L., Constitutive and agonist-dependent self-association of the cell surface human lutropin receptor, *Also in endnote B1530 G#0452* **279**, 5904-5914 (2004).

76. Roess, D. A., Rahman, N. A., Kenny, N., and Barisas, B. G., Lateral and rotational dynamics of LH receptors on rat luteal cells, *Biochimica et Biophysica Acta* **1137**, 309-316 (1992).

77. Philpott, C. J., Rahman, N. A., Kenny, N., Londo, T. R., Young, R. M., Barisas, B. G., and Roess, D. A., Rotational dynamics of luteinizing hormone receptors and MHC class I antigens on murine leydig cells, *Biochimica et Biophysica Acta* **1235**, 62-68 (1995).

78. Roess, D. A., Horvat, R. D., Munnelly, H., and Barisas, B. G., Luteinizing hormone receptors are self-associated in the plasma membrane, *Endocrinology* **141**, 4518-4523 (2000).

79. Guan, R., Feng, X., Wu, X., Zhang, M., Zhang, X., Hebert, T., and Segaloff, D., Bioluminescence resonance energy transfer studies reveal constitutive dimerization of the human lutropin receptor and a lack of correlation between receptor activation and propensity for dimerization, *J Biol Chem* **284**, 7483-7494 (2009).

80. Perrin, F., Polarisation de la Lumiere de Fluorescence. Vie Moyenne des Molecules dan L'etat Excite, *J. Phys.* **12**, 390-401 (1926).

81. Forster, T., Zwischenmolekulare energiewanderung und fluoreszenz, *Annalen Der Physik* **2**, 55-75 (1948).

82. Krishna, M., and Ingole, B., Evolving trends in biosciences: multi-purpose proteins - GFP and GFP-like proteins, *Curr Sci India* **97**, 1022-1032 (2009).

83. Tramier, M., Gautier, I., Piolot, T., Ravalet, S., Kemnitz, K., Coppey, J., Durieux, C., Mignotte, V., and Coppey-Moisan, M., Picosecond-hetero-FRET microscopy to probe protein-protein interactions in live cells, *Biophysical Journal* **83**, 3570-3577 (2002).

84. Vilardaga, J. P., Bunemann, M., Krasel, C., Castro, M., and Lohse, M. J., Measurement of the millisecond activation switch of G protein-coupled receptors in living cells, *Nature Biotechnology* **21**, 807-812 (2003).

85. Hoffmann, C., Gaietta, G., Bunemann, M., Adams, S. R., Oberdorf-Maass, S., Behr, B., Tsien, R. Y., Ellisman, M. H., and Lohse, M. J., A FlAsH-based FRET approach to determine G-protein coupled receptor activation in living cells, *Naunyn-Schmiedebergs Archives of Pharmacology* **369**, R19-R19 (2004).

86. Ferrandon, S., Feinstein, T. N., Castro, M., Wang, B., Bouley, R., Potts, J. T., Gardella, T. J., and Vilardaga, J.-P., Sustained cyclic AMP production by parathyroid hormone receptor endocytosis, *Nature Chemical Biology* **5**, 734-742 (2009).

87. Lidke, D., Nagy, P., Barisas, B., Heintzmann, R., Post, J., Lidke, K., Clayton, A., Arndt-Jovin, D., and Jovin, T., Imaging molecular interactions in cells by dynamic and static fluorescence anisotropy (rFLIM and emFRET), *Biochemical Society Transactions* **31**, 1020-1027 (2003).

88. Weber, G., Polarization of the fluorescence of macromolecules. 1. Theory and experimental method, **51** 145-155 (1952).

89. Gradinaru, C. C., Marushchak, D. O., Samim, M., and Krull, U. J., Fluorescence anisotropy: from single molecules to live cells, *Analyst* **135**, 452-459 (2010).

90. Lakowicz, J. R. *Principles of Fluorescence Spectroscopy*, 3rd ed., Springer, New York, (2006).

91. Jameson, D. M., and Ross, J. A., Fluorescence Polarization/Anisotropy in Diagnostics and Imaging, *Chemical Reviews* **110**, 2685-2708 (2010).

92. Levitt, J. A., Matthews, D. R., Ameer-Beg, S. M., and Suhling, K., Fluorescence lifetime and polarization-resolved imaging in cell biology, *Current Opinion in Biotechnology* **20**, 28-36 (2009).

93. Karpova, T. S., Baumann, C. T., He, L., Wu, X., Grammer, A., Lipsky, P., Hager, G. L., and McNally, J. G., Fluorescence resonance energy transfer from cyan to yellow fluorescent protein detected by acceptor photobleaching using confocal microscopy and a single laser, *J Microsc-Oxford* **209**, 56-70 (2003).

94. Garini, Y., Young, I. T., and McNamara, G., Spectral imaging: Principles and applications, *Cytometry Part A* **69A**, 735-747 (2006).

95. Piston, D. W., and Rizzo, M. A. FRET by fluorescence polarization microscopy, In *Fluorescent Proteins, Second Edition* (Sullivan, K. F., Ed.), pp 415-430 (2008).

96. Chang, C.-W., Sud, D., and Mycek, M.-A. Fluorescence lifetime imaging microscopy, In *Digital Microscopy, 3rd Edition* (Sluder, G., and Wolf, D. E., Eds.), pp 495-+ (2007).

97. Tregidgo, C., Levitt, J. A., and Suhling, K., Effect of refractive index on the fluorescence lifetime of green fluorescent protein, *Journal of Biomedical Optics* **13** (2008).

98. Suhling, K., French, P. M. W., and Phillips, D., Time-resolved fluorescence microscopy, *Photochemical & Photobiological Sciences* **4**, 13-22 (2005).

99. Williams, C., cAMP detection methods in HTS: Selecting the best from the rest, *Nature Reviews Drug Discovery* **3**, 125-135 (2004).

100. Sammak, P. J., Adams, S. R., Harootunian, A. T., Schliwa, M., and Tsien, R. Y., Intracellular cyclic AMP not calcium, determines the direction of vesicle movement in melanophores: direct measurement by fluorescence ratio imaging, *Journal of Cell Biology* **117**, 57-72 (1992).

101. Bacskai, B. J., Hochner, B., Mahautsmith, M., Adams, S. R., Kaang, B. K., Kandel, E. R., and Tsien, R. Y., Spatially resolved dynamics of cAMP and protein kinase A subunits in Aplysia sensory neurons, *Science* **260**, 222-226 (1993).

102. Gorbunova, Y. V., and Spitzer, N. C., Dynamic interactions of cyclic AMP transients and spontaneous Ca2+ spikes, *Nature* **418**, 93-96 (2002).

103. Zaccolo, M., De Giorgi, F., Cho, C. Y., Feng, L. X., Knapp, T., Negulescu, P. A., Taylor, S. S., Tsien, R. Y., and Pozzan, T., A genetically encoded, fluorescent indicator for cyclic AMP in living cells, *Nature Cell Biology* **2**, 25-29 (2000).

104. Violin, J. D., DiPilato, L. M., Yildirim, N., Elston, T. C., Zhang, J., and Lefkowitz, R. J., ?-Adrenergic receptor signaling and desensitization elucidated by quantitative modeling of real time cAMP dynamics, *Journal of Biological Chemistry* **283**, 2949-2961 (2008).

105. DiPilato, L., and Zhang, J., The role of membrane microdomains in shaping beta2-adrenergic receptor-mediated cAMP dynamics, *Molecular Biosystems* **5**, 832-837 (2009).

106. Nagai, T., Yamada, S., Tominaga, T., Ichikawa, M., and Miyawaki, A., Expanded dynamic range of fluorescent indicators for Ca2+ by circularly permuted yellow fluorescent proteins, *Proceedings of the National Academy of Sciences of the United States of America* **101**, 10554-10559 (2004).

107. Pfleger, K. D. G., and Eidne, K. A., Illuminating insights into protein-protein interactions using bioluminescence resonance energy transfer (BRET), *Nature Methods* **3**, 165-+ (2006).

108. Wu, P., and Brand, L., Resonance energy transfer: methods and applications, *Analytical Biochemistry* **218**, 1-13 (1994).

109. Prinz, A., Diskar, M., Erlbruch, A., and Herberg, F. W., Novel, isotype-specific sensors for protein kinase A subunit interaction based on bioluminescence resonance energy transfer (BRET), *Cellular Signalling* **18**, 1616-1625 (2006).

110. Jiang, L. I., Collins, J., Davis, R., Lin, K.-M., DeCamp, D., Roach, T., Hsueh, R., Rebres, R. A., Ross, E. M., Taussig, R., Fraser, I., and Sternweis, P. C., Use of a cAMP BRET sensor to characterize a novel regulation of cAMP by the sphingosine 1-phosphate/G(13) pathway, *Journal of Biological Chemistry* **282**, 10576-10584 (2007).

111. Barak, L. S., Salahpour, A., Zhang, X., Masri, B., Sotnikova, T. D., Ramsey, A. J., Violin, J. D., Lefkowitz, R. J., Caron, M. G., and Gainetdinov, R. R., Pharmacological characterization of membrane-expressed human trace amine-associated receptor 1 (TAAR1) by a bioluminescence resonance energy transfer cAMP biosensor, *Molecular Pharmacology* **74**, 585-594 (2008).

112. Guan, R., Feng, X., Wu, X., Zhang, M., Zhang, X., Hebert, T. E., and Segaloff, D. L., Bioluminescence Resonance Energy Transfer Studies Reveal Constitutive Dimerization of the Human Lutropin Receptor and a Lack of Correlation between Receptor Activation and the Propensity for Dimerization, *Journal of Biological Chemistry* **284**, 7483-7494 (2009).

113. Lei, Y., Hagen, G. M., Smith, S. M., Liu, J., Barisas, G., Roess, D. A., Barisas, B. G., Song, J., Pecht, I., and Cahill, M. E., Constitutively-active human LH receptors are self-associated and located in rafts, *Mol Cell Endocrinol* **260-262**, 65-72 (2007).

114. Crenshaw, S. A. Role of homotropic association of luteinizing hormone receptors in hormone mediated signaling, p 180 pp, Ph.D. thesis. Colorado State University (2012).

115. Broussard, J. A., Rappaz, B., Webb, D. J., and Brown, C. M., Fluorescence resonance energy transfer microscopy as demonstrated by measuring the activation of the serine/threonine kinase Akt, *Nature Protocols* **8**, 265-281 (2013).

116. Lakowicz, J. R. *Principles of fluorescence spectroscopy*, 2nd ed., Kluwer Academic/Plenum, New York, (1999).

117. Bos, J. L., Epac proteins: multi-purpose cAMP targets, *Trends in Biochemical Sciences* **31**, 680-686 (2006).

118. Gorshkov, K., and Zhang, J., Visualization of cyclic nucleotide dynamics in neurons, *Frontiers in Cellular Neuroscience* **8** (2014).

119. Bos, J. L., Epac: a new cAMP target and new avenues in cAMP research, **4**, 733-738 (2003).

120. Weiss, R. R., Sulimovici, S., Macri, J. N., Robins, J., and Roginsky, M. S., Amniotic fluid adenosine 3',5' - monophosphate in prostaglandin-induced midtrimester abortions, *Obstet Gynecol* **49**, 223-226 (1977).

121. Banning, C., Votteler, J., Hoffmann, D., Koppensteiner, H., Warmer, M., Reimer, R., Kirchhoff, F., Schubert, U., Hauber, J., and Schindler, M., A Flow Cytometry-Based FRET Assay to Identify and Analyse Protein-Protein Interactions in Living Cells, *PLoS ONE* **5** (2010).

122. Simons, K., and Ikonen, E., Functional rafts in cell membranes, *Nature* **387**, 569-572 (1997).

123. Patel, H., Murray, F., and Insel, P., G-protein-coupled receptor-signaling components in membrane raft and caveolae microdomains, *Handb Exp Pharmacol*, 167 - 184 (2008).

124. Klarenbeek, J., Jalink, K., Detecting cAMP with an EPAC-based FRET sensor in single living cells, *Methods Mol Biol*, **1071**, 49-58 (2014).

125. Szabo, A., Horvath, G., Szoellosi, J., and Nagy, P., Quantitative characterization of the large-scale association of ErbB1 and ErbB2 by flow cytometric homo-FRET measurements, *Biophysical Journal* **95**, 2086-2096 (2008).

LIST OF ABBREVIATIONS

AC	adenyl cyclase
ATP	adenosine triphosphate
ADP	adenosine diphosphate
BRET	bioluminescence resonance energy transfer
BSA	bovine serum albumin
cAMP	cyclic adenosine monophosphate
CDC25HD	CDC25-homology domain
CFP	cyan fluorescent protein
CHO	chinese hamster ovary
CNB	cyclic nucleotide-binding
CNGC	cyclic nucleotide-gated channels
Da	dalton
DG-hCG	deglycosylated-human chorionic gonadotropin
DMEM	dulbecco's modified minimum essential medium
E	percent energy transfer efficiency
EC_{50}	half-maximal effective concentration
EDTA	ethylenediaminetetraacetic acid
Epac	exchange protein activated by cAMP
FSK	forskolin
FBS	fetal bovine serum
FCET	flow cytometric energy transfer

FCS	fluorescence correlation spectroscopy
FcεRI	type I Fcε receptor
FICRhR	fluorescein-labeled PKA catalytic and a rhodamine-labeled regulatory subunit
FITC	fluorescein isothiocyanate
FLIM	fluorescence lifetime imaging microscopy
FMPP	familial male-limited precocious puberty
FSH	follicle stimulating hormone
g	g-factor
GPCR	G protein-coupled receptor
Gs	stimulatory G protein
GDP	guanosine diphosphate
GTP	guanosine triphosphate
hCG	human chorionic gonadotropin
hetero-FRET	heterotransfer fluorescence resonance energy transfer
hLHR	human luteinizing hormone receptor
homo-FRET	homotransfer fluorescence resonance energy transfer
LH	luteinizing hormone
LHR	luteinizing hormone receptor
LP	lipofectamine
MESF	molecules of equivalent soluble fluorophores
MβCD	methyl-beta cyclodextrin
PBS	phosphate buffered saline

PKA	protein kinase A
r	anisotropy
r_0	Förster distance
RA	Ras-association
RCT	rotational correlation time
REM	Ras exchange motif
RET	resonance energy transfer
RIAs	Radioimmunoassays
rLHR	rat luteinizing hormone receptor
TPA	time-resolved phosphorescence anisotropy
TSH	thyroid stimulating hormone
Wt	wild type
YFP	yellow fluorescent protein

CHAPTER III

DISSERTATION SUMMARY AND FUTURE DIRECTION

The plasma membrane of cells is important in cell function. The membrane is made up of a lipid bilayer with proteins imbedded in the bilayer. The membrane serves as a barrier between the outside environment and the interior of the cell. It also permits communication between the exterior environment and the cell. Most cell communication functions are handled by plasma membrane proteins.

Understanding the mechanisms involved in communication between the cell's external environment and the cell interior is important to understanding overall cell function and, for pharmaceutical companies, the design and function of drugs that are targeted to the cell membrane and, more specifically to membrane proteins embedded in the lipid bilayer. Among membrane proteins, two classes are of special interest, tyrosine kinase receptors and G-protein coupled receptors. One example of each type of membrane protein is the subject of Chapter I and Chapter II in this dissertation.

The Type I Fcε receptor is a tyrosine kinase receptor that mediates many of the symptoms associated with allergic responses. This membrane protein is found on cells that are part of the immune system. When an allergen attaches to multiple Fcε receptors on the cell membrane, the cell releases chemicals including histamine that trigger sneezing and nasal congestion.

The other receptor studied in this dissertation is the luteinizing hormone receptor. Like the Fcε receptor, the LH receptor is a membrane protein. It recognizes small molecules secreted by a gland in the brain and, upon interacting with these small molecules, starts chemical processes in the cell that lead to the synthesis of steroid hormones that are important in reproduction. In men, the LH receptor is necessary for testosterone synthesis and, in women, the

LH receptor is necessary for the synthesis of estrogens and progesterone. There are some known structural changes in the LH receptor that cause diseases affecting male reproductive organs. One structural change in the receptor reduces the activity of this membrane protein and results in Leydig cell hypoplasia. There are also structural changes that are associated with genetic disease, in particular, familial male-limited precocious puberty (FMPP). In this case, the receptor is overly active and causes the onset of puberty in male children as young as five years old. More recently, it has been confirmed that LH receptors can be detected in human endometrial cancer and that their expression is apparently related to the cancer grading [21].

The goal of this research was to study the mechanism by which Fcε receptor and LH receptor function as part of cell communication. We have focused on the plasma membrane events that are associated with the reception of signal by Fcε receptor and on improving methods to count the number of LH receptors that are involved in transduction of a transmembrane signal to the cell interior.

Although it is known that Fcε receptors signal when multiple copies of the receptor involved in responding to antigen associate into clusters, the number of Fcε receptors that must be present in that cluster is not known. To determine the number of Fcε receptors that must be present in a cluster, we have developed a method to measure a property of the receptors that is affected by cluster size. All proteins have the ability to rotate about their axis in the lipid bilayer that makes up the surface of the cell. The rate of their motion is dependent on the size of the cluster. Our method looks at individual Fcε receptors that are tagged with a quantum dot, a fluorescent particle that, when attached to a membrane protein, is able to rotate together with the membrane protein to which it is attached and produce a fluorescence signal that can be detected. That fluorescence signal has a time for rotational motion that can be measured and used to

estimate the size of the cluster containing Fcε receptors. In proof-of-principle experiments, we have shown that, even though quantum dots exhibit blinking, i.e., the loss of fluorescence emission for variable lengths of time, we can use the rotational times of these probes to measure Fcε receptor rotation. In the future, we expect to quantify the number of Fcε receptors that are present in clusters on living cells, a measurement that has not been possible before, and to determine whether the extent of disruption of Fcε receptor clusters by pharmaceutical agents is important in reducing the symptoms of immune system responses to allergens. This will have important ramifications for the development of new pharmacologic strategies to treat allergies.

LH receptors also form clusters of unknown size on the cell membrane upon binding of a protein secreted by the brain. The size of these clusters has been estimated to be as high as 9 monomers units. One problem with previous studies is that they have used methods that depend on the introduction of new receptors into the membrane of a cell in numbers that are considerably higher than those found in the gonads of males or females. When receptor number become very high, the LH receptors tend to cluster spontaneously and transfer a signal to the interior of the cell. In this dissertation, we have developed a flow cytometry method to study, in individual cells, the relationship between the number of LH receptors in the cell membrane and the intracellular signal that is generated by those receptors. This involved a fluorescent reporter molecule, ICUE3, which detects the intracellular signal, cyclic adenosine monophosphate. Now that we have demonstrated that this method is both feasible and robust, we will use single cells from the mare to determine whether there are critical numbers of receptors that are needed for a productive signal in cells involved in oocyte development in the ovary. This will have important implications for the treatment of infertility in women linked to a lack of LH receptor function. If the membrane must have sufficient receptors for clustering of the LH receptors, the flow

cytometry methods that we have developed in this dissertation may have clinical applications in evaluating the likelihood of successful oocyte development in *in vitro* fertilization protocols.

In conclusion, a better understanding of membrane proteins and, in particular, the clustering of membrane proteins and its relationship to cell signaling, is important in physiology and in drug development. Improved and robust methods for single cell and single molecule assays of receptor cluster size and coupling of these assays to evaluation of levels of cell signaling molecules like cyclic adenosine monophosphate provide valuable tools to support drug development and clinical diagnostic testing. The methods that we have developed in this dissertation are broadly applicable to other tyrosine kinase receptors and to G-protein coupled receptors which are one of the largest classes of membrane proteins and a highly studied target of new pharmaceutical agents.

APPENDIX I

This paper had been published in *Dalton Transactions*, ***Vol.* 42**, 11912-11920 (2013)

Raft Localization of Type I Fcε Receptor and Degranulation of RBL-2H3 cells Exposed to Decavanadate, a structural model for V_2O_5

Abeer Al-Qatati,†[a,b] Fabio L. Fontes,† [a,c] B. George Barisas,[a,c] Dongmei Zhang,[c] Deborah A. Roess[a,b] and Debbie C. Crans*[a,c]

[a]Cell and Molecular Biology Program, [b]Department of Biomedical Sciences, [c]Department of Chemistry, Colorado State University, Fort Collins, Colorado 80523,

*Address all correspondence and requests for reprints to: Debbie C. Crans, Department of Chemistry, 1301 Center Ave, Colorado State University, Fort Collins, CO 80523. Email: debbie.crans@colostate.edu.

† These individuals contributed equally to this work

Abstract

Vanadium oxides (VOs) have been identified as low molecular weight sensitizing agents associated with occupational asthma and compromised pulmonary immunocompetence. Symptoms of adult onset asthma result, in part, from increased signal transduction by Type I Fcε receptors (FcεRI) leading to release of vasoactive compounds

including histamine from mast cells. Exposure to (VOs) typically occurs in the form of particles which are insoluble. Upon contact with water or biological fluids, (VOs) form a series of soluble oxoanions, one of which is decavanadate, $V_{10}O_{28}^{6-}$ abbreviated V_{10}, which is structurally related to a common vanadium pentoxide, V_2O_5. Here we investigate whether V_{10} may be initiating plasma membrane events associated with activation of FcεRI signal transduction. We show that exposure of RBL-2H3 cells to V_{10} causes a concentration-dependent increase in degranulation of RBL-2H3 and, in addition, an increase in plasma membrane lipid packing as measured by the fluorescent probe, di-4-ANEPPDHQ. V_{10} also increases FcεRI accumulation in low-density membrane fragments, i.e., lipid rafts, which may facilitate FcεRI signaling. To determine whether V_{10} effects on plasma membrane lipid packing were similarly observed in Langmuir monolayers formed from dipalmitoylphosphatidylcholine (DPPC), the extent of lipid packing in the presence and absence of V_{10} and vanadate was compared. V_{10} increased the surface area of DPPC Langmuir monolayers by 6% and vanadate decreased the surface area by 4%. These results are consistent with V_{10} interacting with this class of membrane lipids and altering DPPC packing.

1. Introduction

Vanadium oxides (VOs) have been identified as low molecular weight sensitizing agents associated with occupational asthma and compromised pulmonary immunocompetence.[1, 2] Vanadium pentoxide (V_2O_5), a common VO, is believed to impact human health.[2, 3] Although V_2O_5 itself is an insoluble material, upon contact with water or biological fluids V_2O_5 forms a series of soluble vanadium oxoanions, depending on specific conditions, the general concept of

species forming illustrated in eqn (1).[4-6] Some of the oxoanions that form are stable, while others, such as the simplest monomeric vanadate form (V_1), convert readily with each of the other oligomeric forms.[4] One of the oxoanions that forms from V_2O_5 in aqueous solution at acidic pH is decavanadate ($V_{10}O_{28}^{6-}$).[4, 6] Decavanadate (V_{10}) is a discrete water-soluble anion which structurally resembles the V_2O_5 surface as shown in Fig. 1.[7, 8] Because of this structural analogy, the effects of this anion on biological systems and its interactions with lipid interfaces and membranes is of particular interest.

$$V_2O_5 + H_2O \rightarrow H_2VO_4^- + H_2V_2O_7^{2-} + V_4O_{12}^{4-} + V_5O_{15}^{5-} + HV_{10}O_{28}^{5-} \quad (1)$$

The species formed from V_{10} upon administration to animals or to cultured cells depends on specific conditions of compound administration and cell environment. The vanadium species formed will vary with slight changes in the specific environment.[9-15] In general simple vanadium coordination complexes are known to form complexes in biological fluids and associate with proteins and metabolites.[16, 17] Although salts such as labile oxovanadates are more reactive, the oxovanadate V_{10} is much more stable in acidic environments.[5] Because there is evidence for interactions between V_{10} and lipid interfaces in several microemulsion-type systems,[18, 19] and we have better understanding of the speciation of oxovanadates in aqueous solution,[4-6] we examined V_{10} interactions in a model system and in cells. Specifically, we determined the biological effects of V_{10}, as a model for V_2O_5, on rat basophilic leukemia (RBL-2H3) plasma membrane functions as well as the interaction of V_{10} with Langmuir monolayers formed from an abundant and common plasma membrane lipid (dipalmitoylphosphatidylcholine (DPPC)).

Symptoms of asthma arise following exocytosis of mast cell and basophil granules containing histamine and other vasoactive compounds.[20] It is generally believed that release of

these granules, i.e., the degranulation response, is initiated by plasma membrane Type I Fcε receptor (FcεRI) signaling which has been extensively studied using RBL-2H3 cells as a mast cell model.[21] Productive cell degranulation is a multi-step process. The FcεRI must first bind IgE which has available binding sites for specific antigens. Subsequent binding of an antigen or allergen to even a small fraction of the FcεRI-bound IgE causes FcεRI receptor crosslinking and clustering leading to discharge of cell granules containing vasoactive amines like histamine and serotonin (reviewed in Ref. 22). FcεRI, like several other receptors involved in immune system regulation, are localized in rafts after FcεRI cross-linking[23] which suggests: (1) that cross-linked FcεRI preferentially interact with membrane microdomains that are detergent insoluble; (2) enriched in phosphatidylcholine and cholesterol; and (3) contain effector proteins involved in downstream intracellular signaling-events.[24]

An alternative mechanism driving FcεRI-initiated accumulation in raft microdomains and subsequent receptor-mediated signaling may involve changes in membrane lipid packing.[22] Reorganization of membrane microdomains resulting from changes in lipid packing affect the preferential association of plasma membrane proteins with the bulk membrane or raft microdomains. Our previous studies have shown that $[VO(malto)]^{2-}$ decreases lipid packing in RBL-2H3 cells[25] and increases insulin receptor localization in plasma membrane raft microdomains. Here we examine whether exposure to V_{10}, as a model for V_2O_5, affects lipid packing in intact RBL-2H3 cells as well as the redistribution of FcεRI from the bulk membrane to membrane raft microdomains and demonstrate that V_{10} exposure is sufficient to initiate mast cell degranulation in the absence of antigen-mediated FcεRI crosslinking. We also explore whether Langmuir monolayers that include V_{10} at concentrations used in cell studies exhibit changes in lipid packing.

2. Results

2.1 Mast cell degranulation occurs in the presence of V_{10}

In initial experiments we examined degranulation of RBL-2H3 cells exposed to V_{10} or to two metal-containing coordination compounds (Fig. 2), chromium picolinate ($Cr(pic)_3$) and bis(maltolato)oxovanadium(IV) (BMOV), shown previously to alter lipid packing in RBL-2H3 cells.[25, 26] RBL-2H3 cells were pre-treated for 1 hr at 37ºC with 0.5 nM DNP-specific A2-IgE, an antibody which binds FcεRI on RBL-2H3 cells via the A2-IgE Fc region. Cells were incubated with 10 μM $Cr(pic)_3$, 2 μM BMOV or 2 μM V_{10} corresponding to 20 μM v-atoms for 45 min at room temperature and FcεRI was then crosslinked using 100 nM DNP_{18}-BSA, a polymeric antigen that binds antigen binding sites on A2-IgE. Degranulation of RBL-2H3 cells was measured using a colorimetric assay kit from Millipore (following the manufacturer's instructions), which detects trypase present in mast cell granules. The optical density in supernatant from cell samples was measured at 405 nm. In all cell samples in which receptors were crosslinked by DNP_{18}-BSA via A2-IgE bound to FcεRI, there was a significant increase in RBL-2H3 cell degranulation compared to untreated cells. The presence of 2 μM V_{10} corresponding to 20 μM v-atoms did not significantly affect absorbance measurements at 405 nm (Fig. 2).

2.2 V_{10} exposure results in concentration dependent degranulation of RBL-2H3 cells

Degranulation of RBL-2H3 cells incubated with V_{10} alone or RBL-2H3 cells where A2-IgE occupied FcεRI was crosslinked by 100 nM DNP_{18}-BSA was investigated using V_{10}

concentrations ranging from 0.02-20 μM V_{10}, Fig. 3. In the absence of FcεRI crosslinking, 0.02-20 μM V_{10} exposure resulted in a significant concentration-dependent increase in RBL-2H3 cell degranulation. When A2-IgE pretreated cells were exposed to various concentrations of V_{10} and DNP_{18}-BSA was used to crosslink A2-IgE occupied FcεRI, there was enhanced degranulation of RBL-2H3 cells at each concentration of V_{10} compared to cells exposed to V_{10} alone. These data suggest that exposure to V_{10} at concentrations between 0.02–20 μM is sufficient to initiate degranulation of RBL-2H3 cells and, in addition, enhances RBL-2H3 degranulation when FcεRI are crosslinked by antigen (Fig. 3).

2.3 Cell plasma membrane lipid order following treatment with V_{10} and raft localization of FcεRI

We then examined concentration dependent effects of V_{10} on lipid packing in otherwise untreated cells and compared these effects with those where A2-IgE occupied FcεRI was subsequently crosslinked with DNP_{18}-BSA. Cells were labeled with di-4-ANEPPDHQ and the ratio of fluorescence emission at 610 and 530 nm was assessed at room temperature as described in Materials and Methods. In otherwise untreated cells, exposure to V_{10} at concentrations between 0.02 μM and 20 μM was associated with a decrease in the 610:530 nm ratio which indicates that V_{10} increased lipid packing at concentrations which also resulted in degranulation of RBL-2H3 cells, Fig. 4. Cells were exposed to these concentrations of sodium vanadate as a control experiment to assess whether the effects of the V_{10} were different from the mixture of V1 and the other vanadate oligomers. Since at these vanadium concentrations and this pH the thermodynamic favorable speciation of the sodium vanadate is mainly in the form of vanadate

monomer,[5, 27] we labelled these measurements as V_1 in Fig. 4. The results with this sample at neutral pH also showed a significant increase in lipid packing at higher concentrations (2.0 μM and 20 μM) although the decrease in the 610:530 ratio was less than seen following exposure to V_{10} alone. Since there are 10-times more vanadium atoms in V_{10} than in V_1, we also checked the effects of 200 μM sodium vanadate (data not shown) which gave a similar response to the 20 μM point in Fig. 4. In cells pretreated with A2-IgE and sequentially exposed to V_{10} and DNP_{18}-BSA to crosslink FcεRI, the extent of lipid packing was unchanged compared to untreated cells. Whether this is because extensive FcεRI crosslinking with DNP_{18}-BSA restricts access of di-4-ANEPPDHQ to some membrane microdomains or has some other effects on membranes is not known.

Because crosslinked FcεRI are known to become concentrated in plasma membrane raft microdomains during signaling events leading to cell degranulation, we examined raft localization of FcεRI in response to 2 μM V_{10} and compared its effects with those of 10 μM $Cr(pic)_3$ and 10 μM BMOV which are known to cause translocation of insulin receptor into rafts on RBL-2H3 cells.[25, 26] As shown in Table 1 both BMOV and V_{10}, but not $Cr(pic)_3$, significantly increased the relative fraction of FcεRI found in high buoyancy membrane fractions in the absence of IgE crosslinking by antigen. Thus exposure of RBL-2H3 cells to V_{10} alone is sufficient to drive the redistribution of FcεRI from the bulk membrane to membrane raft microdomains and suggests that concentrating FcεRI in cholesterol- and phosphatidylcholine-enriched microdomains may initiate FcεRI signaling leading to degranulation of RBL-2H3 cells.

2.4 V_{10} interaction with membrane Langmuir monolayers

Studies of lipid packing in RBL-2H3 cells incubated with V_{10} suggest that V_{10} may be interacting with the plasma membrane lipid interface. To determine whether such interactions were occurring and whether V_{10} alone might be sufficient to alter lipid packing in intact cells, we examined V_{10} interactions with a simple lipid monolayer prepared using pure dipalmitoylphosphatidylcholine (DPPC), an abundant cell membrane lipid in cells. DPPC generates well-defined phase changes in the isotherms generated from subphases prepared from diluted yellow solutions containing either high (200 μM) or low (0.02 μM) concentrations of V_{10} or high (2 mM) or low (0.2 μM) concentrations of V_{10} in terms of the concentration of V-atoms. The subphases were prepared from the V_{10} stock solution by dilution immediately before use. Because the half-life of V_{10} at neutral pH is on the order of 30 hrs, the hydrolysis of V_{10} is negligible on the time-scale of the experiment.[28] In Fig. 5, isotherms are shown at neutral pH for DPPC in the absence or presence of V_{10}. The effects of V_{10} on the lipid monolayer are concentration-dependent and are different for high and low concentrations of V_{10} and for V_{10}-free DPPC monolayers.

$$HV_{10}O_{28}^{5-} \rightarrow H_2V_{10}O_{28}^{4-} \quad (2)$$

$$HV_{10}O_{28}^{5-} \rightarrow H_2VO_4^{-} + H_2V_2O_7^{2-} + V_4O_{12}^{4-} + V_5O_{15}^{5-} \quad (3)$$

We then investigated whether observed differences in Langmuir isotherms were due to changes in the protonation state of V_{10} such as shown in eq. 2. A series of measurements were obtained using HEPES buffer in the subphase to maintain pH. However, HEPES can affect speciation and as a result some studies were also carried out in the absence of HEPES to investigate if the protonation state of V_{10} made a difference in the observations. We did not

observe any differences when comparing the isotherm at pH 5.4 where the main species was $H_2V_{10}O_{28}^{4-}$ or at pH 6.9 where the main species was $HV_{10}O_{28}^{5-}$. These observations rule out the possibility that changes in the protonation state of V_{10} are causing the observed differences in Langmuir monolayer isotherms.

We then investigated whether observed differences in Langmuir isotherms were due to hydrolysis of the yellow V_{10} to form a variety of the colorless V_1 and other oligomers as conceptualized eq. 3 and Fig. 7. These studies (Fig. 6) were carried out because it is known that oxovanadates interconvert and V_{10} at neutral pH in the presence of a catalyst can form the rapidly exchanging, colorless simple oxovanadates (Fig. 7).[27] The possibility that the effects of the yellow V_{10} would be different in a subphase containing HEPES and no HEPES was compared and ruled out at 200 μM V_{10}. Finally, the series of Langmuir monolayer isotherms containing V_{10} were compared with those of DPPC monolayers containing sodium vanadate (labeled as V_1) in Fig. 6. V_{10} increased the surface area of Langmuir monolayers by 6% whereas V_1 decreased surface area by 4%. These studies showed the effects of 0.02 μM V_{10} in Fig. 5 were similar to those observed with 0.02 μM V_1 sodium vanadate (V_1). Since the observations for V_1 at low concentrations are indistinguiable from those observed for V_{10} at low concentration; we suggest that the V_{10} in the presence of HEPES is hydrolyzed.

Because experiments in the absence of HEPES were technically more demanding and it was difficult to control pH, subsequent experiments using V_{10} and, for comparison, V_1 were performed in the presence of the HEPES buffer, which permitted excellent pH control. The effects of V_{10} on monolayers at different V_{10} concentrations in the presence of HEPES are shown in Fig. 8. Solution with high concentrations of V_{10} ($\geq$ 2 μM) increased surface areas while low

concentrations of V_{10} (< 2 μM) decreased surface area. Although studies carried out by continuously adding sodium vanadate (V_1) stock solution to the subphase changed the isotherm, the surface area was never greater than that observed for DPPC alone.

3. Discussion

Studies were carried out to evaluate the effects of V_{10}, a hydrolysis product and structural model of V_2O_5, on RBL-2H3 cell function. We show here that exposure of RBL-2H3 cells to V_{10} alone at comparatively low concentrations (0.02-20 μM) increases plasma membrane lipid packing, the relative numbers of FcεRI in membrane rafts and mast cell degranulation. These results suggest that simple perturbations in lipid packing may be sufficient to drive the accumulation of FcεRI in raft microdomains which, in turn, increases the likelihood of FcεRI-mediated signaling leading to cell degranulation. The concentration of FcεRI in rafts following V_{10} exposure also makes antigen-mediated crosslinking of FcεRIs[29] by DNP_{18}-BSA more likely.[30]

While it is generally believed that soluble V species are responsible for biochemical effects in cells,[2] it is not clear whether the effects of V_{10} solutions on RBL-2H3 cell membranes are caused by V_{10} or a result of the species that form when V_{10} hydrolyzes in biological solutions. The toxicity of V_2O_5 has been associated with its insolubility.[1, 2] However, V_2O_5 oxides are acidic upon dissolution giving rise to protonated oxovanadates as shown in eq. 1.[4, 6, 31, 32] In water VO forms a series of soluble oxoanions such as yellow V_{10} (eq. 1 and 3)[4, 33] and colorless monomeric ($H_2VO_4^-$) and oligomeric oxovanadates which readily interconvert, eq. 1 and Fig. 7.[4] While these species differ in number of V atoms, charge, *etc*., all retain the fundamental

coordination to oxygen that V exhibits in crystalline V_2O_5 fluids.[16] The major forms can exist in different protonation states in biological systems. The actual speciation is therefore likely to depend on pH, concentration and the metabolites that are present.[16, 33-36]

Dilute solutions at equilibrium support less V_{10} compared to more concentrated solutions at the same pH.[35] However, the thermodynamic stability of the anions describes only part of the system because V_{10} is kinetically stable at neutral pH. Since the kinetics of these equilibria can be quite slow at neutral pH, the true equilibrium distributions involving V_{10} are only slowly achieved.[4, 34] Generally, after dissolution, V_2O_5 generates acidic solutions which contain primarily monomeric vanadates and V_{10} (eq. 1) in a protonation state reflecting the specific pH of the solution.[4, 37] As these solutions approach neutral pH more oligomeric vanadates appear.

How V_{10} interacts with biological membranes is not clear. Previous studies have shown that V_{10} penetrates model lipid interfaces in microemulsions under some conditions and, more generally, affects the structure of the lipid interface.[28] In negatively-charged microemulsions formed using a sodium bis(2-ethylhexyl)sulfosuccinate (AOT)/isooctane/water system, V_{10} is repelled by the interface and stays in the water pool of the microemulsion.[28] In positively-charged microemulsions formed from cetyltrimethylammonium bromide (CTAB)/pentanol, isooctane and water, V_{10} is nestled against the interface (Crans, unpublished). In a nonionic surfactant system containing Igepal, isooctane and water, V_{10} in located in the water pool.[38] Because the lipid bilayer of the cell plasma membrane provides a zwitterionic lipid interface, the negative charge of the phosphate head group is near the interface as is the case of the negative charge in the AOT model system while the positive charge in the phosphatidyl choline head group is modeled by the positive charge in CTAB microemulsions. The overall neutral charge of phosphatidylcholine and ethanolamine lipids is best represented by the nonionic surfactant Igepal.

Although the nature of the interactions between V_{10} and the lipid interface are likely to be ionic for the most part, other factors may be important.[18, 28, 38] For example, the protonation state of the V_{10} is sensitive to the interface.[13, 28, 38] Studies carried out with V_{10} and with other metal-complexes[39] suggest that the interface can affect the stability of the coordination complexes[9] as well as their protonation state,[13, 28, 38] and thus their interaction and potential lipid interface penetration.

In order to better understand whether interactions of V_{10}, as a model for V_2O_5, with lipid interfaces are sufficient to alter lipid packing, we examined the interactions of V_{10} with Langmuir monolayers prepared from DPPC. Although the DPPC layer does not represent the heterogeneous lipid mixture present in a biological membrane, V_{10} interactions with DPPC monolayers do reflect the effects of V_{10} on a densely packed lipid monolayer. Isotherms were generated from subphases containing both high and low concentrations of vanadium in a subphase containing HEPES as a buffer to maintain pH. Vanadium(V) interacts the least with HEPES compared to other buffers[27] and will maintain the solution pH. While V_{10} above mM concentrations caused an increase in area, at submillimolar concentrations V_{10} caused a decrease in area (data not shown), a result that was not due to changes in the protonation state of V_{10}. Instead, it appears that these results may be due to hydrolysis of V_{10}. HEPES is known to affect depolymerization of vanadium(IV).[27, 40, 41] Speciation considerations predict that, at submillimolar concentrations, the concentration of V-atoms in the form of V_{10} will decrease dramatically. Presumably, V_{10} does not remain intact at low concentrations because there are not enough V-atoms to maintain the V_{10} cluster.

Hydrolysis products of V_{10} may be responsible for biological effects in RBL-2H3 cells. This notion is supported by Langmuir monolayer studies comparing the effects of V_{10} and V_1 in

a HEPES-free subphase. V_{10} increased the surface area of these monolayers while V_1 decreased the surface area (Fig. 6). Studies conducted in the presence of HEPES where there was better pH control (Fig. 8) showed that at high concentrations of V_{10} ($\geq$ 2 mM), surface areas increased and at low concentrations of V_{10} (< 2 mM), surface areas decreased. If V_1 stock solution was added to subphase, the surface areas never increased above that observed for DPPC alone. These results are consistent with the hydrolysis of V_{10} to V_1 at low V_{10} concentrations, neutral pH and in the presence of HEPES. This may give rise to the isotherms in Figure 4 that are typical of DPPC exposure to V_1 rather than V_{10}.

We cannot rule out, however, the possibility that V_{10} affects RBL-2H3 cell function through a mechanism that is independent of membrane lipid packing. Vanadates interact with most functional groups and such interactions can have an effect on the rate of oxovanadate anion hydrolysis.[4, 33, 42] Some oxoanions have been shown to have markedly different biological effects.[6] For example, vanadate monomer (V_1) is a potent inhibitor for alkaline phosphatase, whereas vanadate dimer and tetramer have no effects.[27, 43] Vanadate tetramer is an inhibitor for 6-phosphogluconate dehydrogenase,[42] glucose-6-phosphate dehydrogenase,[44] and aldolase,[45] while V_1 has no effect on those enzymes. Because of V_{10} solubility in aqueous solution, we and others have examined the effects of this anion and found it can act as either an inhibitor or an activator of enzyme activity and cell growth.[6, 46-72] As an enzyme inhibitor[51, 53, 67, 68] or activator,[56, 72] the anion generally interacts with the enzyme active site, although inhibition through interaction with a substrate has also been reported.[49] Some of these enzymes are soluble enzymes present in the cytoplasm, whereas others are membrane-associated enzymes.[69-72]

4. Conclusion

Treatment of RBL-2H3 cells with solutions of V_{10}, as a model for V_2O_5, caused a concentration-dependent increase in degranulation of RBL-2H3 and, in addition, caused an increase in plasma membrane lipid packing as measured by the fluorescent probe, di-4-ANEPPDHQ. In addition, solutions of V_{10} increased Type I Fcε receptor (FcεRI) accumulation in low-density membrane fragments characteristic of lipid rafts. This result suggests that V_{10}, by altering the extent of lipid packing, may drive the preferential accumulation of FcεRI in rafts where the likelihood of receptor crosslinking and subsequent release of histamine-containing granules increases. Studies of V_{10} in Langmuir monolayers formed from dipalmitoylphosphatidylcholine (DPPC) suggest that the observed differences in isotherms can be correlated with speciation changes; V_{10} causes an increase in the surface area whereas V_1 causes a decrease in surface area. These observations are supported by V_{10} chemistry; under conditions where V_{10} hydrolyzes, effects of V_{10} on surface area in Langmuir monolayers are consistent with the presence of V_1. This result is supported by speciation considerations predicting that V_{10} does not remain intact at low concentrations. Therefore the effects of V_{10} on RBL-2H3 cell lipid packing and degranulation are a result of V_{10} and the hydrolysis of V_{10}. These results support the possibility that in biological systems some effects by larger oxometalates may result from their hydrolysis into smaller or monomeric forms.

5. Materials and Methods

5.1 Materials

DNP_{18}-BSA was purchased from Sigma Chemical Company. A2 IgE was the kind gift of Dr. Israel Pecht (Weizmann Institute, Rehovoth, Israel). Minimum Essential Medium (MEM) with Earle's Balanced Salts was purchased from Thermo Scientific (Logan, Utah). Fetal bovine serum (FBS) was purchased from Gemini BioProducts (Woodland, CA). The phase-sensitive aminonaphthylethenylpyridinum-based dye di-4-ANEPPDHQ[73] was purchased from Invitrogen (Carlsbad, CA). Complete mini-protease inhibitor cocktail tablets were purchased from Roche (Indianapolis, IN). 35mm, #1.5 glass bottom petri dishes were purchased from Willco Wells (Amsterdam, Netherlands). All reagents for Langmuir monolayer studies were purchased from Aldrich except for HEPES and dipalmitoylphosphatidylcholine (DPPC), which were purchased from Fisher and Avanti Polar Lipids, respectively.

5.2 Cell culture

2H3 rat basophilic leukemia (RBL-2H3) cells were maintained in cell medium that included MEM supplemented with Earle's Balanced Salts and 10% FBS, 200 mM L-glutamine, 10,000 U/mL penicillin G, 10 μg/mL streptomycin and 25 μg/mL Fungizone (Gemini BioProducts).

2H3 rat basophilic leukemia (RBL-2H3) cells were maintained in cell medium that included MEM supplemented with Earle's Balanced Salts and 10% FBS, 200 mM L-glutamine,

10,000 U/mL penicillin G, 10 µg/mL streptomycin and 25 µg/mL Fungizone (Gemini BioProducts).

5.3 Assay of RBL-2H3 cell degranulation

Mast cell degranulation and release of trypase, a major component in mast cell granules together with histamine, was assayed using a Millipore kit (Cat. No. IMM001) and Manufacturer's instructions. Results shown are the mean and standard deviation of 3-7 individual experiments performed in triplicate. A *t*-test was used to evaluate differences in the means ($p<0.05$).

5.4 Isolation of plasma membrane rafts

High buoyancy membrane fragments were isolated from RBL-2H3 cells as previously described.[69] The $5x10^7$ cells were washed two times with phosphate-buffered saline, pH 7.2 (PBS) and lysed for 5-10 minutes on ice in 1 mL of a buffer containing 25 mM MES, 150 mM NaCl, 2mM EDTA, 0.25% Triton-X100, and a protease inhibitor cocktail including aprotinin, leupeptin, EDTA, and phenylmethylsulfonyl fluoride (Roche). A low speed 300x g spin was used to remove cell nuclei and large cell debris. Supernatant from this spin (1 mL), which contained plasma membrane fragments, was then combined with an equal volume of 80% sucrose containing 0.25% Triton-X100 and the protease inhibitors to produce a 40% sucrose solution. A discontinuous sucrose gradient containing equal volumes of 10-80% sucrose was created with the sample in 40% sucrose layered within this gradient. The gradient was loaded

into a Beckman SW-41 swinging bucket rotor and spun at 175,000x g for 20 hr at 4°C. After the spin, eighteen 650 μL fractions were carefully collected from the top of the gradient downward. A 50 μL aliquot from each fraction was diluted 1:1 with 95% SDS and 5% β-mercaptoethanol. FcεRI in fractions containing >40% sucrose or <40% sucrose was identified by Western blotting and the relative amount of each protein was determined using a Bio-Rad GS-800 calibrated densitometer. Sucrose concentrations were determined from refractive indices using a Bausch and Lomb refractometer.

5.5 Evaluation of RBL-2H3 cell plasma membrane lipid order

After the various treatments, RBL-2H3 cells were labeled at room temperature with 1.0 μM di-4-ANEPPDHQ for 30 minutes, washed and immersed in buffer for imaging. Confocal fluorescence images were acquired using an Olympus IX-71 inverted microscope equipped with a 60x, 1.2NA water-immersion objective and a FV 300 confocal scanning unit. Cell samples were illuminated with a 488 nm laser. Fluorescence emission, split between detector channels 1 and 2 using a 570 nm dichroic mirror, was collected simultaneously in channel 1 up to 530 nm and in channel 2 using a 605 nm band-pass filter. All images were collected at identical instrument and detector settings with the exception of the laser excitation power, which was adjusted between experiments due to slight variations in labeling efficiency. Background correction and the background-corrected ratio of fluorescence emission at 605 nm to that at 530 nm (red/green) were calculated using NIH Image J 1.42i.

5.6 Langmuir films

The decavanadate (V_{10}) solution was prepared by gently heating sodium metavanadate ($NaVO_3$) in deionized water in about half the volume needed for a 5.0 mM solution. The pH of the clear and yellow solution was adjusted to 5.4 with a hydrogen chloride solution, resulting in an orange solution, and the volume was increased to reach the final 5.0 mM. The vanadate (V_1) solution was prepared by gently heating $NaVO_3$ in deionized water to generate a 5.0 mM solution. Further dilutions were done using the stock solution and either deionized water or 20 mM HEPES buffer, pH 7.2. A 2.00 mg/mL (2.72 mM) stock DPPC solution was prepared by dissolving DPPC in a 3:2 hexane:propanol mixture.

The Langmuir trough experiments followed the general procedure reported previously[70] varying the composition of the subphase using a Kibron MicroTroughXS. The subphase was poured into the trough well to a total volume of 25 mL, and a total amount of 19 nmol of DPPC (7.0 μL of 2.72 mM) was applied to the subphase. The setup was allowed to spread for 15 minutes. At this time the monolayer was compressed at constant temperature and a constant rate of 35 mm/min until the isotherm collapsed. Data was collected using Kibron FilmWarex 3.62 software.

Isotherms were plotted and compression modules calculated for a range of subphases, as described previously.[74] The composition of the subphases varied depending on the probe concentration (from 0.02 to 200 μM), the pH (5.4 – 7.2) and the presence or absence of HEPES (20 mM, pH 7.2).

Acknowledgements

We would like to thank to Drs. Chris D. Rithner and Audra Sostarecz for their helpful discussions. We would also like to acknowledge the support of NSF CHE-0628260 to DCC, DAR and BGB and NSF MCB-1024668 to BGB.

References

1. M. D. Cohen, M. Sisco, C. Prophete, K. Yoshida, L. C. Chen, J. T. Zelikoff, J. Smee, A. A. Holder, J. Stonehuerner, D. C. Crans and A. J. Ghio, *Inhalation Toxicology*, 2010, **22**, 169-178.

2. M. D. Cohen, M. Sisco, C. Prophete, L. C. Chen, J. T. Zelikoff, A. J. Ghio, J. D. Stonehuerner, J. J. Smee, A. A. Holder and D. C. Crans, *Journal of Immunotoxicology*, 2007, **4**, 49-60.

3. F. L. Assem and L. S. Levy, *Journal of Toxicology and Environmental Health Part B Critical Reviews*, 2009, **12**, 289-306.

4. D. C. Crans, J. J. Smee, E. Gaidamauskas and L. Q. Yang, *Chemical Reviews*, 2004, **104**, 849-902.

5. L. Pettersson, B. Hedman, I. Andersson and N. Ingri, *Chem. Scrip.*, 1983, **22**, 254-264.

6. M. Aureliano and D. C. Crans, *Journal of Inorganic Biochemistry*, 2009, **103**, 536-546.

7. D. C. Crans, M. Mahrooftahir, O. P. Anderson and M. M. Miller, *Inorganic Chemistry*, 1994, **33**, 5586-5590.

8. V. P. Filonenko, M. Sundberg, P. E. Werner and I. P. Zibrov, *Acta Crystallographica Section B-Structural Science*, 2004, **60**, 375-381.

9. D. C. Crans, S. Schoeberl, E. Gaidamauskas, B. Baruah and D. A. Roess, *Journal of Biological Inorganic Chemistry*, 2011, **16**, 961-972.

10. K. H. Thompson, I. Setyawati, Y. Sun, V. Yuen, D. Lyster, J. H. McNeill and C. Orvig, *Faseb Journal*, 1997, **11**, 3479-3479.

11. K. H. Thompson and C. Orvig, *Journal of Inorganic Biochemistry*, 2006, **100**, 1925-1935.

12. G. R. Willsky, D. A. White and B. C. McCabe, *Journal of Biological Chemistry*, 1984, **259**, 3273-3281.

13. D. C. Crans, B. Baruah, A. Ross and N. E. Levinger, *Coordination Chemistry Reviews*, 2009, **253**, 2178-2185.

14. G. R. Willsky, D. A. Preischel and B. C. McCabe, *Biophysical Journal*, 1984, **45**, A76-A76.

15. G. Willsky, P. Kaszynski, M. Godzalla, P. Kostyniak and A. Goldfine, *Faseb Journal*, 2000, **14**, A1479-A1479.

16. A. Gorzsas, I. Andersson and L. Pettersson, *European Journal of Inorganic Chemistry*, 2006, 3559-3565.

17. D. Sanna, E. Garribba and G. Micera, *Journal of Inorganic Biochemistry*, 2009, **103**, 648-655.

18. B. Baruah, L. A. Swafford, D. C. Crans and N. E. Levinger, *Journal of Physical Chemistry B*, 2008, **112**, 10158-10164.

19. D. A. Roess, S. M. L. Smith, P. Winter, J. Zhou, P. Dou, B. Baruah, A. M. Trujillo, N. E. Levinger, X. D. Yang, B. G. Barisas and D. C. Crans, *Chemistry & Biodiversity*, 2008, **5**, 1558-1570.

20. M. I. Asher, S. Montefort, B. Bjorksten, C. K. W. Lai, D. P. Strachan, S. K. Weiland and H. Williams, *Lancet*, 2006, **368**, 733-743.

21. E. Passante and N. Frankish, *Inflammation Research*, 2009, **58**, 737-745.

22. S. Kraft and J. P. Kinet, *Nature Reviews Immunology*, 2007, **7**, 365-378.

23. K. A. Field, D. Holowka and B. Baird, *Proceedings of the National Academy of Sciences of the United States of America*, 1995, **92**, 9201-9205.

24. A. M. Davey, K. M. Krise, E. D. Sheets and A. A. Heikal, *Journal of Biological Chemistry*, 2008, **283**, 7117-7127.

25. P. W. Winter, A. Al-Qatati, A. L. Wolf-Ringwall, S. Schoeberl, P. B. Chatterjee, B. G. Barisas, D. A. Roess and D. C. Crans, *Dalton Transactions*, 2012, **41**, 6419-6430.

26. A. Al-Qatati, P. W. Winter, A. L. Wolf-Ringwall, P. B. Chatterjee, A. K. Van Orden, D. C. Crans, D. A. Roess and B. G. Barisas, *Cell Biochemistry and Biophysics*, 2012, **62**, 441-450.

27. D. C. Crans, R. L. Bunch and L. A. Theisen, *Journal of the American Chemical Society*, 1989, **111**, 7597-7607.

28. B. Baruah, J. M. Roden, M. Sedgwick, N. M. Correa, D. C. Crans and N. E. Levinger, *Journal of the American Chemical Society*, 2006, **128**, 12758-12765.

29. N. L. Andrews, J. R. Pfeiffer, A. M. Martinez, D. M. Haaland, R. W. Davis, T. Kawakami, J. M. Oliver, B. S. Wilson and D. S. Lidke, *Immunity*, 2009, **31**, 469-479.

30. A. Carroll-Portillo, K. Spendier, J. Pfeiffer, G. Griffiths, H. T. Li, K. A. Lidke, J. M. Oliver, D. S. Lidke, J. L. Thomas, B. S. Wilson and J. A. Timlin, *Journal of Immunology*, 2010, **184**, 1328-1338.

31. C. Hess, J. D. Hoefelmeyer and T. D. Tilley, *Journal of Physical Chemistry B*, 2004, **108**, 9703-9709.

32. O. Durupthy, M. Jaber, N. Steunou, J. Maquet, G. T. Chandrappa and J. Livage, *Chemistry of Materials*, 2005, **17**, 6395-6402.

33. D. C. Crans, *Comments on Inorganic Chemistry*, 1994, **16**, 1-31.

34. O. Durupthy, N. Steunou, T. Coradin, J. Maquet, C. Bonhomme and J. Livage, *Journal of Materials Chemistry*, 2005, **15**, 1090-1098.

35. D. C. Crans, P. M. Ehde, P. K. Shin and L. Pettersson, *Journal of the American Chemical Society*, 1991, **113**, 3728-3736.

36. T. Jakusch, J. C. Pessoa and T. Kiss, *Coordination Chemistry Reviews*, 2011, **255**, 2218-2226.

37. C. F. Baes and R. E. Mesmer, *The Hydrolysis of Cations*, Wiley, New York, 1976.

38. M. A. Sedgwick, D. C. Crans and N. E. Levinger, *Langmuir*, 2009, **25**, 5496-5503.

39. D. C. Crans, B. Baruah and N. E. Levinger, *Biomedicine & Pharmacotherapy*, 2006, **60**, 174-181.

40. N. D. Chasteen and M. W. Hanna, *The Journal of Physical Chemistry*, 1972, **76**, 3951-3958.

41. N. D. Chasteen, *Structure and Bonding*, 1983, **53**, 105-138.

42. D. C. Crans, C. D. Rithner and L. A. Theisen, *Journal of the American Chemical Society*, 1990, **112**, 2901-2908.

43. L. E. Seargeant and R. A. Stinson, *Biochemical Journal*, 1979, **181**, 247-250.

44. D. C. Crans, E. M. Willging and S. R. Butler, *Journal of the American Chemical Society*, 1990, **112**, 427-432.

45. D. C. Crans, K. Sudhakar and T. J. Zamborelli, *Biochemistry*, 1992, **31**, 6812-6821.

46. F. Yraola, S. Garcia-Vicente, L. Marti, F. Albericio, A. Zorzano and M. Royo, *Chemical Biology & Drug Design*, 2007, **69**, 423-428.

47. S. S. Soares, C. Gutierrez-Merino and M. Aureliano, *Journal of Inorganic Biochemistry*, 2007, **101**, 789-796.

48. S. M. Hua and G. Inesi, *Journal of Biological Chemistry*, 2000, **275**, 30546-30550.

49. S. Pluskey, M. Mahroof-Tahir, D. C. Crans and D. S. Lawrence, *Biochemical Journal*, 1997, **321**, 333-339.

50. M. J. Pereira, E. Carvalho, J. W. Eriksson, D. C. Crans and M. Aureliano, *Journal of Inorganic Biochemistry*, 2009, **103**, 1687-1692.

51. J. M. Messmore and R. T. Raines, *Archives of Biochemistry and Biophysics*, 2000, **381**, 25-30.

52. T. L. Turner, V. H. Nguyen, C. C. McLauchlan, Z. Dymon, B. M. Dorsey, J. D. Hooker and M. A. Jones, *Journal of Inorganic Biochemistry*, 2012, **108**, 96-104.

53. G. Fraqueza, C. A. Ohlin, W. H. Casey and M. Aureliano, *Journal of Inorganic Biochemistry*, 2012, **107**, 82-89.

54. N. Bosnjakovic-Pavlovic, A. Spasojevic-de Bire, I. Tomaz, N. Bouhmaida, F. Avecilla, U. B. Mioc, J. C. Pessoa and N. E. Ghermani, *Inorganic Chemistry*, 2009, **48**, 9742-9753.

55. T. Ramasarma, *Indian Journal of Biochemistry & Biophysics*, 2012, **49**, 295-305.

56. M. Lehir, *Biochemical Journal*, 1991, **273**, 795-798.

57. A. D. Michel, S. W. Ng, S. Roman, W. C. Clay, D. K. Dean and D. S. Walter, *British Journal of Pharmacology*, 2009, **156**, 1312-1325.

58. S. Manon and M. Guerin, *Biochemistry and Molecular Biology International*, 1998, **44**, 565-575.

59. B. Kaboudin, K. Moradi, E. Safaei, H. Dehghan and P. Salehi, *Phosphorus Sulfur and Silicon and the Related Elements*, 2012, **187**, 1521-1527.

60. Z. L. Gao, C. Y. Zhang, S. W. Yu, X. D. Yang and K. Wang, *Journal of Biological Inorganic Chemistry*, 2011, **16**, 789-798.

61. A. Sheela and R. Vijayaraghavan, *Journal of Coordination Chemistry*, 2011, **64**, 511-524.

62. M. Passadouro, A. M. Metelo, A. S. Melao, J. R. Pedro, H. Faneca, E. Carvalho and M. M. C. A. Castro, *Journal of Inorganic Biochemistry*, 2010, **104**, 987-992.

63. C. Sanchez, M. Torres, M. C. Bermudez-Pena, P. Aranda, M. Montes-Bayon, A. Sanz-Medel and J. Llopis, *Magnesium Research*, 2011, **24**, 196-208.

64. M. J. Xie, X. D. Yang, W. P. Liu, S. P. Yan and Z. H. Meng, *Journal of Inorganic Biochemistry*, 2010, **104**, 851-857.

65. H. Sakurai, *Journal of Health Science*, 2010, **56**, 129-143.

66. M. Sutradhar, T. R. Barman, G. Mukherjee, M. Kar, S. S. Saha, M. G. B. Drew and S. Ghosh, *Inorganica Chimica Acta*, 2011, **368**, 13-20.

67. C. X. Yuan, L. P. Lu, X. L. Gao, Y. B. Wu, M. L. Guo, Y. Li, X. Q. Fu and M. L. Zhu, *Journal of Biological Inorganic Chemistry*, 2009, **14**, 841-851.

68. T. Scior, J. A. Guevara-Garcia, F. J. Melendez, H. H. Abdallah, Q. T. Do and P. Bernard, *Drug Design Development and Therapy*, 2010, **4**, 231-242.

69. R. J. Pezza, M. A. Villarreal, G. G. Montich and C. E. Argarana, *Nucleic Acids Research*, 2002, **30**, 4700-4708.

70. P. Proks, R. Ashfield and F. M. Ashcroft, *Journal of Biological Chemistry*, 1999, **274**, 25393-25397.

71. T. Tiago, P. Martel, C. Gutierrez-Merino and M. Aureliano, *Biochimica Et Biophysica Acta-Proteins and Proteomics*, 2007, **1774**, 474-480.

72. B. Neumcke and R. Weik, *European Biophysics Journal*, 1991, **19**, 119-123.

73. L. Jin, A. Millard and L. M. Loew, *Biophysical Journal*, 2005, **88**, 414a-414a.

74. M. Thoma and H. Mohwald, *Colloids and Surfaces A-Physcochemical and Engineering Aspects*, 1995, **95**, 193-200.

Figure Legends

Fig. 1 The partial structure for V_2O_5 sheet is shown (left).[8] The structure for the discrete anion (V_{10},) is shown (right).[7] While V_2O_5 falls apart in solution, the discrete V_{10} anion retains its structure upon dissolution.

Fig. 2 Degranulation of RBL-2H3 cells in response to metal-containing coordination compounds and V_{10} was measured at room temperature as described in Materials and Methods. Experimental conditions are indicated for each cell sample. Degranulation was assessed in untreated RBL-2H3 cells and compared to degranulation responses in cells exposed to A2-IgE and 100 nM DNP_{18}-BSA alone or to cells pretreated with A2-IgE and then exposed to metal-containing compounds and 100 nM DNP_{18}-BSA to crosslink A2-IgE.

Fig. 3 Degranulation of RBL-2H3 cells in the presence of V_{10}. Cell degranulation was measured at room temperature as described in Materials and Methods using supernatant from RBL-2H3 cells incubated with V_{10} alone (o) or following pretreatment of RBL-2H3 cells with A2-IgE, exposure to V_{10} and FcεRI crosslinking via DNP_{18}-BSA (•).

Fig. 4 Fluorescence emission of di-4-ANEPPDHQ labeled RBL-2H3 cells treated with V_{10} or $V_{1.}$ Di-4-ANEPPDHQ fluorescence emission was collected simultaneously at 610 nm and 530 nm at

room temperature as described in Materials and Methods and the ratio of fluorescence emission at 610nm and 530nm was calculated. A significant increase in lipid packing, indicated by a decrease in the ratio of 610nm:530nm emission, is observed following treatment of cells with V_{10} (o) alone for 1 hr at room temperature. V_1, over this same concentration range causes a smaller decreases in the 610nm:530nm ratio and these changes are significant only for cells treated with 2.0 μM or 20 μM V_1 (Δ). Lipid packing was not affected by exposure to any concentration of V_{10} when cells were pretreated with A2-IgE and DNP_{18}-BSA was used to crosslink FcεRI (●).

Fig. 5 Plots of the Langmuir isotherms at room temperature with surface pressure as a function of molecular area. Isotherms in a HEPES buffer subphase (pH 7.2) with V_{10} at 0.02 (long-short dash) and 200 μM (short-short dash) or without V_{10} (no probe, full line).

Fig. 6 Langmuir isotherms prepared by plotting surface pressure against concentration of vanadium compound added to the solutions. Isotherms in an aqueous subphase with either V_1 (at 200 μM, long-short dash), V_{10} (at 200 μM V-atoms, 20 μM V_{10}, short-short dash) or no probe (full line) at pH 6.9.

Fig. 7 Structures of vanadate monomer (V_1), dimer (V_2), tetramer (V_4), and pentamer (V_5).

Fig. 8 Histogram of the molecular area at 30 mN/m as a function of concentration, in a HEPES buffer subphase containing either no probe (crossed bars), V_1 (white bars) or V_{10} (black bars). At lower concentrations, V_{10} shows the same molecular area shown by V_1.

Table 1: Evaluation of the percent of FcεRI distributed in raft and non-raft membrane fragments following treatment of RBL-2H3 cells with 10 μM BMOV, 10 μM $Cr(pic)_3$ or 2 μM V_{10} for 1 hr.

Lanes[1]	Untreated	BMOV	$Cr(pic)_3$	V_{10}
1-9	10 ± 3^a	16 ± 1^b	14 ± 4^a	23 ± 17^b
10-18	90 ± 3^a	84 ± 2^b	85 ± 4^a	77 ± 17^b

[1]Results shown are mean +/- S.E.M. for the distribution of FcεRI in membrane fractions 1-9 and 10-18 for 2-6 experiments performed in triplicate. Values with the superscript a are different from the value for untreated cells using a paired t-test ($p<0.002$) and values with the superscript b are different from the value for untreated cells using a paired t-test ($p<0.02$).

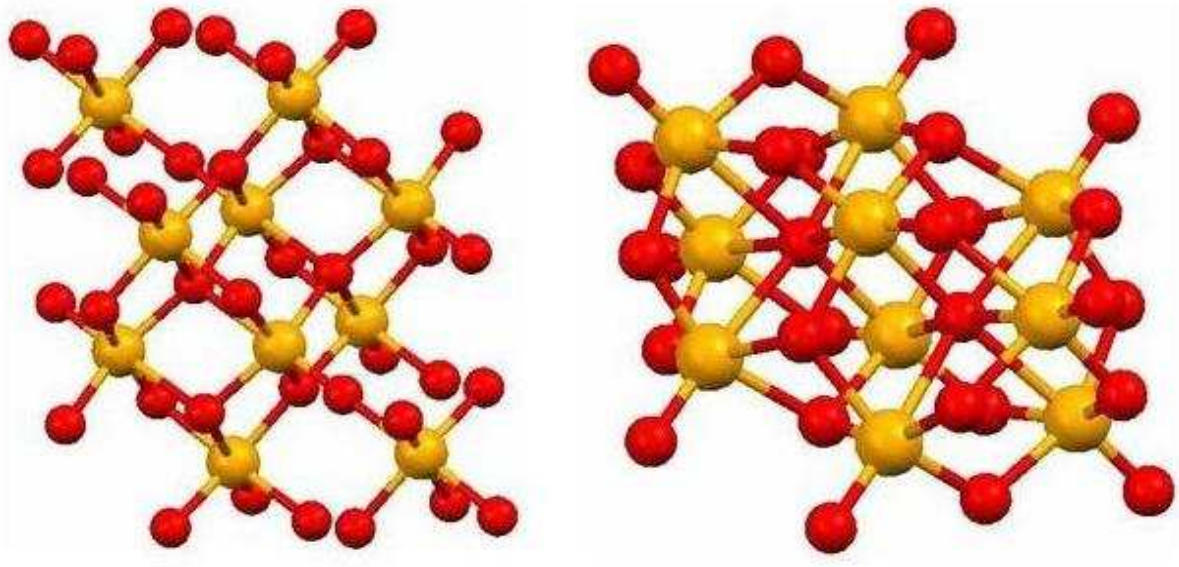

Figure 1

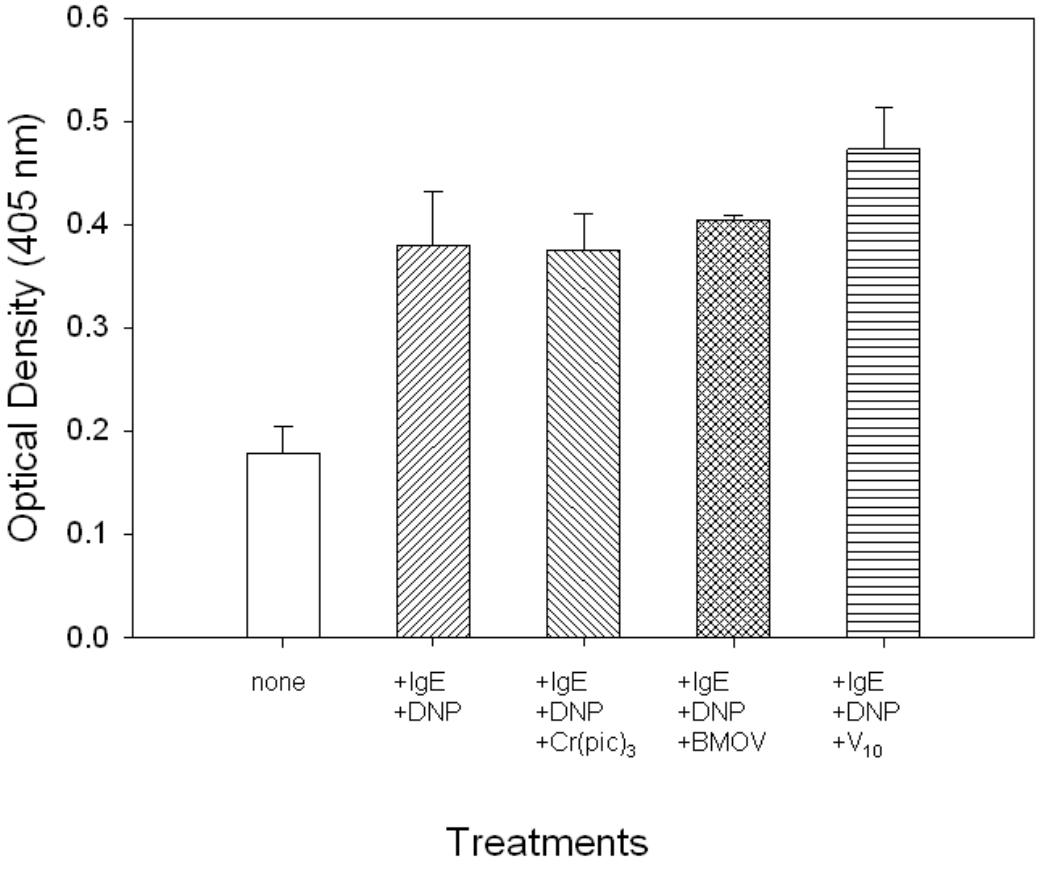
Optical Density (405 nm)
0.6
0.5
0.4
0.3
0.2
0.1
0.0
none
+IgE
+DNP
+IgE
+DNP
+Cr(pic)3
+IgE
+DNP
+BMOV
+IgE
+DNP
+V10
Treatments

Figure 2

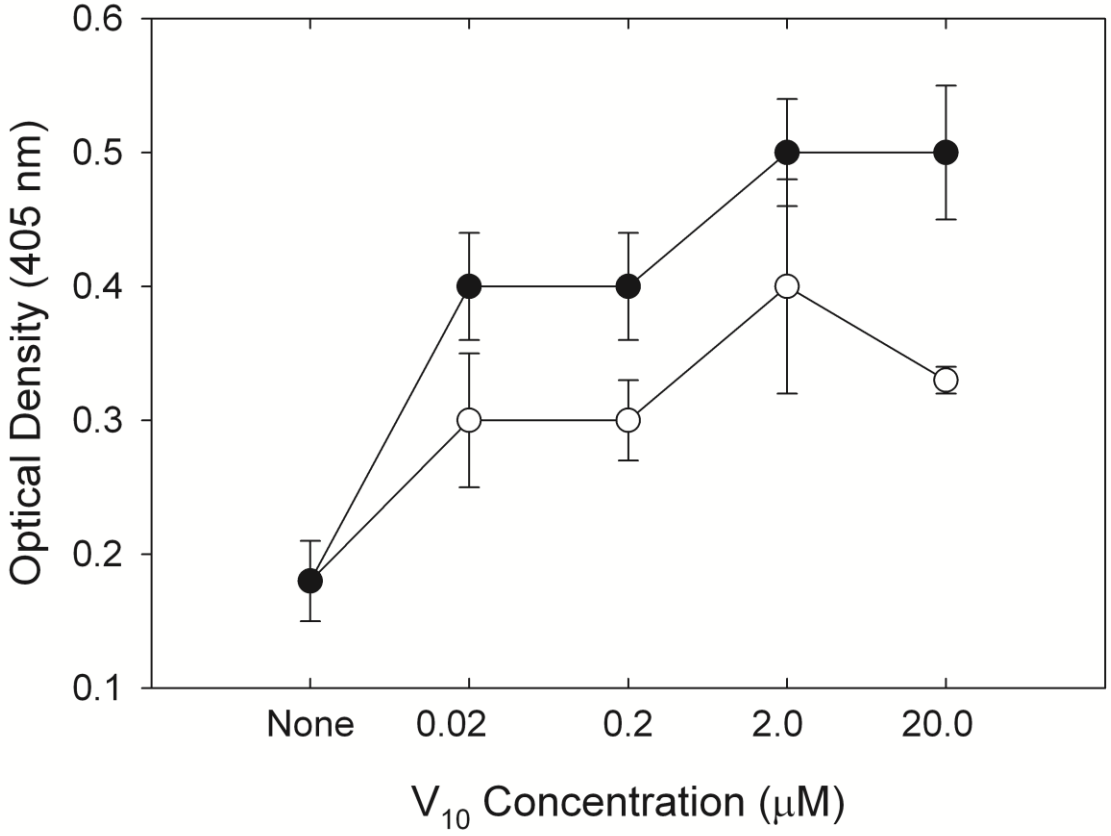
0.6
0.5
0.4
0.3
0.2
0.1
Optical Density (405 nm)
None
0.02
0.2
2.0
20.0
V10 Concentration (μM)

Figure 3

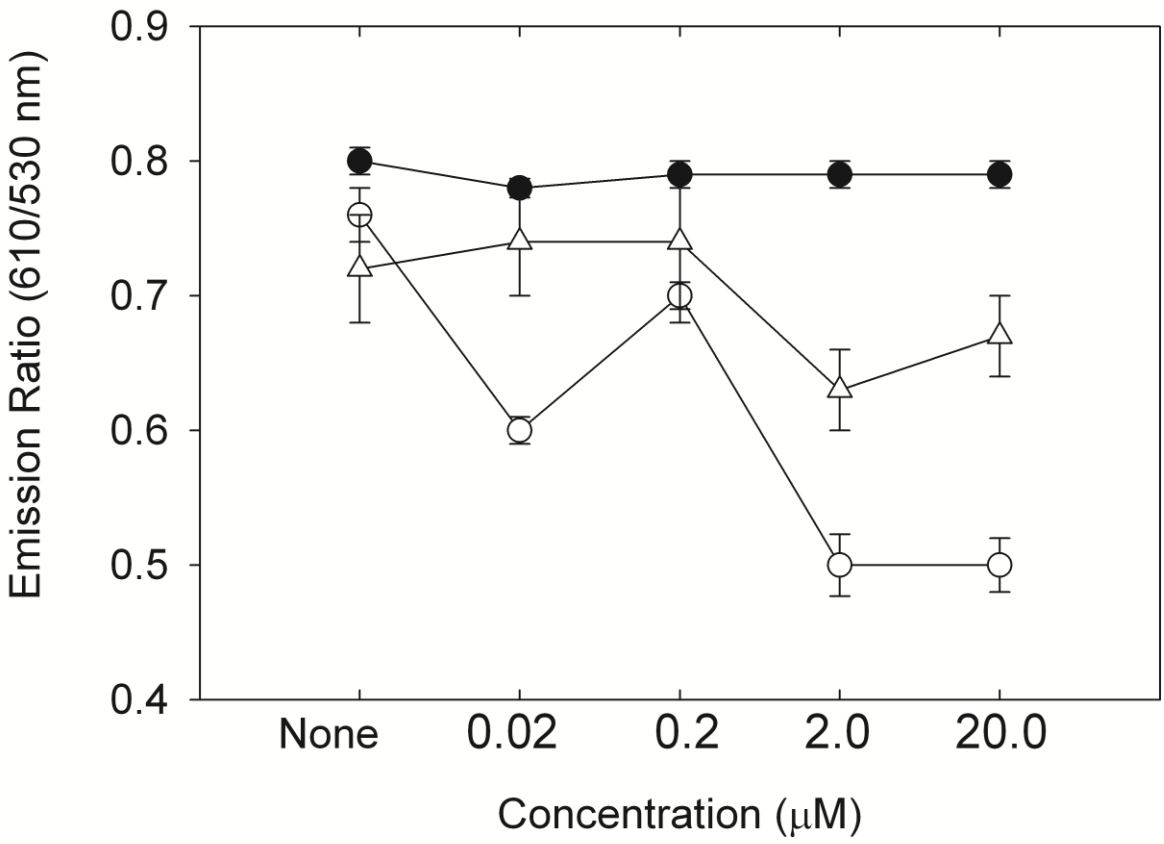
Emission Ratio (610/530 nm)
0.9
0.8
0.7
0.6
0.5
0.4
None
0.02
0.2
2.0
20.0
Concentration (μM)

Figure 4

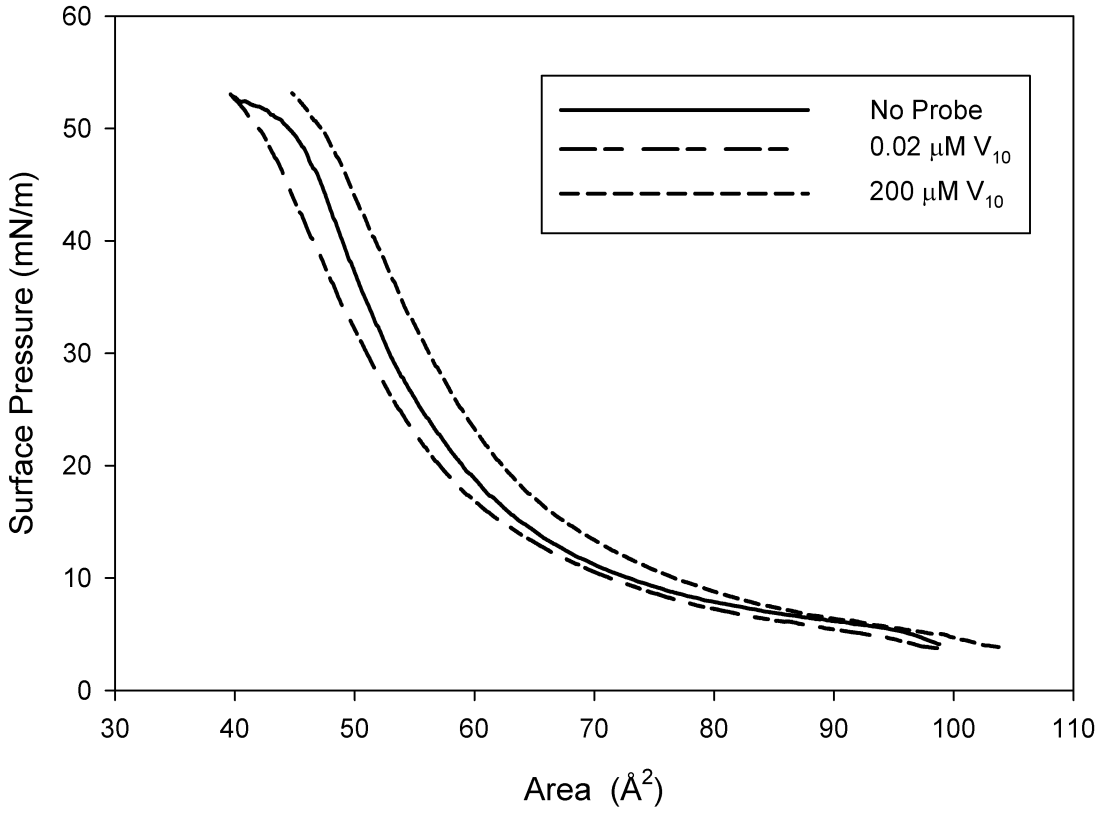
Surface Pressure (mN/m)
Area (Å^2)
No Probe
0.02 μM V_{10}
200 μM V_{10}
0
10
20
30
40
50
60
30
40
50
60
70
80
90
100
110

Figure 5

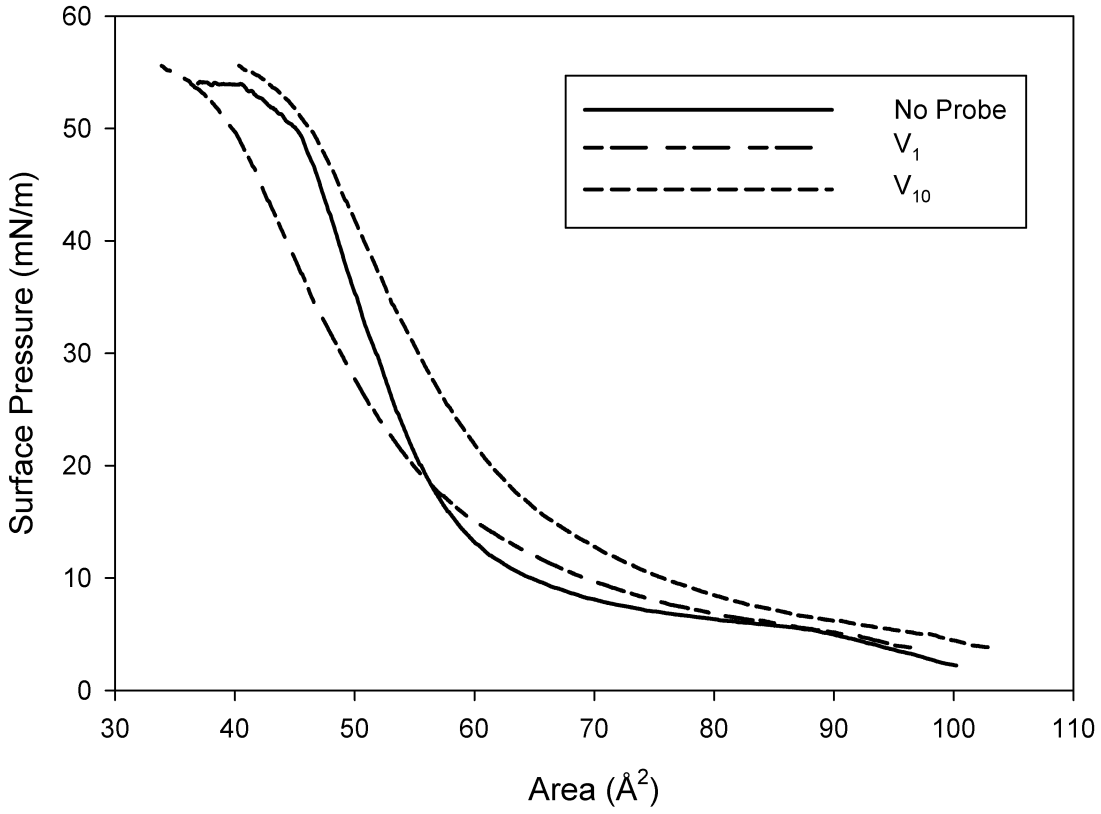
Surface Pressure (mN/m)
Area (Å^2)
No Probe
V_1
V_{10}
0
10
20
30
40
50
60
30
40
50
60
70
80
90
100
110

Figure 6

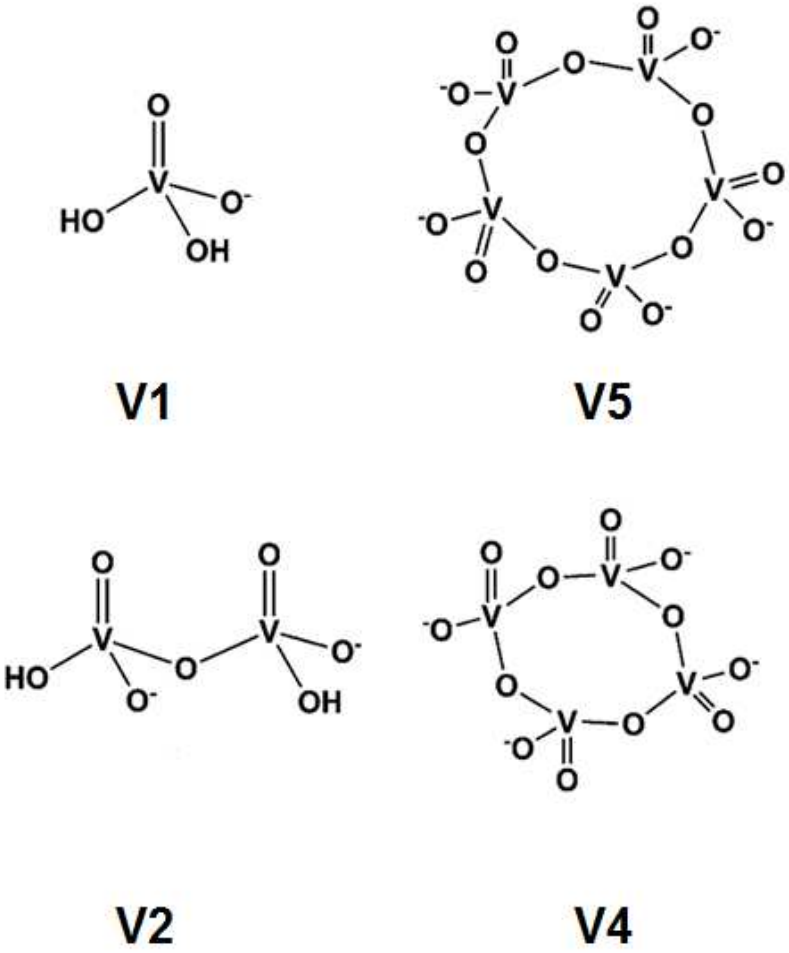

Figure 7

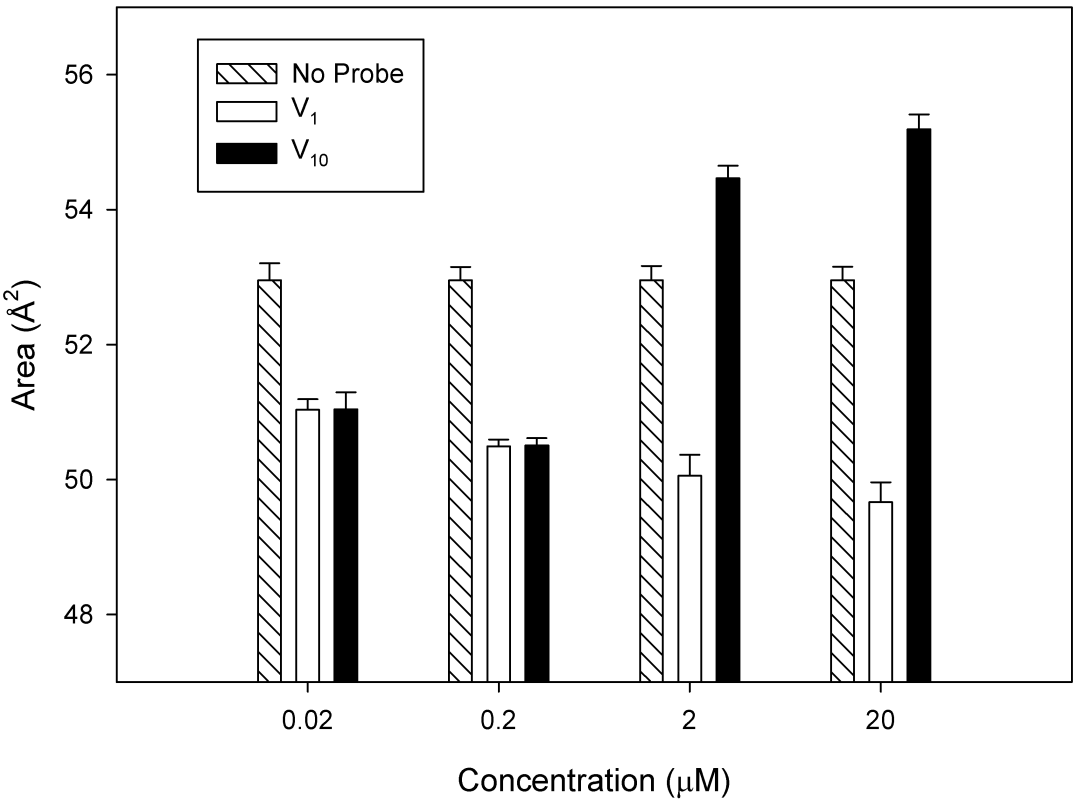
No Probe
V1
V10
56
54
52
50
48
Area (Å2)
0.02
0.2
2
20
Concentration (μM)

Figure 8